SEPTEMBER 2021 M.Sc. in Electrical and Electronics Engineering WALEED KHALED ABDULRAZAQ

REPUBLIC OF TURKEY

GAZİANTEP UNIVERSITY

GRADUATE SCHOOL OF NATURAL & APPLIED SCIENCES

MODELING AND CONTROL OF 1.5 MW RATED SPARSE MATRIX CONVERTER BASED WIND ENERGY CONVERSION SYSTEM

M.Sc. THESIS

IN

ELECTRICAL AND ELECTRONICS ENGINEERING

BY

WALEED KHALED ABDULRAZAQ ABDULRAZAQ

SEPTEMBER 2021

MODELING AND CONTROL OF 1.5 MW RATED SPARSE MATRIX CONVERTER BASED WIND ENERGY CONVERSION SYSTEM

M.Sc. Thesis

in

Electrical and Electronics Engineering
Gaziantep University

Supervisor

Assoc. Prof. Dr. AHMET METE VURAL

by

Waleed Khaled Abdulrazaq ABDULRAZAQ

September 2021

MODELING AND CONTROL OF 1.5 MW RATED SPARSE MATRIX CONVERTER BASED WIND ENERGY CONVERSION SYSTEM

submitted by **Waleed Khaled Abdulrazaq ABDULRAZAQ** in partial fulfillment of the requirements for the degree of Master of Science **Electrical and Electronics Engineering, Gaziantep University** is approved by,

Prof. Dr. Mehmet İshak YÜCE
Director of the Graduate School of Natural and Applied Sciences ……………..........

Prof. Dr. Ergun ERÇELEBİ
Head of the Department of Electrical and Electronics Engineering …………….......

Assoc. Prof. Dr. Ahmet Mete VURAL
Supervisor, Electrical and Electronics Engineering
Gaziantep University ……………..........

Exam Date: 9 September 2021

Examining Committee Members:

Assoc. Prof. Dr. Ahmet Mete VURAL
Thesis Supervisor, Electrical and Electronics Engineering
Gaziantep University …........................

Assoc. Prof. Dr. Mehmet Ali ÖZÇELİK
Electrical and Electronics Engineering
Gaziantep University ……………..........

Assist. Prof. Dr. Murat Mustafa SAVRUN
Electrical and Electronics Engineering
Adana Alparslan Türkeş Bilim ve Teknoloji Üniversitesi ……………..........

I hereby declare that all information in this document has been obtained and presented in accordance with academic rules and ethical conduct. I also declare that, as required by these rules and conduct, I have fully cited and referenced all material and results that are not original to this work.

Waleed Kahled Abdulrazaq ABDULRAZAQ

ABSTRACT

MODELING AND CONTROL OF 1.5 MW RATED SPARSE MATRIX CONVERTER BASED WIND ENERGY CONVERSION SYSTEM

ABDULRAZAQ, Waleed Khaled Abdulrazaq
M.Sc. in Electrical and Electronics Engineering
Supervisor: Assoc. Prof. Dr. Ahmet Mete Vural
September 2021
97 pages

Sparse matrix converter (SMC) is a matrix converter topology without any storage element like an inductor or a capacitor. There is a fictitious DC link between rectifier and inverter stages in SMC topology. The input is directly connected to the output via a set of bidirectional power semiconductor switches. Such an arrangement decreases the converter size and increases the reliability. Due to these advantages, SMC is used in many applications like AC drives, aerospace industry, electric ships, as well as in wind energy applications. In this thesis, a three-phase SMC is adapted to a grid-connected permanent magnet synchronous generator-based wind energy conversion system (WECS). The IGBT is chosen as the power semiconductor element in the rectifier and inverter stages, controlled by sinusoidal pulse width modulation technique. The switching frequency is changeable in the range between 20-50 kHz. The overall system including the power stage as well as the control sub system are modelled and tested under various operating conditions. An LCL filter is replaced at the output of the SMC to weaken switching harmonics. Moreover, a fuzzy fractional-order PID (FFOPID) controller is designed to control active and reactive power of WECS. By this way, the dynamic response of a classical PID controller with fixed gains is improved by combining the salient features of fractional-order calculus and fuzzy logic theory. The simulation results show that the designed FFOPID controller is superior to classical PID controller in tracking d- and q-axis current references of the SMC at the output. FFOPID controller shows better transient performance when unit step changes are applied to the reference signals.

Key Words: Sparse Matrix Converter, Permanent Magnet Synchronous Generator, Wind Energy Conversion System, Fuzzy Fractional-Order PID Controller

ÖZET

1.5 MW GÜÇ KAPASİTELİ SEYREK MATRİX DÖNÜŞTÜRÜCÜ TABANLI RÜZGAR ENERJİSİ DÖNÜŞÜM SİSTEMİNİN MODELLEMESİ VE DENETİMİ

ABDULRAZAQ, Waleed Khaled Abdulrazaq
Yüksek Lisans Tezi, Elektrik ve Elektronik Mühendisliği
Danışman: Doç. Dr. Ahmet Mete Vural
Eylül 2021
97 sayfa

Seyrek matris dönüştürücü (SMD), indüktör veya kapasitör gibi herhangi bir depolama elemanı olmayan bir matris dönüştürücü topolojisidir. SMD topolojisinde doğrultucu ve evirici aşamaları arasında hayali bir DC bağ bulunur. Giriş, bir dizi çift yönlü güç yarı iletken anahtarı aracılığıyla doğrudan çıkışa bağlanır. Böyle bir düzenleme sayesinde, dönüştürücü boyutu küçülmekte ve güvenilirlik artmaktadır. Bu avantajlardan dolayı SMD, AC sürücüler, havacılık endüstrisi, elektrikli gemiler gibi birçok uygulamada ve rüzgar enerjisi uygulamalarında kullanılmaktadır. Bu tezde, üç fazlı bir SMD, şebekeye bağlı kalıcı mıknatıslı senkron jeneratör tabanlı rüzgar enerjisi dönüşüm sistemine (REDS) uyarlanmıştır. IGBT, sinüzoidal darbe genişlik modülasyonu tekniği ile kontrol edilen doğrultucu ve evirici aşamalarında güç yarı iletken elemanı olarak seçilmiştir. Anahtarlama frekansı 20-50 kHz aralığında değiştirilebilir. Güç aşamasının yanı sıra kontrol alt sistemi de dahil olmak üzere genel sistem modellenmiş ve çeşitli çalışma koşulları altında test edilmiştir. Anahtarlama harmoniklerini zayıflatmak için SMD'nin çıkışına bir LCL filtresi yerleştirilmiştir. Ayrıca, REDS'nin aktif ve reaktif gücünü kontrol etmek için bir bulanık kesirli sıralı PID (FFOPID) denetleyici tasarlanmıştır. Bu sayede, sabit kazançlı klasik bir PID kontrolörün dinamik yanıtı, kesirli mertebeden hesap ve bulanık mantık teorisinin göze çarpan özellikleri birleştirilerek iyileştirilmiştir. Benzetim sonuçları, tasarlanan FFOPID denetleyicisinin, çıkışta SMD'nin d ve q ekseni akım referanslarını izlemede klasik PID denetleyiciden üstün olduğunu göstermektedir. FFOPID denetleyicisi, referans sinyallerine birim adımdeğişiklikleriuygulandığındadahaiyigeçiciperformansgöstermektedir.

Anahtar Kelimeler: Seyrek Matris Dönüştürücü, Kalıcı Mıknatıslı Senkron Jeneratör, Rüzgarenerjisi Dönüşüm Sistemi, Bulanık Kesirli Sıralı PID Denetleyici.

''Dedicated to my family''

ACKNOWLEDGEMENTS

I would like to thank my supervisor, Assoc. Prof. Dr. Ahmet Mete Vural for his guidance and support throughout the study. I am thankful for his encouragement and motivation, and useful critiques of this research work. His willingness to give his time so generously has been very much appreciated.

I would like to express my love and gratitude to my family, especially my mother and my wife, for their support and encouragement, always best wishes.

Finally, I would like to express my gratitude to my friends who encouraged and supported me throughout my research.

TABLE OF CONTENTS

Page

LIST OF TABLES

LIST OF FIGURES

Page

LIST OF SYMBOLS

$\boldsymbol{\rho}$	Air density
$\boldsymbol{m}$	Air mass
α	Alpha
$\boldsymbol{W_t}$	Angular speed of the wind turbine
$\mathbf{w_r}$	Angular velocity of the rotor
$\boldsymbol{\beta}$	Beta
i	Current
$\mathbf{i_d}$	Current d-axis
$\mathbf{i_q}$	Current q-axis
$\mathbf{L_d}$	d–axis inductance
$\boldsymbol{D_t}$	Damping coefficient
C	DC link capacitance
dB	Decibel
$\boldsymbol{w_{ebs}}$	Electrical base speed
$\boldsymbol{e}$	Error
$\Delta\boldsymbol{e}$	Error change
e(t)	Error signal with respect to time
$\boldsymbol{d/dt}$	First order time derivative
Vf	Forward voltage
$\boldsymbol{\mu}$	Fractional component of derivative parts
$\boldsymbol{\lambda}$	Fractional component of integral parts
fs	Switching frequency
F	Friction of rotor
G	Gain
H	Henry
Hz	Hertz
L	Inductor
$\boldsymbol{H_t}$	Inertia constant of the turbine

J	Inertia of the rotor
Ic	Initial current
N	Integer number
$K_P, K_{I,} K_D$	Initial gain value of the FOPID controller
K	Kilo
P_m	Mechanical power
T_m	Mechanical torque
M	Mega
µA	Microampere
uF	Microfarad
nF	Nanofarad
p	Number of pole pairs
Ω	Ohm
Π	Pi
β	Pitch angle
lbf	Pound-force
C_p	Power coefficient of the turbine
L_q	q–axis inductance
Iq	q-axis current
ref	Reference
θ	Rotor angular
$\Delta K_P, \Delta K_I \Delta K_D$	Scaling factors computed from fuzzy logic control
K_{ss}	Shaft stiffness
,T_s	Shaft torque
θ_{sta}	Shaft twist angle
Cs	Snubber capacitance
Rs	Snubber resistance
S	Surface area of the turbine
S	Switch
λ	Tip speed ratio
v_{wind}	Velocity of the wind

V	Voltage
$\mathbf{V_d}$	Voltage d-axis
$\mathbf{V_q}$	Voltage q-axis
W	Watt
Wb-t	Weber-turn
P_w	Wind power
v	Wind speed

LIST OFABBREVIATIONS

AC	Alternating Current
CMC	Conventional Matrix Converter
CSI	Current Source Inverter
CSR	Current Source Rectifier
DC	Direct Current
DFIG	Doubly Feed Induction Generator
DMC	Direct Matrix Converter
EESG	Electrically Excited Synchronous Generator
FFOPID	Fuzzy Fractional Order Proportional Integral Derivative
FO	Fractional Order
FOC	Fractional Order Control
FOMCON	Fractional Order Modeling Control
FS	Frequency of Switch
HTSG	High Temperature Superconducting Generator
IGBT	Insulated Gate Bipolar Transistor
IGCT	Integrated Gate Commutated Thyristors
ILMC	Inverting Link Matrix Converter
IMC	Indirect Matrix Converter
IS	Inverter Stage
MC	Matrix Converter
MOSFET	Metal Oxide Semiconductor Field-Effect Transistor
MVA	Mega Volt-Ampere
NB-NM-NS	Negative Big- Negative Medium- Negative Small
PB-PS-PM	Positive Big- Positive Medium- Positive Small
PID	Proportional Integral Derivative
PLL	Phase Lock Loop
PM	Permanent Magnet

PMSG	Permanent Magnet Synchronous Generator
P-Q	Real Power-Reactive Power
PWM	Pulse Width Modulation
RB-IGBT	Reverse Blocking Insulated Gate Bipolar Transistor
rpm	Round Per Minute
RS	Rectifier stage
SMC	Sparse Matrix Converter
SPWM	Sinusoidal Pulse Width Modulation
SVM	Space Vector Modulation
THD	Total Harmonic Distortion
TWh	Tera Watt-hours
USMC	Ultra-Sparse Matrix Converter
VSI	Voltage Source Inverter
VSMC	Very Sparse Matrix Converter
VSR	Voltage Source Rectifier
WECS	Wind Energy Conversion System
Z	Zero

CHAPTER I

INTRODUCTION

1.1 Introduction to Wind Energy

The simplified principle that generates wind is the movement of air due to heating by the sun. Because the air is hotter on the earth than on the water, hot air rises and the cold air descends into the bottom, and this movement is opposite at night, in the same principle that creates winds around the earth. As the air around the equator is hot compared to at the north and south poles, this wind movement is used in generating the electrical energy [1][2]. Wind energy is one of the most vital renewable energy types. Wind energy has been relied upon since ancient history. Moreover, it was used by the people of Nile and China. The Reeds were used to weave windmill blades. Man continued to use wind energy and developed its use until the Middle Ages. One of the primary uses of wind energy in those times was to grind grain to produce food. After wind technology arrived in Europe with the trade, Dutch were the first to develop it in Europe, using windmills to drain lakes [1][2]. Wind energy continued to grow in the other hemisphere after arriving with immigrants. Grinding of grain and logs of wood was a prominent use among Americans, and they used water-pumping windmills and small wind turbines in the 1900s. With the arrival of electricity in the countryside, the number of wind pumps began to decrease, but recently it had become popular, especially in remote areas, to supply electricity [1][2]. Due to the oil crisis in the 1970s and the escalation of environmental concerns due to emissions generated by fossil fuels, in addition to the need to diversify sources of electrical energy to meet the growing demand for it [3], the trend towards creating alternative energy sources has been a priority for many countries. There is an increasing interest in solar energy and wind energy sources, especially in Turkey. The power generated from wind turbines has continually increased. The energy generated from wind in Turkey grew from 0.0050% in 1998 to 8.4% in 2020. It has grown to be one of the

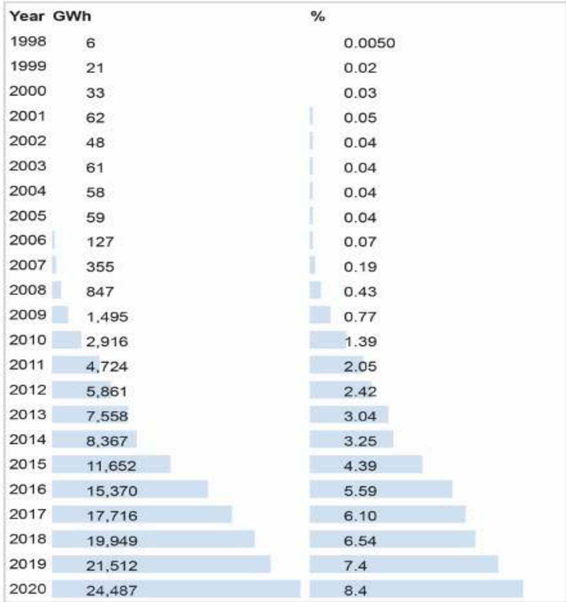

Year	GWh	%
1998	6	0.0050
1999	21	0.02
2000	33	0.03
2001	62	0.05
2002	48	0.04
2003	61	0.04
2004	58	0.04
2005	59	0.04
2006	127	0.07
2007	355	0.19
2008	847	0.43
2009	1,495	0.77
2010	2,916	1.39
2011	4,724	2.05
2012	5,861	2.42
2013	7,558	3.04
2014	8,367	3.25
2015	11,652	4.39
2016	15,370	5.59
2017	17,716	6.10
2018	19,949	6.54
2019	21,512	7.4
2020	24,487	8.4

Figure 1.1 Wind energy growth rate over 23 years in Turkey[4][5]

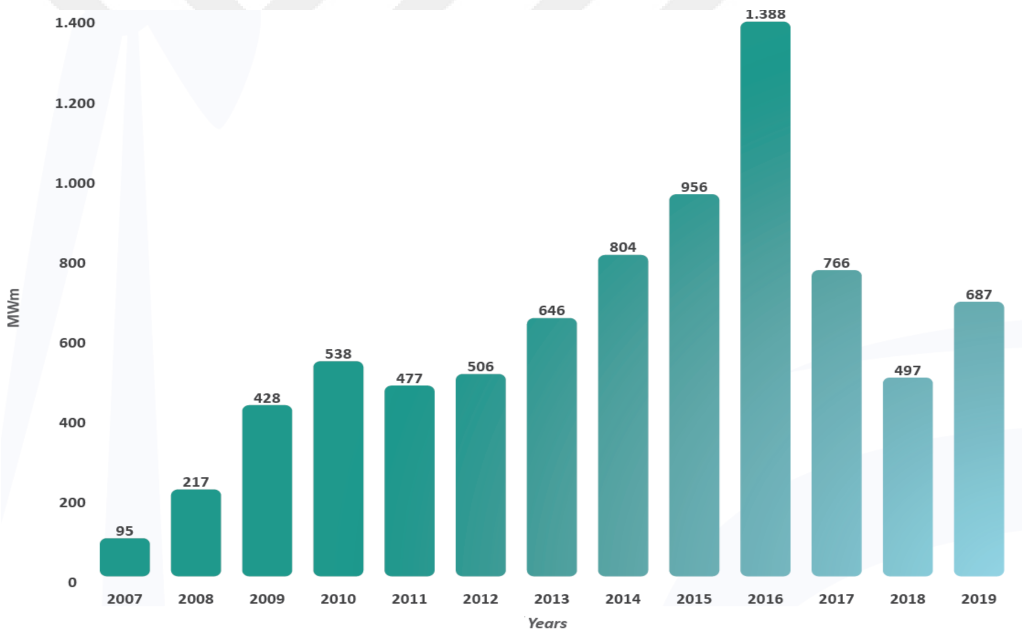

Figure 1.2 Wind power plants in Turkey from 2007 to 2019 [6]

crucial sources of energy, according to the statistics shown in Figure 1.1 [4] [5]. As of 2020, the installed capacity was 9,305 MW compared to 51 MW in 2006. Figure 1.2 shows the annual installations of wind power plants in Turkey. Wind energy has witnessed growth in many other countries, such as China, the largest wind energy generator globally. The statistic shave reached that129countries have been producing 1.13 trillion kilowatt hours of wind energy. Figure 1.3 shows the distribution of wind energy according to the production of each country. The statistics on wind energy worldwide have witnessed significant growth during the last 20 years, as shown in Figure 1.4. Figure 1.5 shows the development of renewable energies worldwide, including wind energy.

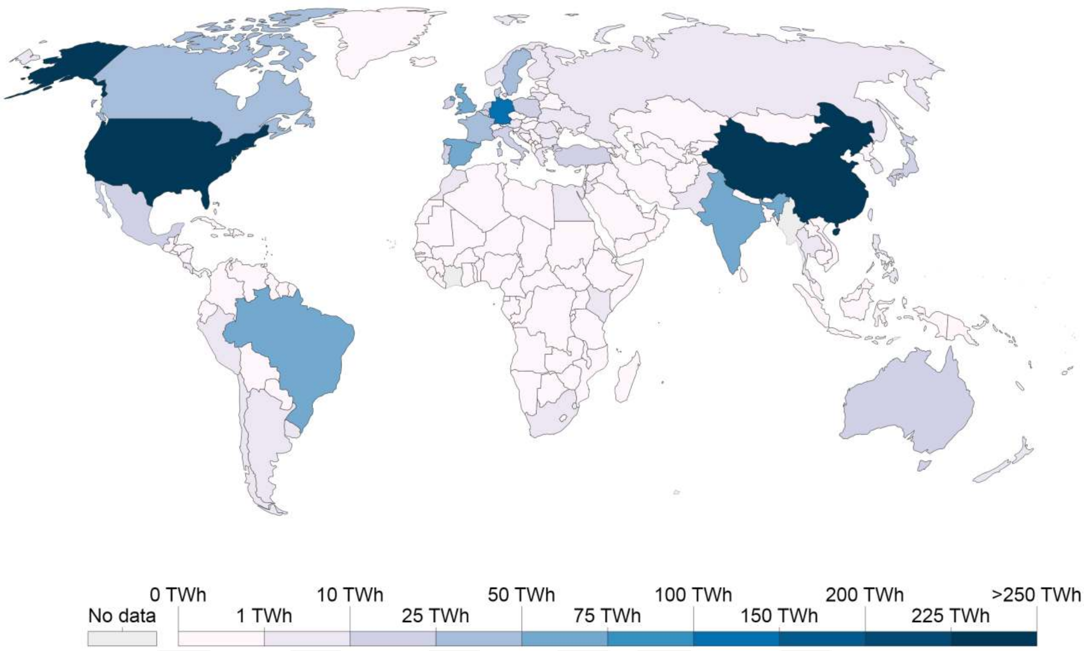

Figure 1.3 Annual electricity generation from wind in 2020 [7][8]

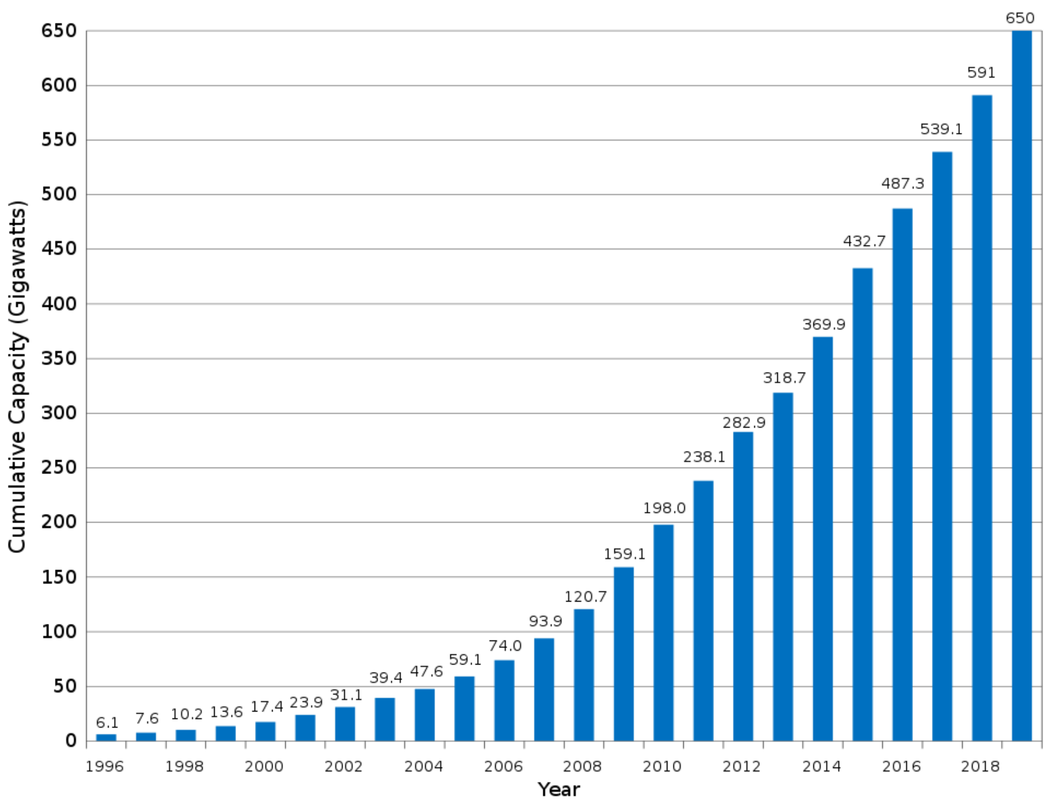

Figure 1.4 Global wind power cumulative capacity [9]

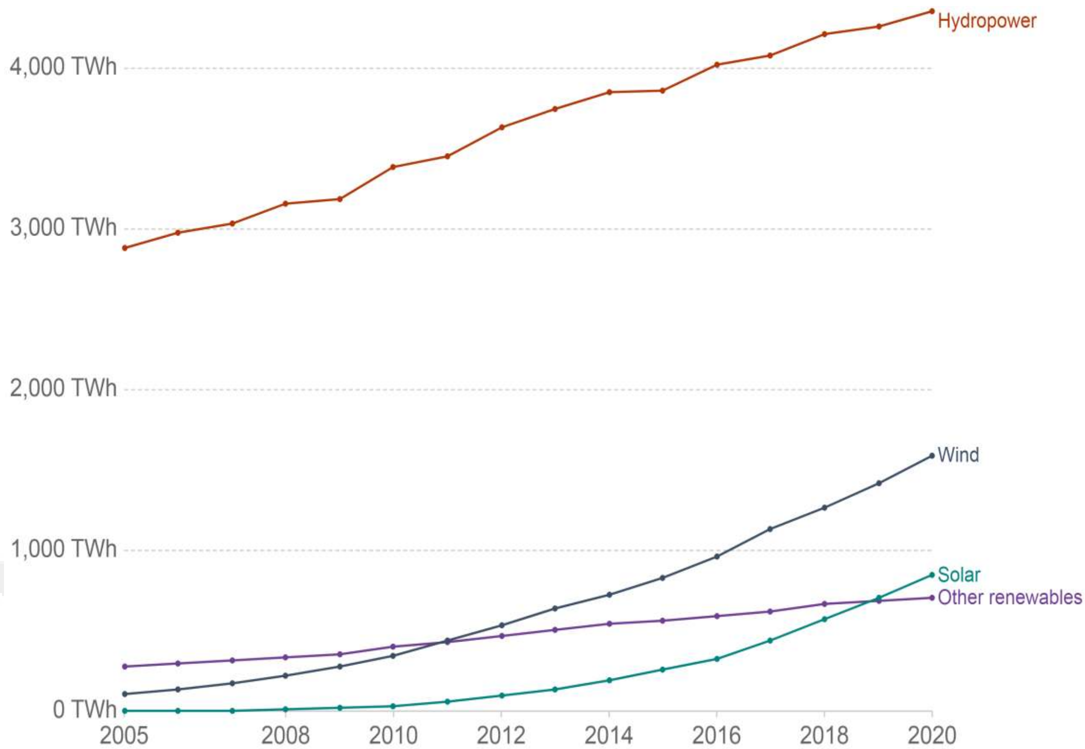

Figure 1.5 Renewable energy generation by source in the world during the past five years [7][8]

1.2 Introduction to Wind Energy Conversion Systems (WECS)

The wind turbine is the central part of WECS. The blades are connected to the wind turbine that are used to collect the wind movement's energy. The movement of the wind over the blades causes it to lift as the same principle used to raise the wings of a plane. Moreover, this effect leads to the rotation of the blades. These blades are connected to an electric generator by a drive shaft. Figure 1.6 shows the parts of a wind turbine. There are two types of turbines: horizontal axis turbine and vertical axis turbine. Wind turbines are of different sizes, and the greater the size of the turbine, the greater the amount of generating electricity. The generated power ranges from 10-kilowatt for households to 10,000 kilowatts or even more to grid.

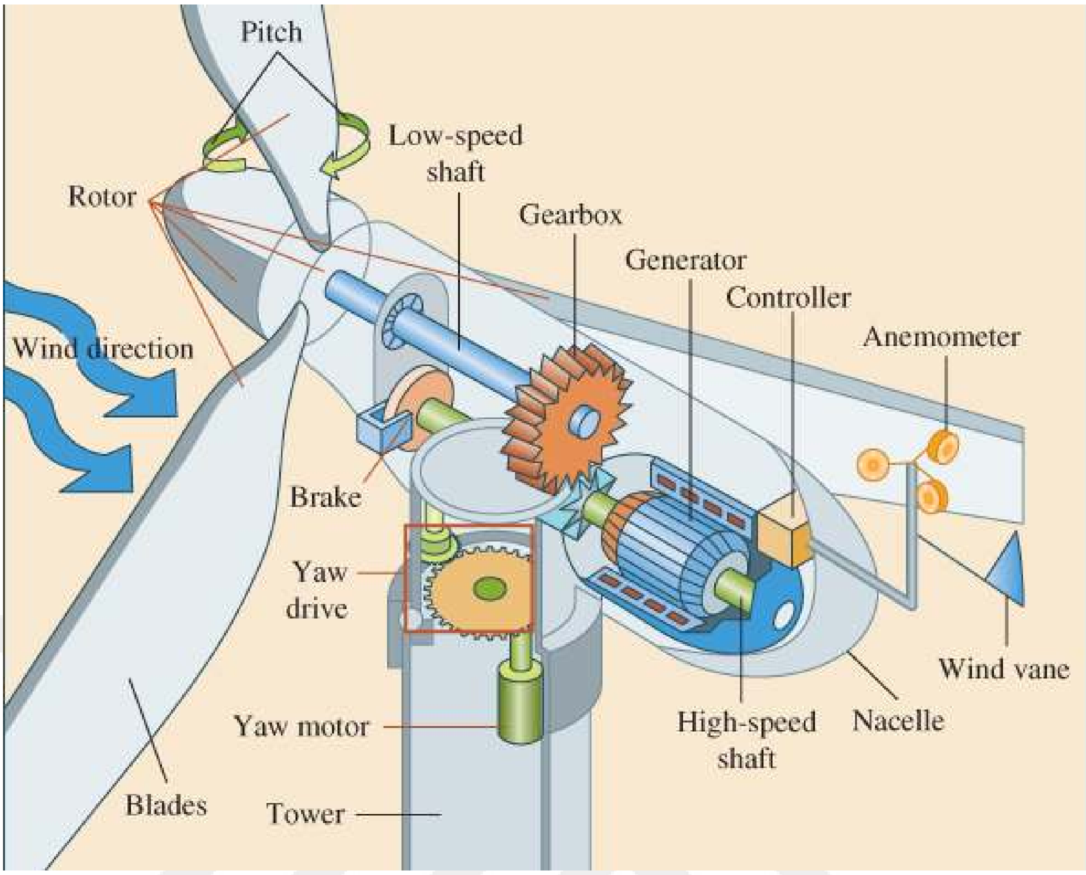

Figure 1.6 The wind turbine parts [10]

Figure 1.7 (a)shows a horizontal axis wind turbine which is more widely used than the vertical axis one, as shown in Figure 1.7 (b). Darius wind turbine is one of the most famous types of vertical axis wind turbines. Generally speaking, horizontal axis wind turbines have more advantages than vertical axis ones, such as high-power output, high efficiency and high reliability [11]. The wind turbines are also categorized according to their locations: onshore and offshore [1], as shown in Figure 1.8. Wind turbines in large areas are called as “wind power stations” or “wind power farms”. The wind farms are usually connected to the electricity network (grid). The Horse Hollow Wind Power Center in Texas is the largest wind farm in the world, containing 430 wind turbines on an area of 47,000 acres with a capacity of 735 MW [1].

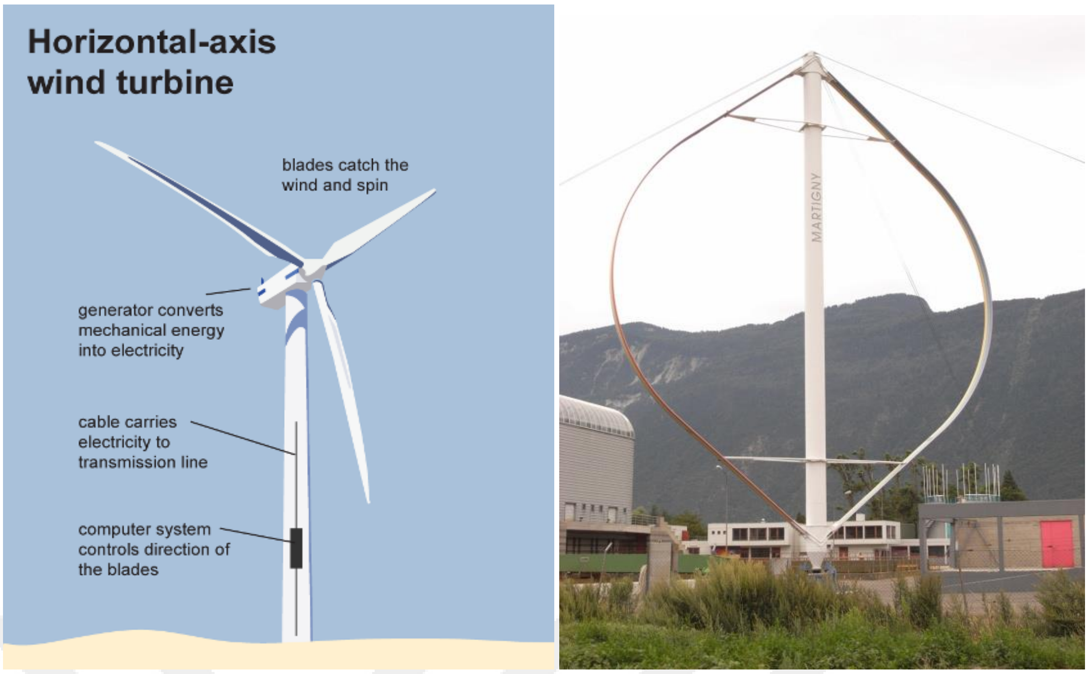

(a) (b)

Figure 1.7 Wind turbine types: (a) horizontal axis; (b) vertical axis [1]

(a) (b)

Figure 1.8 Categories of wind turbine according to area: (a) onshore; (b) offshore [1][12]

1.3 Motivation of the Study

The increasing demand for electric power calls for diversifying energy sources. Because of the significant damages that fossil fuel-based sources produce on the environment, it is imperative to give priority to renewable energies and develop the related technologies. WECS needs to transfer the energy collected by the turbine to the electrical grid by means of power electronic based power converters. The power converters are used to dynamically control the generated power from the WECS. A "sparse matrix converter" (SMC) is one of the modern power converters used in the field of wind energy conversion that does not contain any storage elements like a capacitor or an inductor. The elimination of such an energy storage element at the DC link helps to design smaller size WECS. As in case of conventional power converters used in WECS, with a SMC, it is also possible to dynamically control the real/reactive power injected into the grid. The output parameters of SMC such as, magnitude, frequency as well as the phase angle of the output voltage can be controlled. With this respect, this thesis aims the design and simulation of a SMC based WECS connected to the grid.

1.4 Purpose of the Study

This thesis provides a study for modeling and simulation of a SMC based WECS connected to the grid. The WECS uses a "permanent magnetic synchronous generator" (PMSG) with a production capacity of 1.5MW. An LCL filter at the output of the SMC is designed to achieve the elimination of the switching disturbances and a lowest value of the total harmonic distortion (THD) at the output. The modeling and simulation studies of the SMC based WECS are accomplished using both PID and fuzzy based fractional order PID controllers. These two controllers are also compared in terms of their dynamic performances. It is shown that the latter one has better results. The simulation results verify the validity of the designed model of the PMSG based WECS and the controllers.

1.5 Organization of the Thesis

This thesis consists of five chapters organized as follows:

CHAPTER I: This chapter includes a review of wind energy. Also, the development of wind energy applications to generate electrical power, as well as some statistical data of the development of wind energy use in Turkey are also summarily given. The components of a WECS are also briefly introduced in this chapter.

CHAPTER II: This chapter categorizes the types of matrix converters used in WECS. SMC is also detailed in this chapter.

CHAPTER III: This chapter includes the theoretical study of the SMC including its electrical circuit and the control methods related with it.

CHAPTER IV: This chapter includes the proposed design of the SMC-based WECS. The results obtained from the simulation environment are presented and discussed.

CHAPTER V: This chapter finally concludes about the results obtained from this thesis study. The future aspirations related to this study are also presented.

CHAPTER II

LITERATURE SURVEY AND BACKGROUND

2.1 Matrix Converter (MC) Topology

Matrix converter (MC) topology is based on a direct transform method from AC-to-AC power without any energy storage device like a capacitor or an inductor. Its working principle depends on nine bi-directional power electronic switches which are made from semiconductors. These switches connect the input stage to the output stage. Figure 2.1 (a) represents the switch allocations in MC topology. Figure 2.1 (b) represents the switch details of the MC topology. The output voltage with desired magnitude, frequency and angle is obtained by a proper switching mechanism for the power electronic switches that connects the input to the output.

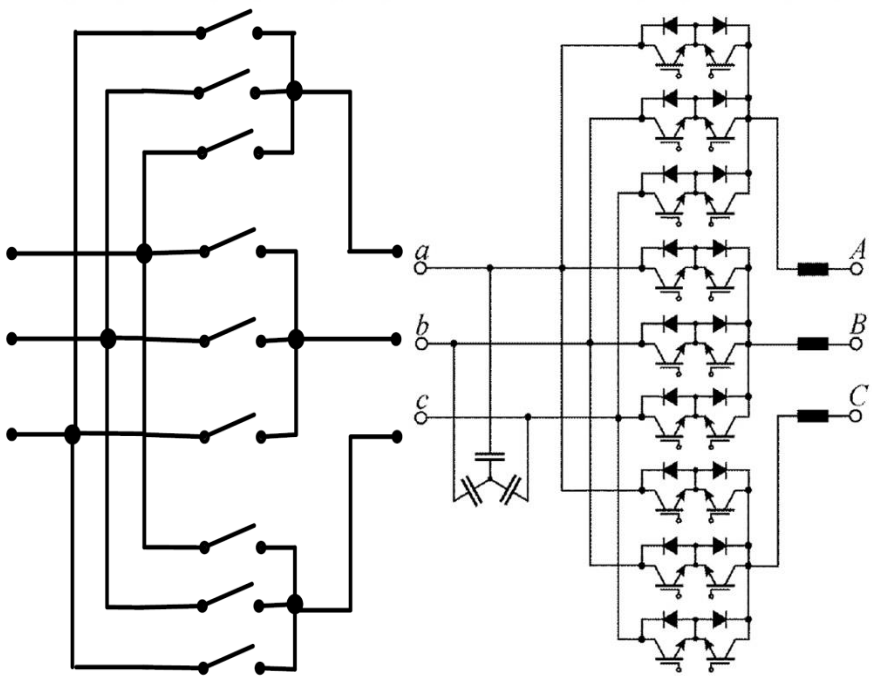

(a) (b)

Figure 2.1 The main structure of MC: (a) the switch allocations; (b) the switch details [13]

The real work of developing the MC in its modern form began with the publication of Venturini and Alesina, who were the first to introduce the name known as "MATRIX CONVERTER" [14][15] by introducing an electrical power circuit containing bidirectional power switches. One of their most important contributions is to describe the low-frequency behavior using mathematical analysis. They introduced the concept of “low-frequency modulation matrix”, also known as a “direct transfer function approach”—the output voltage results by multiplying the modulation matrix by the input voltage. Bidirectional switches are the main component of the MC, and each switch is an electronic circuit made up of semiconductors. These switches are arranged in a controlled manner that helps to create an output voltage with a frequency that is also controlled. The input can be controlled regardless of load in MC, and an adjustable power factor helps with that. Early work was completed to obtain a bidirectional control switch. Among these, the thyristors and an externally forced commutation circuits were used [1][16]. In this arrangement, the circuit was heavy and primitive and the performance was poor. However, after developing the transistor to enter many fields, including the bidirectional control switch, it changed the idea about bidirectional switches [17][18]. The absence of DC link due to the presence of bidirectional switches ensures that there are no heavy and bulky elements for energy storage. Such a design provides compact design, thus making the system lighter and more reliable to operate. There are many advantages of the MC over classical AC-DC-AC converters. MC has the ability to operate at higher temperatures and more reliable because of the absence of the energy storage element. Moreover, the size of MC is smaller when compared to classical AC-DC-AC converters. All these advantages make the MC the integrated and desirable choice in the field of industrial applications, for example, aerospace industries [19][20], marine propulsion industry, variable speed electrical machines [21][22], embedded systems, and military industries as well. MC can also be used in the field of renewable energies, especially those depend on wind energy [23][24]. Despite the many advantages of the MC, it also has some downsides. MC lacks fully of controlled bilateral switches. The voltage ratio is also limited. Another problem in MC is the switch commutation problem produced from over-current due to short-circuiting of the AC sources, or over-voltage spikes that may destroy the power semiconductor. Safe commutation has been accomplished by developing several multi-step commutation strategies and the "semi-soft current commutation" technique [25].MC has become necessary in wind energy conversion applications due to the increasing research on it. Several solutions have been proposed for MC operation.MC is divided into two types; direct matrix converter (DMC) or conventional matrix converter (CMC) and indirect matrix converter (IMC) [26][27]. Figure 2.2 shows the primary classification AC-AC converters.

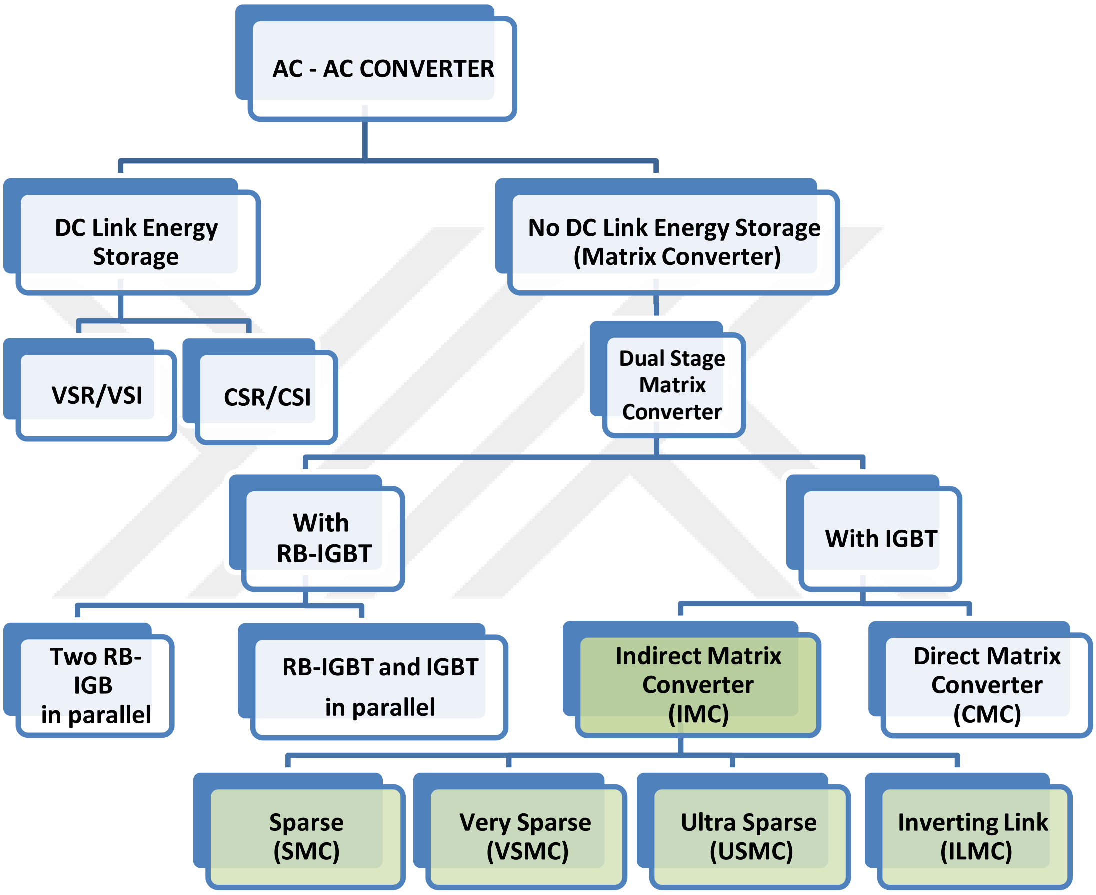

Figure 2.2 The primary classification of AC-AC converter [28][29]

2.1.1 Direct Matrix Converter Topology

The Conventional Matrix Converter (CMC) or Direct Matrix Converter (DMC) consists of nine bi-directional switches distributed into four quadrants. In using semiconductors, the arrangement will be 18 semiconductors (IGBT) with 18 diodes, as shown in Figure 2.3 [13]. The manner-based modulation of the switches in the dual-stage MC is called as “modulation function” [21][30].

2.1.1.1 Mathematical Model of DMC

The relationship matrices that refer to the rectifier stage from dual-stage are represented in Equations (2.1) and (2.2).

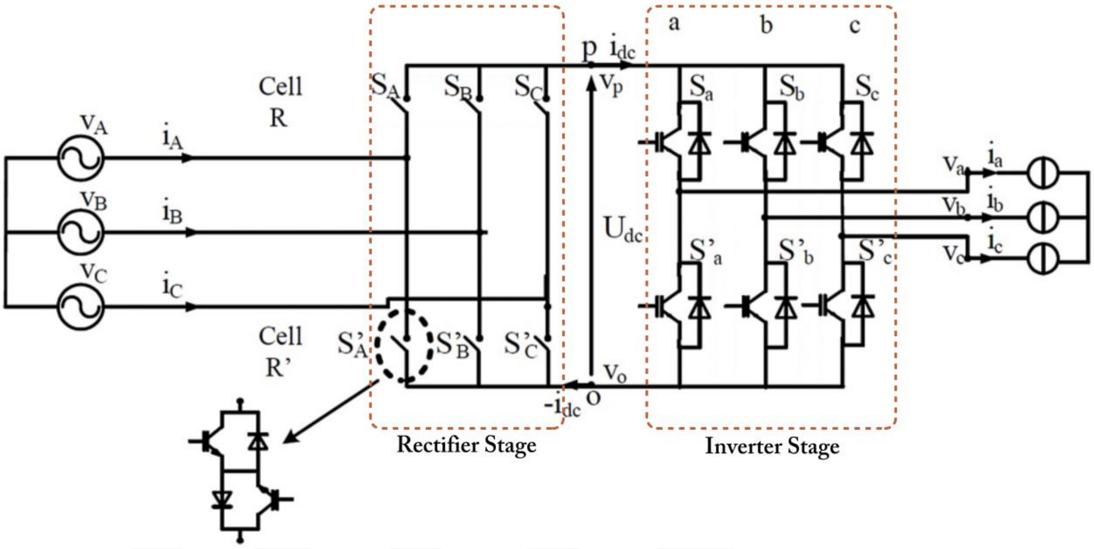

Figure 2.3 Power circuit topology of DMC or (CMC) [13]

$$[M_{rect}] = \begin{bmatrix} m_A & m_B & m_C \\ m'_A & m'_B & m'_C \end{bmatrix} \tag{2.1}$$

$$\begin{Bmatrix} m_A + m_B + m_C = 1 \\ m'_A + m'_B + m'_C = 1 \end{Bmatrix} \tag{2.2}$$

During the commutation period (T), the (S_i) will switch in the conduction time (t_i) and the relationship that represents this operation is shown in Equation (2.3).

$$m_i = \frac{t_i}{T} \tag{2.3}$$

The relationship that represents the inverter stage is shown in Equations (2.4) and (2.5).

$$[\mathrm{M_{inv}}] = \begin{bmatrix} \mathrm{m_a} & \mathrm{m'_a} \\ \mathrm{m_b} & \mathrm{m'_b} \\ \mathrm{m_c} & \mathrm{m'_c} \end{bmatrix} \tag{2.4}$$

$$\left\{\begin{array}{c} m_a + m'_a = 1 \\ m_b + m'_b = 1 \\ m_c + m'_c = 1 \end{array}\right\} \quad (2.5)$$

The expressions that represent the rectifier operation of MC are given in Equations (2.6) and (2.7).

$$\begin{bmatrix} v_p \\ v_o \end{bmatrix} = [M_{rect}] \begin{bmatrix} v_A \\ v_B \\ v_C \end{bmatrix} \quad (2.6)$$

$$\begin{bmatrix} i_A \\ i_B \\ i_c \end{bmatrix} = [M_{rect}]^T \begin{bmatrix} i_{rect} \\ -i_{rect} \end{bmatrix} \quad (2.7)$$

The expressions that represent the inverter operation of MC are given in Equations (2.8) and (2.9).

$$\begin{bmatrix} v_a \\ v_b \\ v_c \end{bmatrix} = [M_{inv}] \begin{bmatrix} v_p \\ v_o \end{bmatrix} \quad (2.8)$$

$$\begin{bmatrix} i_{dc} \\ -i_{dc} \end{bmatrix} = [M_{inv}]^T \begin{bmatrix} i_a \\ i_b \\ i_c \end{bmatrix} \quad (2.9)$$

The matrix $[M_{DE}]$ resulting from the multiplication of the rectifier modulation matrix with the inverter modulation matrix is shown in Equation (2.10).

$$[M_{DE}] = [M_{inv}].[M_{rec}] = \begin{bmatrix} m_a & m'_a \\ m_b & m'_b \\ m_c & m'_c \end{bmatrix} . \begin{bmatrix} m_A & m_B & m_C \\ m'_A & m'_B & m'_C \end{bmatrix} \quad (2.10)$$

The relationship that represents the result of the connection between two matrices is represented in Equation (2.11).

$$[M] = [M_{DE}] \Rightarrow \begin{bmatrix} m_{Aa} & m_{Ba} & m_{Ca} \\ m_{Ab} & m_{Bb} & m_{Cb} \\ m_{Ac} & m_{Bc} & m_{Cc} \end{bmatrix} = \begin{bmatrix} m_a & m'_a \\ m_b & m'_b \\ m_c & m'_c \end{bmatrix} . \begin{bmatrix} m_A & m_B & m_C \\ m'_A & m'_B & m'_C \end{bmatrix} \quad (2.11)$$

During the commutation period (T), the (S_{ij}) will switch in the conduction time (t_{ij}) and the relationship that represents this operation is shown in Equation (2.12).

$$m_{ij} = \frac{t_{ij}}{T} \quad (2.12)$$

2.1.2 Indirect Matrix Converter (IMC) Topology

The IMC topology, also known as "double stage topology," was developed in the early 2000s to substitute for the DMC topology. The power circuit of a three-phase IMC represented in Figure 2.4.

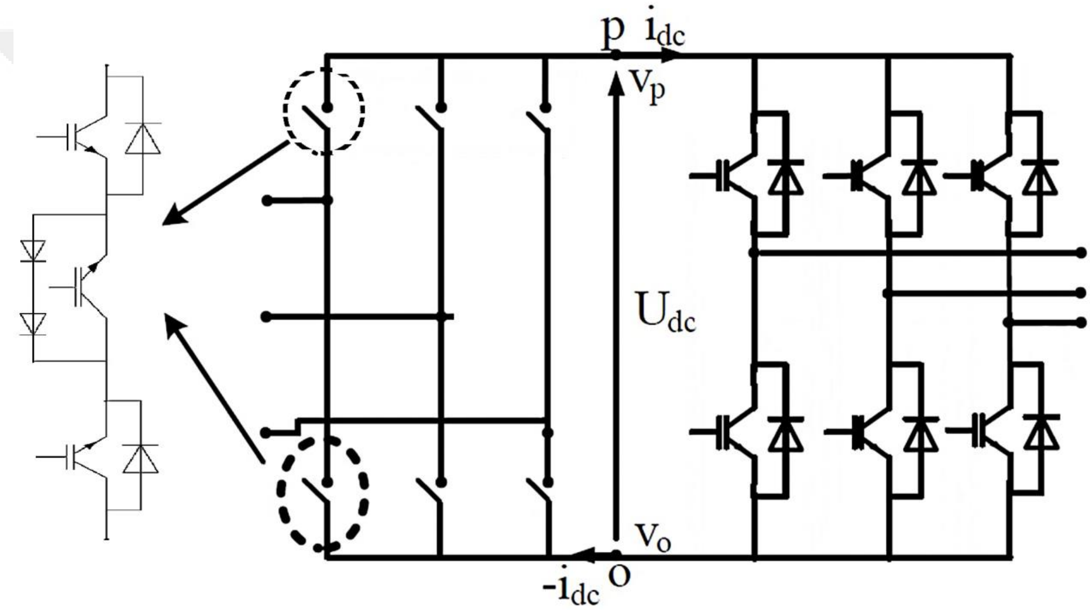

Figure 2.4 Power circuit topology of IMC [13]

This topology has two stages; rectifier and inverter. The rectifier stage contains six bidirectional switches. Each switch combines two power semiconductor switches (IGBT, IGCT, or MOSFET) with an anti-parallel diode connection. The semiconductor switches can be in a common-emitter or common collector configuration. The rectifier stage is connected to the AC voltage source as the input and the output is fictitious DC voltage. The rectifier is connected to the inverter by a fictitious DC link. In the DC link, there is no storage element, such as a capacitor or an inductor. The inverter stage contains six power semiconductor switches such as IGBT, IGCT, or MOSFET. The inverter generates a controllable three-phase voltage at its output. A control algorithm and a switching modulation scheme can change the output voltage's magnitude, phase angle, as well as frequency [30]. There is a relationship between the modulation function of IMC produced from the DMC topology. The arrangement of IMC, which contains two-stage, is developed byJ.W. Kollar [30]. The advantage of this arrangement minimizes the number of transistors. Due to a large number of switches in IMC, many types of research have emerged to reduce the number of transistors in the MC topology, thus make it easier to monitor and control [31]. IMC also has gained much interest and associated modeling approaches. Several topologies for IMC have been developed, including the sparse matrix converter (SMC) family. This family is the latest technology developed in the MC field compared to CMC. Furthermore, the SMC has some sub-types, such as very sparse matrix converter (VSMC), ultra sparse matrix converter (USMC), and inverting link matrix converter (ILMC). In this study, SMC topology is used as the AC-AC converter topology in a WECS.

2.1.2.1 Mathematical Model of IMC

Equation (2.13) shows the connection matrix of the rectifier stage S_{rec}, where S_x represents the state of each power electronic switch availableat the phase-x. $S = 1$ means that the switch is turned on, while $S = 0$ means that the switch is turned off. The notation S' denotes the reciprocal state of the respected switch. In the time of switching for both cells, one switch is always closed [30]. The necessary conditions for the switches in the rectifier stage can be expressed in Equation (2.14). The voltage and current relations represent the IMC's rectifier operation expressed in Equations (2.15) and (2.16), respectively. v_p and v_0 represent the voltage of two points illustrated in Figure 2.3. v_A, v_B, v_c are the phase voltages of the input side. i_A, i_B, i_c are the phase input currents and i_{dc} is the DC current flowing from the rectifier to the inverter stage. The connection matrix of the inverter stage is shown in Equation (2.17). The necessary conditions for the switches in the inverter stage are shown in Equation (2.18). The voltage and current relations representing IMC's inverter operation are expressed in Equations (2.19) and (2.20), respectively. The matrix $[S_{DE}]$ expressed in Equation (2.21) is the connection matrix of the IMC, resulting from the multiplication of the connection matrices of the rectifier and inverter stages.

$$[S_{rec}] = \begin{bmatrix} S_A & S_B & S_C \\ S'_A & S'_B & S'_C \end{bmatrix} \quad (2.13)$$

$$\begin{gathered} S_A + S_B + S_C = 1 \\ S'_A + S'_B + S'_C = 1 \end{gathered} \quad (2.14)$$

$$\begin{bmatrix} v_p \\ v_o \end{bmatrix} = [S_{rect}] \begin{bmatrix} v_A \\ v_B \\ v_C \end{bmatrix} \quad (2.15)$$

$$\begin{bmatrix} i_A \\ i_B \\ i_C \end{bmatrix} = [S_{rect}]^T \begin{bmatrix} i_{dc} \\ -i_{dc} \end{bmatrix} \quad (2.16)$$

$$[S_{inv}] = \begin{bmatrix} S_a & S'_a \\ S_b & S'_b \\ S_c & S'_c \end{bmatrix} \quad (2.17)$$

$$\left\{ \begin{matrix} S_a + S'_a = 1 \\ S_b + S'_b = 1 \\ S_c + S'_c = 1 \end{matrix} \right\} \quad (2.18)$$

$$\begin{bmatrix} v_a \\ v_b \\ v_c \end{bmatrix} = [S_{inv}] \begin{bmatrix} v_p \\ v_o \end{bmatrix} \quad (2.19)$$

$$\begin{bmatrix} i_{dc} \\ -i_{dc} \end{bmatrix} = [S_{inv}]^T \begin{bmatrix} i_a \\ i_b \\ i_c \end{bmatrix} \quad (2.20)$$

$$[S_{DE}] = [S_{inv}].[S_{rec}] = \begin{bmatrix} S_a & S'_a \\ S_b & S'_b \\ S_c & S'_c \end{bmatrix} . \begin{bmatrix} S_A & S_B & S_C \\ S'_A & S'_B & S'_C \end{bmatrix} = \begin{bmatrix} S_{Aa} & S_{Ba} & S_{Ca} \\ S_{Ab} & S_{Bb} & S_{Cb} \\ S_{Ac} & S_{Bc} & S_{Cc} \end{bmatrix} \quad (2.21)$$

2.2 Comparisons between DMC and IMC

Table 2.1 shows a comparison between different types of MCs, including the SMC family. This comparison examines different MCs in terms of the number of transistors used, the number of diodes used, power losses, and ease of control[28][29]. The primary importance of using SMC is the reducing the number of IGBTs used, thus reducing energy losses and manufacturing costs, lower realization effort, and lower control complexity. On the other hand, Table 2.2 shows a comparison among different power semiconductor switches. As seen, IGBT combines the advantages of both MOSFET and BJT.

Table 2.1 The comparison of different dual-stage MCs [32]

Topology	With RB-IGBT		With IGBT				
	Two RB-IGBT in parallel	RB-IGBT & IGBT in parallel	IMC	SMC	VSMC	USMC	ILMC
Transistor Count	18	18	18	15	12	9	14
Diode Count	18	18	18	18	12	18	14
Losses	low	medium	low	medium	low	low	low
Control	difficult	easy	difficult	difficult	easy	easy	difficult

Table 2.2 The comparison of different power semiconductor switches [33][34]

Device Characteristics	Power BJT	Power MOSFET	Power IGBT
Voltage Rating	High< 1kV	High< 1kV	Very high>1kV
Current Rating	High< 500A	Low< 500A	High> 500A
Input Drive	Current (20-200)µA	Voltage VGS 3-10V	Voltage VGE 4-8 V
Input Impedance	Low	High	High
Output Impedance	Low	Medium	Low
Switching Speed	Slow (microsecond)	Fast (nanosecond)	Medium
Cost	Low	Medium	High

2.3 Permanent Magnet Synchronous Generator (PMSG) based WECS

The wind turbine in a WECS is the part rotated by the blades when the wind blows. Then, the rotor of the generator is connected to the wind turbine to generate electrical power. The electrical generators have witnessed so many developments to reduce losses as well as cost. Previous generators connected to the wind turbines were mostly fixed-speed type. This type of generator is called as “fixed-speed” generator and squirrel cage induction generator is a good example for fixed-speed generators. Much research has been carried out to harvest more energy from the wind. Variable speed WECS is a result of these efforts [35][36]. Permanent magnet synchronous generator (PMSG) can be efficiently used in variable speed wind turbine applications due to many advantages [37][38]. When the pole number is increased in a PMSG, low-speed operation can be possible. Then, a gearbox between the wind turbine and the PMSG can be utilized to increase the rotation speed. There is also an option that the gearbox may not be used which decreases cost and service period while increases the system reliability. There has been more interest in PMSGs in the wind energy industry after the significant increase in turbine sizes [39][40]. There are many advantages of a PMSG. The high torque could be achieved even at low speeds with reduced noise and the absence of the gearbox as an option helps to reduce losses in the rotor system. Self-excitation without a field circuit helps to get rid of the auxiliary accessories such as brushes and slip rings [41][42]. There is no problem on the wind speed change, since the PMSG output is connected to a controlled power conversion system. This system can regulate the output power and the power factor of the WECS. The output voltage is usually stepped up with a power transformer when connecting the WECS to the utility grid. Figure 2.5 depicts the rate of energy change according to wind speed in a typical WECS [43]. Figure 2.6 shows the types of generators used in wind energy applications according to the wind speed.

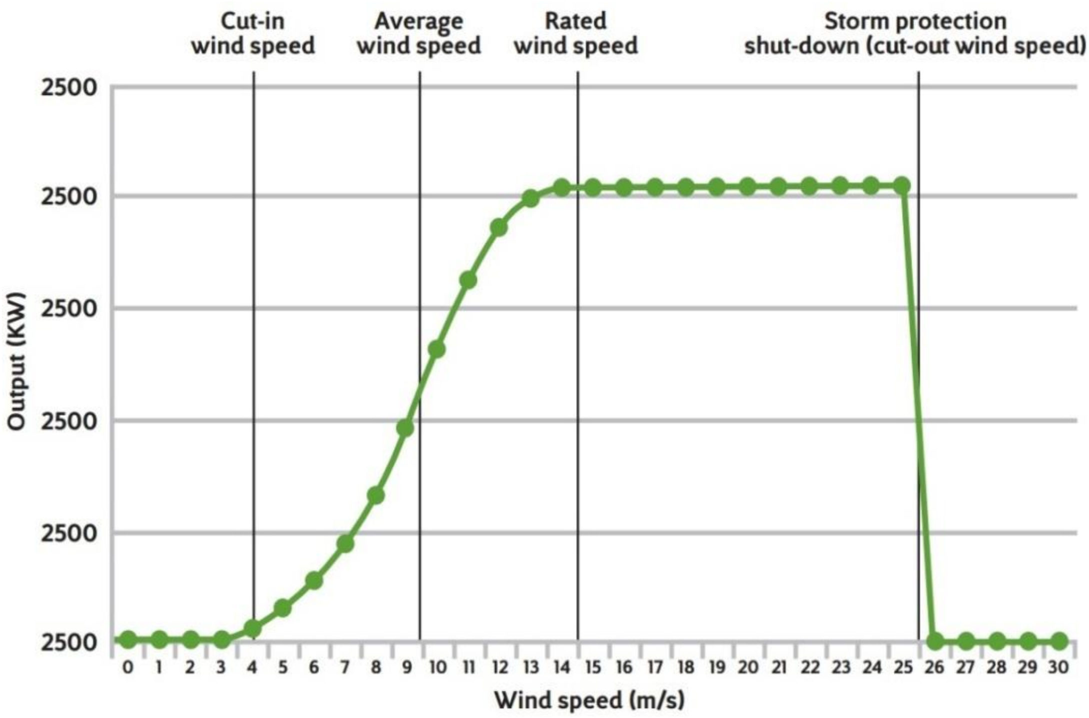

Figure 2.5 The rate of energy change according to wind speed [43]

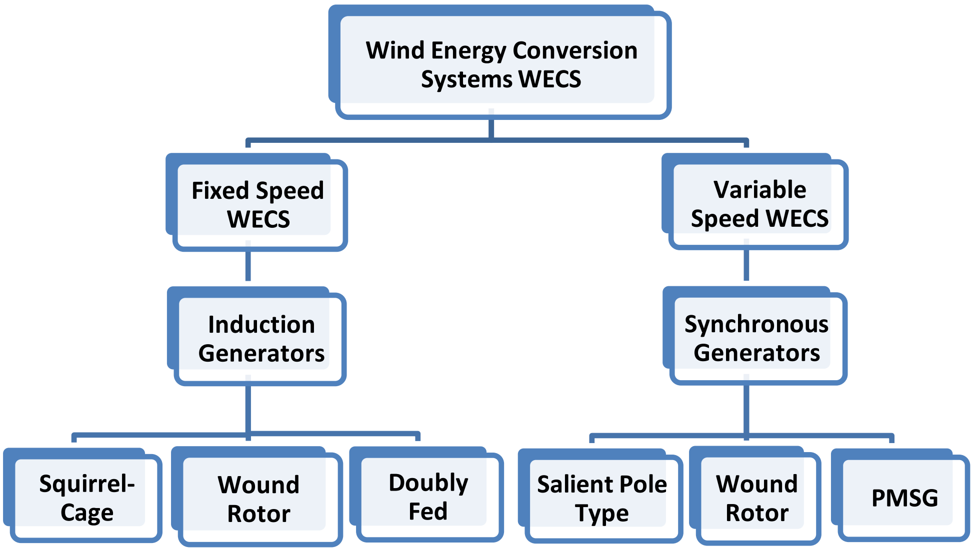

Figure 2.6 Classification of WECS according to the generator types used [44]

The PMSG based WECS is usually divided into two main types according to the use of a DC-DC converter (chopper). Figure 2.7 shows a DC-DC converter circuit used in a PMSG based WECS. On the other hand, Figure 2.8 shows a back-to-back converter arrangement used in a PMSG based WECS. Figure 2.7 explains the first type of converter which is connected to the WECS. This type of converter is also called as "Passive Front End Power Converter". The ruggedness and reliability of this type of rectifier makes it a better choice than active rectifiers where we have to deal with high current switching. But the diode bridge rectifiers inject harmonic components in the system, which raises the THD of the system. Moreover, during passive rectification operation, the maximum power usable cannot be extracted from the PMSG [45]. For the proposed system, each branch is provided with three bidirectional switches to perform the current control and ensure near unity power factor operation. The two diode bridge rectifiers are connected to the three phase PMSG output. They are connected to two same valued capacitors with a midpoint. Each phase of the branches is connected to one bidirectional switch. The later end of the three switches are merged and connected to the midpoint of the capacitors for both branches. When the switches are turned ON, the corresponding phases exercise a rise of current. Turning OFF of the switch is associated with the current conducted from the upper diode or the lower diode of the front half of the diode bridge. Consequently, the phase current reduces. The operation is same for both top and bottom branches [45]. Figure 2.8 explains the second type of converter which is connected to the WECS. This type of converter is also called as "back-to-back converter". The complete structure of the PMSG-based WECS is obtained from a full-scale frequency converter that helps to enable the control access for both active and reactive power which makes a smoother connection to a grid and also helps to achieve the better performance [45]. The closed-loop system is obtained, in which the sufficient stability conditions are correspondingly derived after using PID or FFOPID. The topology of the given system with a two-level full-scale BTB converter bridges the WTS and the grid is illustrated in the work of this thesis.

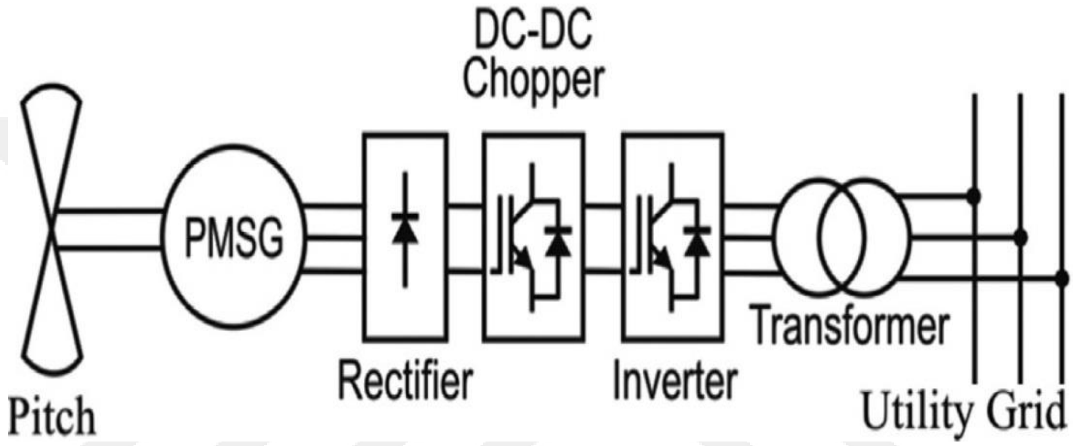

Figure 2.7 DC-DC converter used in a PMSG based WECS [44][45]

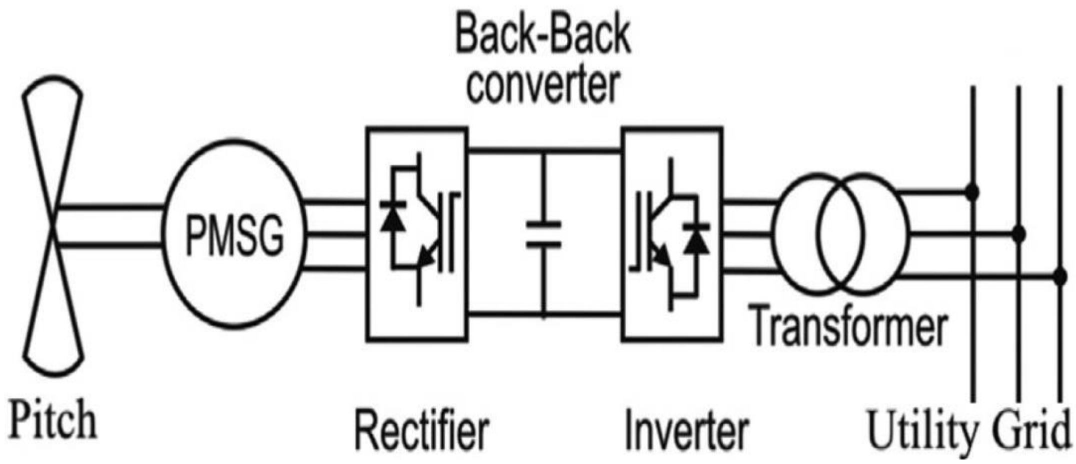

Figure 2.8 Back-to-Back converter arrangement used in a PMSG based WECS [45]

2.4 The Summary

In this chapter, the MC topology and its power circuit were reviewed. It was also referred to the main classification of the types of converters used. The DMC and IMC were mentioned with the power circuits and the mathematical operations that explain the working mechanism of each of them. Also, comparisons were made between DMC and IMC, which showed the superiority of IMC in order to reduce the number of IGBT used, reduce switch losses, and reduce manufacturing cost. A comparison was also made between the types of semiconductors used in the converter. The results of the comparison showed the superiority of IGBT semiconductor over BJT and MOSFET. Finally, the WECS was mentioned, which will be linked later with the converter (Sparse Matrix Converter), and the types of generators that are used with the WECS were clarified. The working mechanism of the WECS was also explained in brief. The control mechanism of the converters used with the WECS, namely, DC-DC converter and back-to-back converter were explained briefly.

CHAPTER III

SPARSE MATRIX CONVERTER

3.1 Sparse Matrix Converter (SMC)

The power circuit of a three-phase sparse matrix converter (SMC) is shown in Figure 3.1[28]. As seen, this a two-stage topology in which there is a fictitious DC link between rectifier and inverter stages without any energy storage element like an inductor or a capacitor. Rectifier stage is the first stage of an SMC which is powered by an AC voltage source on the input side of the rectifier, such as an AC generator. The output current of the rectifier stage is in DC form which flows to the inverter stage through the fictitious DC link. In a PMSG-based WECS, the rectifier stage is connected to the output of the PMSG. The rectifier stage can be controlled using sinusoidal pulse width modulation (SPWM) [46]. The inverter stage is the second part of the SMC. The inverter stage contains a voltage source inverter circuit which is fed from the fictitious DC link. The output of the inverter is controlled such that a sinusoidal voltage waveform is obtained at the output with an appropriate filter. Due to the absence of an energy storage component in the DC link, A synchronization process must be handled between the rectifier and inverter stages. Like the rectifier stage, the inverter stage can be controlled using SPWM for generating the control signals for the power semiconductors.

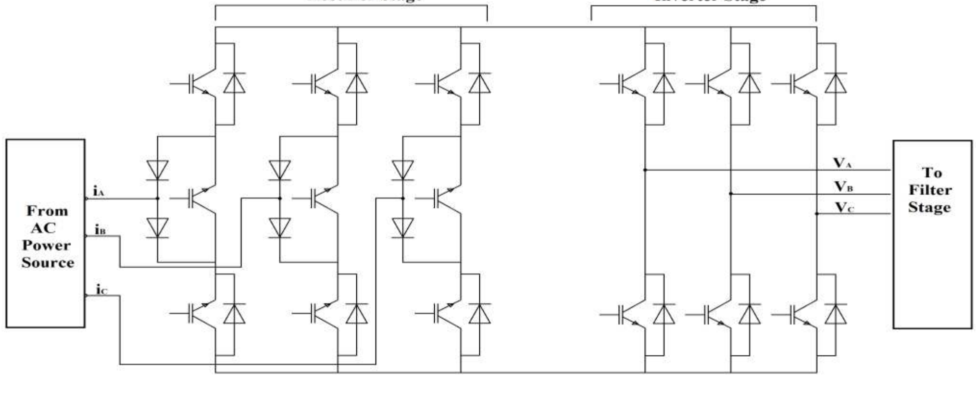

Figure 3.1 The power circuit of a three-phase sparse matrix converter (SMC)[28]

3.2 The Derivation to Obtain SMC Legs

The derivation of a simplified bridge branch structure of the IMC is shown in Figure 3.2 to reduce the number of active switches on the line bridge of CMC. This is possible if we assume that the DC link voltage is positive polarity. If an unidirectional power flow is required, a more simplified version of the system is possible such as VSMC, USMC, and ILMC. The structure of SMC requires the use of a multi-step switch commutation method to fulfill commutation rules.

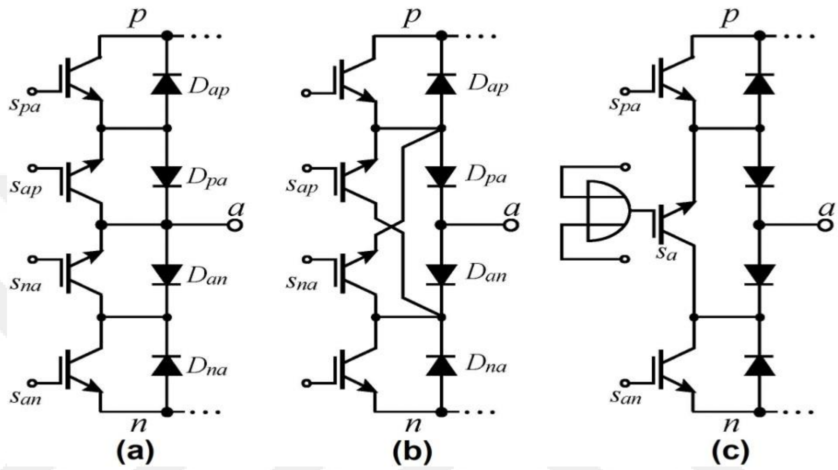

Figure 3.2 Transformation of the leg from 4 IGBTs in CMC to 3 IGBTs in order to obtain the SMC leg [29]

3.3 SMC Commutation Scheme

3.3.1 Multi-Step Commutation

There is a dead time between rectifier and inverter stages in SMC operation. For a specific switching commutation in the input rectifier stage, the output inverter stage of the SMC must have the same commutation as the one in input rectifier stage. So, it must be taken care of to ensure there is no short circuit in the DC link. For example, we have an inverter switching case in SMC in the rectifier input stage, then we must assure that there is no bidirectional connection for two input lines to avoid a possible short circuit in the input line to line voltage. To prevent this from happening, we must use the schemes of multi-step commutation which provides a continuous current path [30]. The schemes of the commutating bridge lines to the SMC are represented in Figure 3.3(a). It is observed that the switch concatenation varies the bus p, representing the positive DC link from input a to b. In Figure 3.3 (b), the voltage is independent for $i > 0$representing the plus DClink current. In Figure 3.3 (c), it is shown that the current is independent for $U_{ab} > 0$.

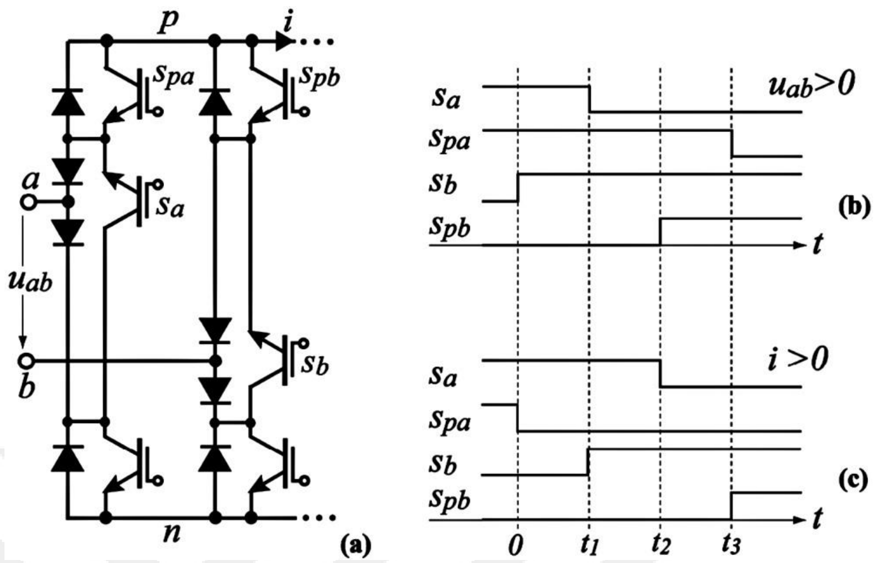

Figure 3.3 SMC rectifier stage and explain the multi-step commutation:

(a) commutating bridge lines to the SMC;

(b) voltage-independent, $i > 0$;

(c) current independent, $U_{ab} > 0$ [30]

3.3.2 Zero DC Link Current Commutation

The previously described multi-step method is complex. The IMC, including SMC, gives more control options that are not available in the CMC. The following method can dispose of the complexity mentioned in the multi-step commutation [30] by changing the inverter stage with a free-wheeling case and changing the rectifier stage with the zero DC link currents. This method is represented in Figure 3.4. Figure 3.4 (a) shows the control in the transistor power to line bridge of SMC. Figure 3.4 (b) shows the switching concatenation $S_{0,}\ S_7 = 1$, referring to the inverter stage that operates under free-wheeling conditions and observing the switch concatenation to vary the bus p, which represents the positive DC link, from input a to input b. The scheme of commutation by zero DC link currents has more than one advantage. It makes the switching loss to be less for the input stage, ensuring no superposition during ON periods in the half-bridge which may cause the short circuit in an input line to line voltage.

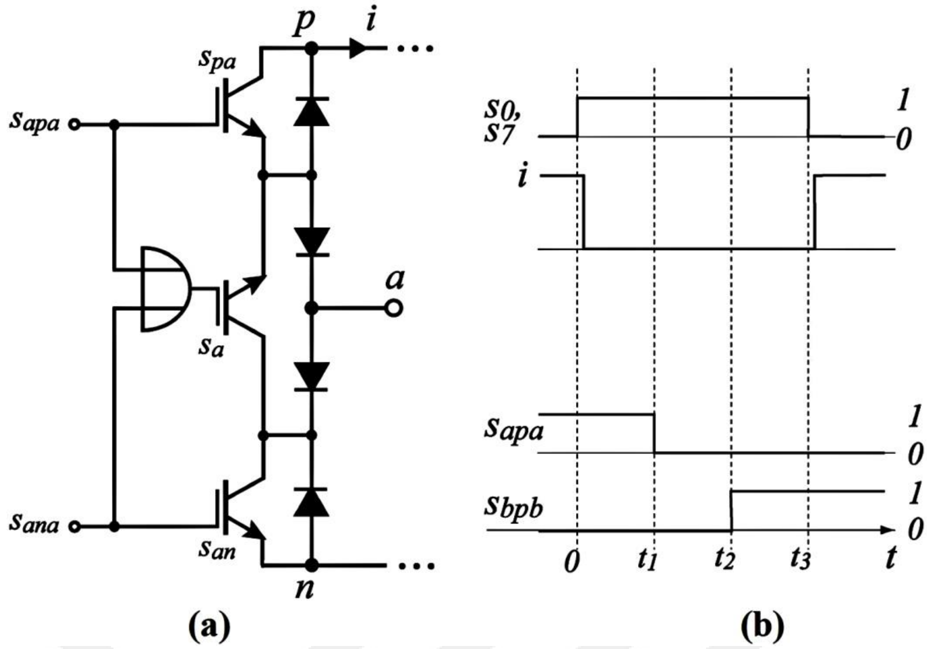

Figure 3.4 SMC for IMC, which explains the zero DC link commutation:
(a) explain the direct application of the switching function to the power transistor;
(b) switching concatenation case, $S_{0,}S_7 = 1$, refer to the inverter stage under the free-wheeling case [30]

3.4 SMC Modulation Strategies

A modulation strategy can be broadly classified into three categories depending upon the type of the calculation of the switch states. Figure 3.5 shows the tree of such a classification for MC modulation techniques. The SMC uses bi-directional switches with high switching frequency by modifying the duty cycle of the switches (S_{jk}) to generate a low-frequency load voltage that varies with amplitude and frequency. A modulation duty cycle should be defined for each switch to determine the average behavior of the MC output voltage waveform. The modulation duty cycle is defined in Equation (3.1).

$$d_{jk}(t) = \frac{t_{jk}}{T_{Seq}} \tag{3.1}$$

wheret_{jk}, represents the time when the switch is turned on. T_{Seq}, represents the time of the complete sequence in the PWM pattern.$0 < d_{jk} < 1$, is based on the switch duty-ratios. The averaged output voltages and the averaged input currents can be related to the input and output currents.

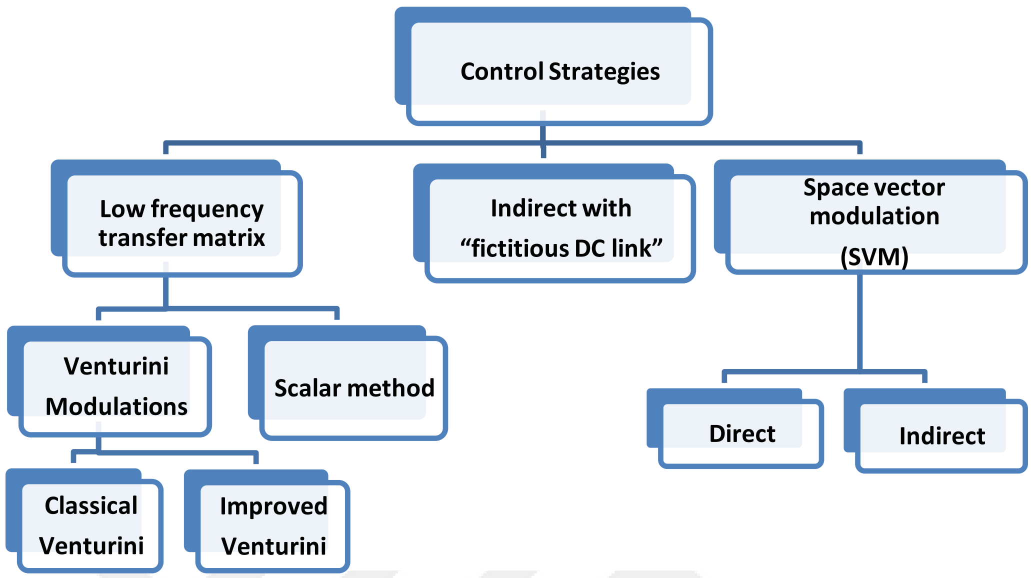

Figure 3.5 Classification of MC modulation techniques [47]

SPWM is one of the most common ways to obtain a sine waveform as much as possible at the output of the inverters. In this technique, the carrier signal is usually a triangular or saw tooth waveform, compared with a reference sinusoidal signal. This comparison generates the control signals of the semiconductors. The ON time of a switch pair is a variable, called the duty cycle (D). If only one sinusoidal reference signal is used, then SPWM scheme is called as bipolar SPWM. On the other hand, if two sinusoidal reference signals are used, then the scheme is called as unipolar SPWM. The PWM technique used for switching of the semiconductor devices of the converter decides the frequency and the AC output voltage of the converter. So, to get the sinusoidal waveform as an output, sinusoidal PWM technique is used. The sinusoidal modulating waveform of 60 Hz system frequency is compared with a high frequency triangular waveform to generate the pulse-width modulated firing pulses for the converter. Two different SPWM methods can be implemented to get the required output.

3.4.1 Bipolar SPWM

In case of bipolar sinusoidal PWM method, a single fundamental frequency modulating waveform per phase is compared with the high-frequency triangular waveform. The output voltage switches between -VDC/2 and +VDC/2 voltage levels where VDC is the total DC voltage. It is the reason why this type of switching is called a bipolar PWM switching. The terminal voltage of the inverter is obtained denoted by VAN and VBN, and the inverter output voltage, VAB,is given by

$$V_{AB} = V_{AN} - V_{BN} \tag{3.2}$$

The waveform of VAB switches between positive and negative DC voltages, and hence this scheme is called bipolar PWM as shown in Figure 3.6. During comparison, when the sinusoidal waveform is greater than the triangular waveform, the PWM trigger signal is high, otherwise it is at lower level [48].

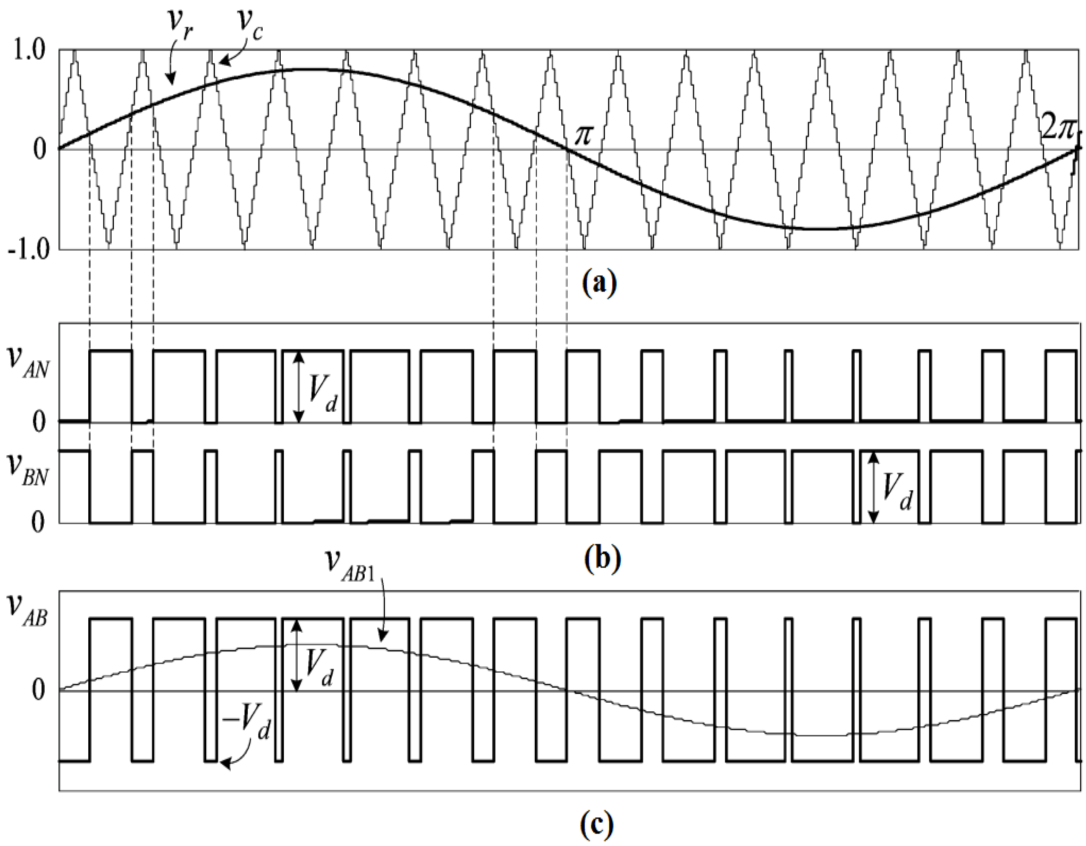

Figure 3.6 Bipolar SPWM voltage: (a) comparison between reference signal and triangular signal; (b) switching pulses; (c) output voltage [48]

3.4.2 Unipolar SPWM

The unipolar SPWM switching signal is shown in Figure 4. The unipolar PWM scheme generally requires two sinusoidal reference waveforms that have the same frequency and magnitude, but with 180 degrees phase shift. The PWM unipolar scheme generally requires two sinusoidal reference waveforms that have the same frequency and magnitude but with 180 degrees phase shift. The triangular signal is compared with two sinusoidal reference signals that are positive and negative signals. The output voltage of the inverter transforms between zero and positive voltage or between zero and negative voltage of the fundamental frequency. The output voltage switches between +VDC/2 and 0 or between 0 and -VDC/2. For this reason, this type of PWM scheme is called a PWM with a unipolar voltage switching. In the unipolar voltage switching scheme, the harmonic content of the output voltage signal is reduced compared to the result obtained in the case of bipolar switching [24][48].

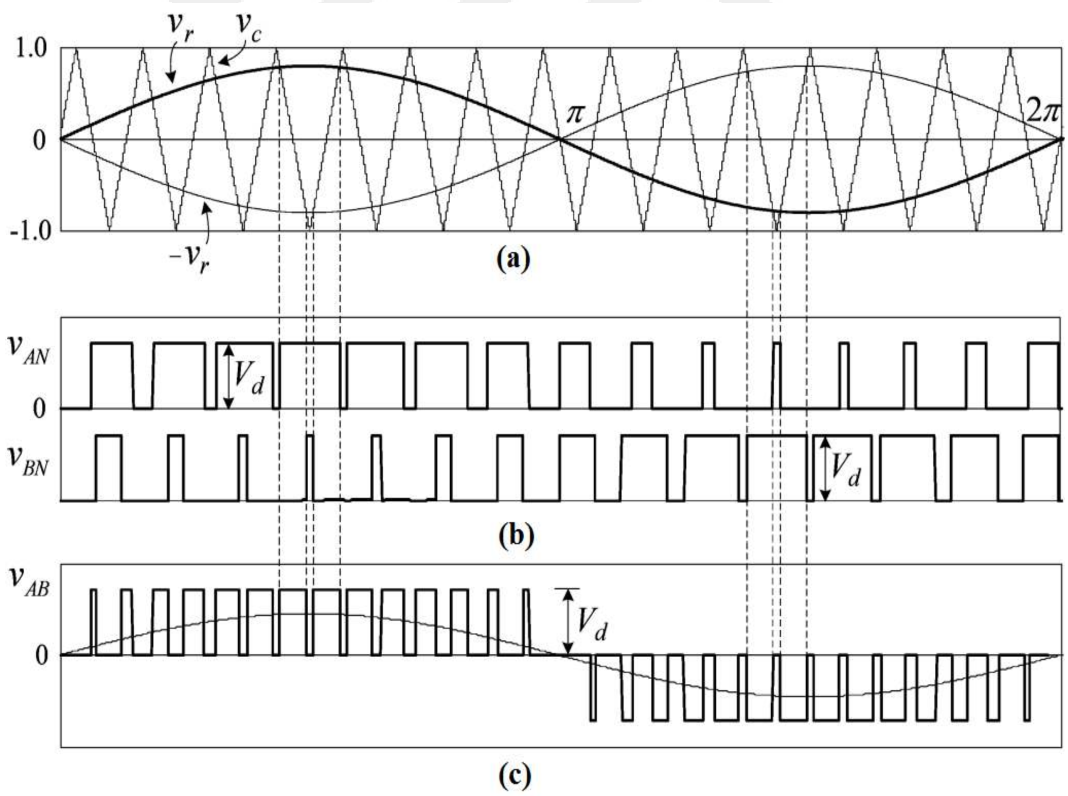

Figure 3.7 Unipolar SPWM voltage: (a) comparison between reference signal and triangular signal; (b) switching pulses; (d) output voltage [48]

3.5 SMC Control Structure

3.5.1 SMC Based PID Controller

The controller in this thesis consists of two control loops. The first one is the voltage regulator which controls the amplitude of the voltage supply in the output using the transformations of d-axis and q-axis. The second loop is the current control which regulates the active power provided by the system at the unity power factor or another power factor depending on dispatch parameters. The use of two independent loops in the controller makes it possible to regulate the active power and reactive power independently. Figure 3.9 shows the general layout of the used controller in this thesis. This control scheme depends on the equations of the inverter model. The voltage and current values obtained from the WECS are calculated using the per unit (pu) system before conversion to the two-axes frame. The phase lock loop (PLL) is used to obtain a reference phase angle information obtained from the grid voltage. Since the controller operation depends on the rotary d-q theory, it is necessary to apply Park's transformation to the voltage and current wave forms. The voltage regulator adjusts AC voltage injected to the grid and determines the reference value i_{d-ref} .Figure 3.9 represents the general control scheme that will be implemented in the simulation environment in Chapter 4 of the thesis. This diagram represents the closed loop control system that is used to control the second stage of the SMC (the inverter stage). In this control scheme, an ABC to dq0 transformation block is used for decoupling of two components (d- and q- component). The d-component is used for active power control. On the other hand, the q-component is used for reactive power control. The two d-q components are dealt with separately using the PID or FFOPID controller to be converted again from dq0 to the ABCto finally obtain a PWM signal set to control the inverter stage. The PWM signals(either 0 or 1) which is used to control the switches of the second stage of SMC (inverter stage). The control signals either turn ON or OFF the specified switch.

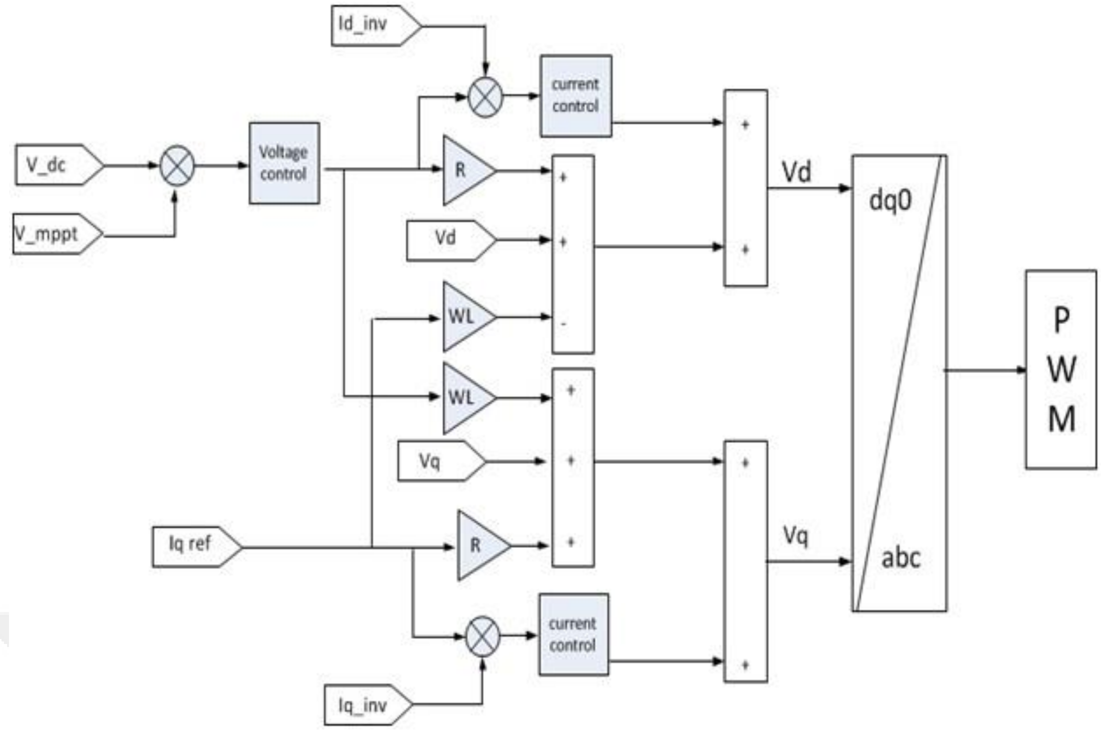

Figure 3.8 The proposed control structure used in this thesis [48]

The voltage regulator ensures that the active power is provided to the utility grid by adjusting the voltage amplitude and not passing the power in the opposite direction. The current controller determines the value of currents $i_d i_q$provided from the WECS system. Active and reactive powers can be calculated in d-q-axis frame as follows [49]:

$$P = V_d i_d + V_q i_q \quad (3.2)$$

$$Q = V_d i_d + V_q i_q \quad (3.3)$$

The reference value $i_{q-ref} = 0$ is usually taken to provide zero reactive power injection or absorption by the WECS or unity power factor operation. After finding the value of $V_d$and V_q, these signals are converted to ABC frame to determine the reference sinusoidal signal used in SPWM scheme. The outline of the closed loop controller which controls the inverter switches is given in Figure 3.10 [48].

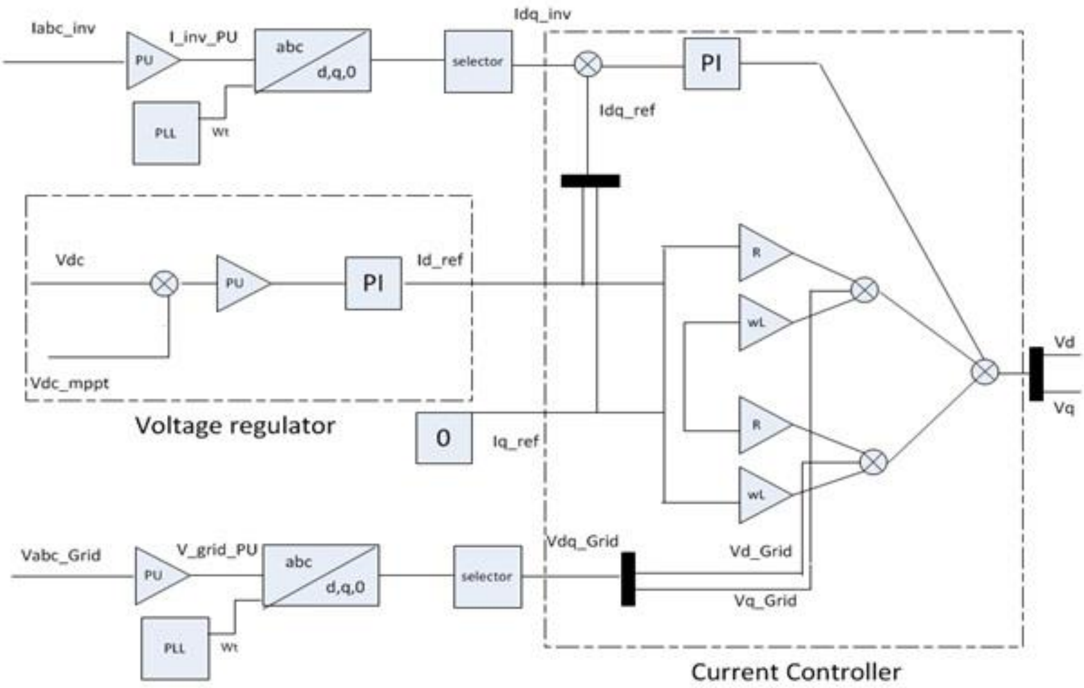

Figure 3.9 Detailed structure of the inverter closed loop controller [48]

3.5.2 SMC Based FFO-PID Controller

3.5.2.1 Fractional-Order PID Controller

The lack of a solution for fractional-order (FO) differential equations and a simple geometric explanation helped to develop the FO calculus to solve complex problems. The FO calculus constitutes the branch of mathematics dealing with differentiation and integration under an arbitrary order of the operation, i.e., the order can be any natural or even complex number, not only the integer [50].In comprehending its theoretical and real-world presentations in many fields, such as astronomy and industrialization problems, FO calculus can express many phenomena that cannot be expressed when using the classical method. FO calculus relates to fractional dimension infinite memory and chaotic behavior. FO calculus can be applied to electronics, control theory, and many other fields [51][52]. With the increase of the research in this field, increasing concentration has been directed to the modification of FO calculus as a successful modeling tool for intricate systems, which gives impetus to innovation in dynamical investigation and regulation. FO calculus appears to be plausibly contestant to incorporate larger exemplars through detaching graceful dependent on the explanation of involvedness [53]. Incorporating the FO calculus into control strategies of the systems can improve the control system dynamic performance with less control effort [54][55].

3.5.2.2 Fuzzy Fractional-Order PID Controller

Fuzzy logic works using linguistic notation, as it gives flexibility in expression in accessible language and helps to solve fuzzy problems in complex systems. A closed-loop control system can be considered as one of the best environments for implementing a fuzzy based control scheme, especially when high nonlinearity between inputs and outputs is available. The working principle of a classic controller relies on the fixed gains of the controller, such as constant-parameter PID controller. Therefore, the required control performance may not be always acquired for nonlinear and complex systems [56]. With this respect, the gains of a FO calculus based PID (FO-PID) controller can be dynamically adjusted using fuzzy logic concept [56]. In this study, such a controller is proposed and named as "Fuzzy FO-PID Controller" or "(FFO-PID)". In this controller, the gains of the PID controller are dynamically adjusted online using a Mamdani type fuzzy logic theory. The FFO-PID controller is a group of rule-based fuzzy controls applied in the FO-PID controller. In this control strategy, the fuzzy logic concept uses the error and its derivative to calculate the scaling factor (gain) of the proportional, integral, and derivative terms in the PID controller. These scaling factors are updated online at each sampling period. The FFO-PID control structure is represented in Figure 3.14.

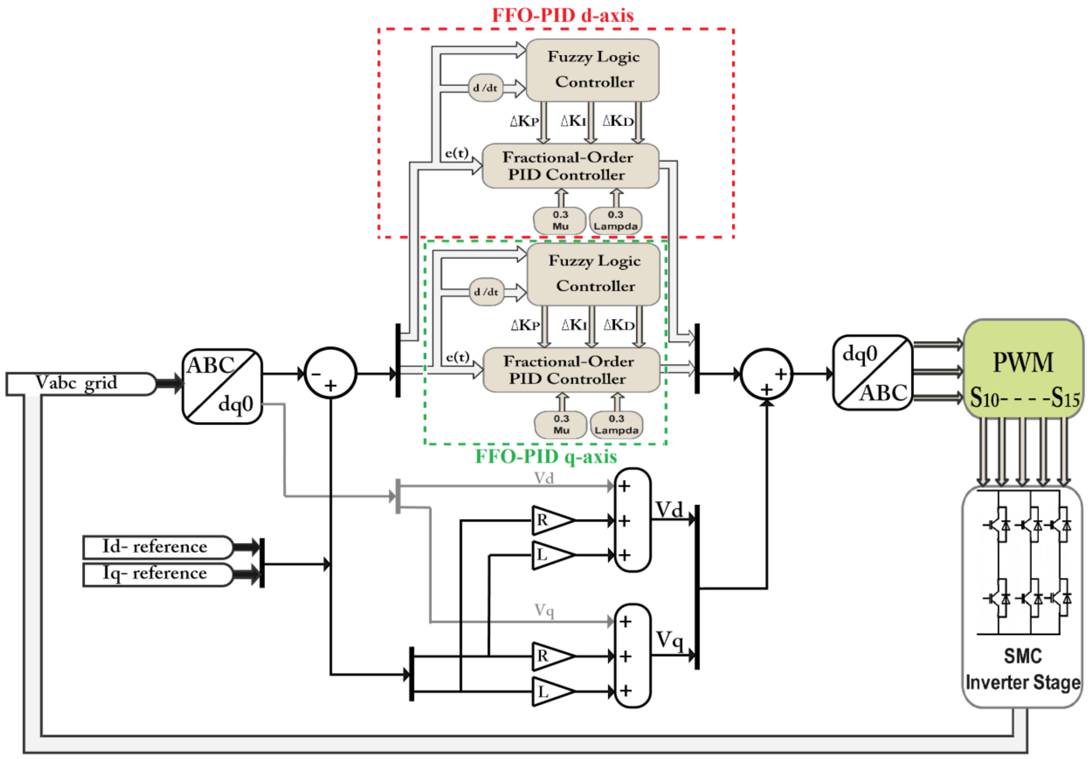

Figure 3.10 Block diagram of the FFO-PID controller used in this thesis

In this structure, the FO model can be obtained from integer-order model. There are numerous tools to specify the integer-order model. One of these tools is the Fractional-Order Modeling and Control (FOMCON) toolbox simulation environment [57]. When the FOMCON toolbox is used, the proposed system's FO model is specified with Grunwald-Letnikov simplification [58] and using the way described in [59] to achieve the FO model. The FO differential equation is transformed into a FO integral equation. Expanding the integral term creates a least-squares expression that allows the implicit time delay term to have an explicit appearance in the parameter vector. It helps to boost straightforward estimation of model parameters synchronously with a time lag. The active and reactive power injection to the grid from WECS is controlled using the FFO-PIF controller. The ABC signals for the FFO-PID controller are adjusted depending on the error and percentage change in error. These ratios are set for each component separately. The d-component represents the real active power injected to the grid. The q-component represents the reactive power injected to the grid. The FFOPID controller works to adjust the error values much faster and more accurately than PID, depending on the fractional order system. All of the details are explained in the fourth chapter of this thesis.

3.6 LCL Filter for SMC

To remove or reduce harmonic content due to high frequency switching of power semiconductor switches, an LCL filter can be employed at the SMC output. In this study, LCL type filter is chosen over L and LC type filters due to some advantages such as small inductor and capacitor size and superior high-frequency attenuation characteristics of -60 dB/dec [29]. However, no filter is used at the SMC input in this study.

3.7 The Final Form of the WECS

The final form of the WECS designed in this study is shown in Figure 3.16. The system contains several stages such as, wind turbine, PMSG, SMC, filter and the grid. The wind turbine is connected to the PMSG. The wind turbine is controlled by a control system based on pitch angle control to achieve maximum possible wind energy harvesting. On the other hand, the operational control protects the generator from high wind speeds. The output of the PMSG is connected to the rectifier stage of the SMC. The control of rectifier and inverter stages of the SMC are realized separately. The control part of the rectifier stage controls the switches (S1-S9) using SPWM scheme. On the other hand, the control part of the inverter stage controls the switches (S10-S15) using SPWM scheme. The output of the SMC is controlled in such a way that the magnitude as well as phase angle of the output voltage can be adjusted. The output of the SMC is connected to the LCL filter. The output of the LCL filter is connected to the grid through a coupling transformer

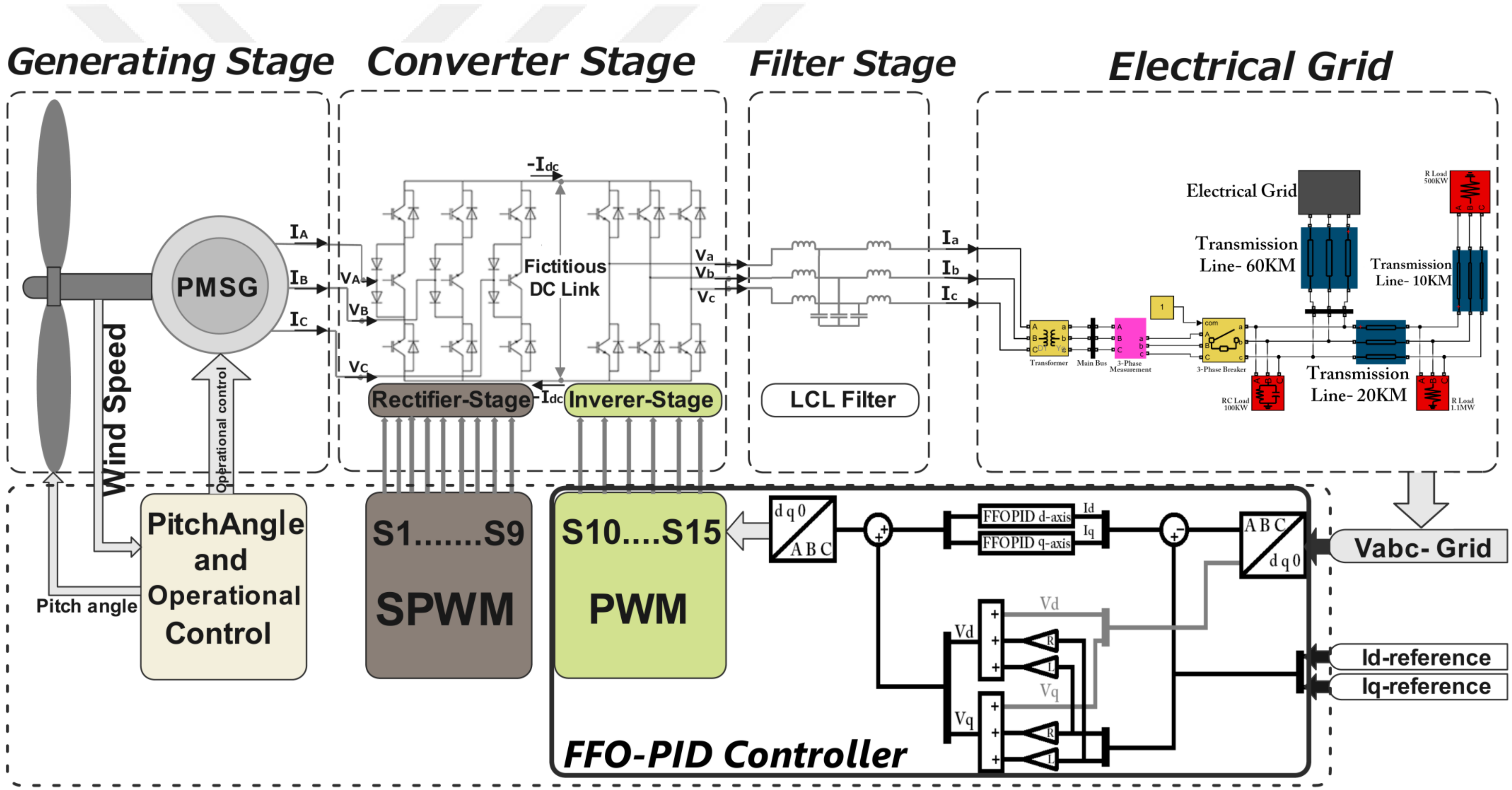

Figure 3.11 Schematic diagram of SMC-based WES and its controllers

3.8 The Summary

In this chapter, the focus is on SMC. The electrical circuit of the SMC was introduced. The derivation method for obtaining the SMC legs is presented. The SMC commutation with its types was also presented with the scheme for each type. The MC modulation strategies were introduced. The main classification of MC modulation techniques was introduced. SPWM (bipolar and unipolar) was introduced. The method for obtaining the PWM signals is presented by plotting the waveforms for both bipolar and unipolar cases. The SMC control structure is mentioned together with the main schematic as well as the equations for active and reactive power. The control mechanism designed in this thesis was also presented. The detailed structure of the inverter closed loop controller is mentioned when the PID is used. The SMC based FFO-PID controller was introduced. The FO and its mechanism of operation were briefly defined. FO was introduced after adding fuzzy logic as well. The main scheme of the FFO-PID controller that will be used in this thesis is mentioned along with its working mechanism. The LCL filter that will be used with the SMC has been mentioned. In the end, a main detailed outline of the WECS that will be designed for this work has been worked out through which the SMC will be operated. The detailed work in this scheme has been presented with mention of all stages, starting from the generation stage, then the converter stage, the filter stage, and finally the stage of injection active and reactive power into the electrical grid. The detailed of the electrical grid was also presented inside of the main scheme.

CHAPTER IV

MODELING AND SIMULATION OF PMSG BASED WECS

4.1 SMC Design

The power circuit of the three-phase SMC used in the simulation environment is shown in Figure 4.1. This figure includes the main stages of the SMC. The first stage of the SMC is the rectifier stage, which consists of three legs. Each leg contains a 3-bidirectional switch. The first switch consists of one IGBT and one diode on the top, the second switch of one IGBT and two diodes in the middle, and the third switch of one IGBT and one diode on the bottom. The input terminal of the rectifier stage is connected to the voltage source, and the voltage source here is represented later by WECS. The output terminal of the rectifier stage is DC voltage. We note here that there is no element storage to store the DC value generated by the RS, such as the inductor or capacitance, and this is the main feature of the SMC. The second stage of the SMC is the inverter stage, which consists of three legs. Each leg contains a 2-bidirectional switch. The first switch consists of one IGBT and one Diode on the top, and the second switch of one IGBT and one Diode on the bottom. The inverter stage is controlled to inject active and reactive power into the grid at the end. The input terminal of the inverter stage is the DC output voltage from rectifier stage, and the output terminal of the inverter stage is the AC output voltage. The output terminal of the inverter stage is connected to the LCL filter in order to deal with the signal coming out of the SMC to reduce the total harmonic distortion. The generated power after the filter stage is injected into the grid. The parameters used in designing the rectifier and inverter stages of the SMC are represented in Table 4.1.

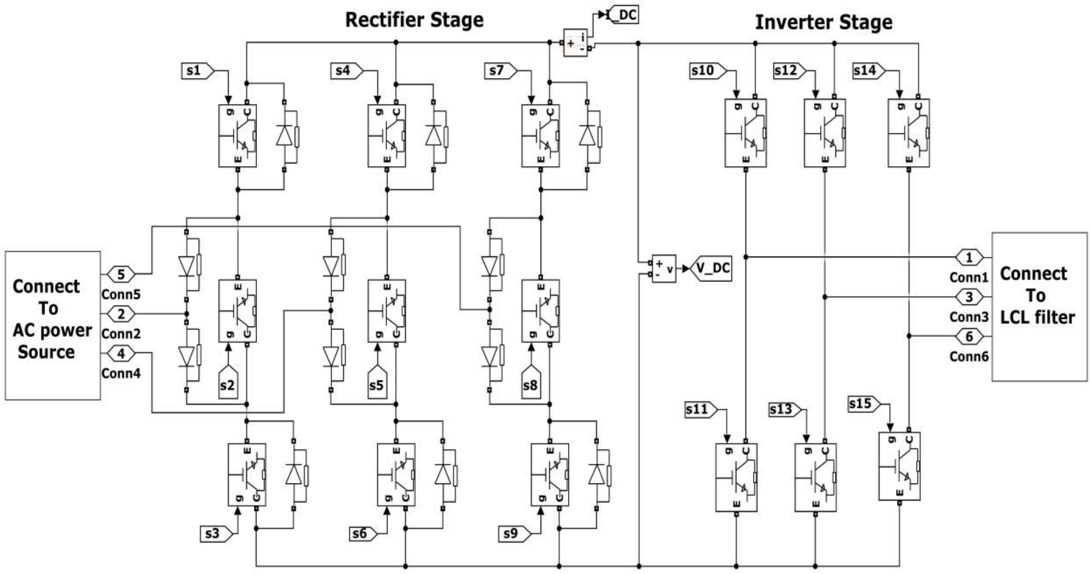

Figure 4.1 Simulink model of SMC showing rectifier and inverter stages

Table 4.1 The IGBT and diode parameters used in SMC design

Parameter	IGBT	Diode
Resistance Ron (Ω)	0.001	0.001
Inductance Lon (H)	0	0
Forward voltage drop (V)	1	0.8
Initial current(A)	0	0
Snubber resistance Rs (Ω)	1e5	500
Snubber capacitance Cs (F)	inf	250e-9

4.1.1 SMC Rectifier Stage Design

A SPWM model is constructed as shown in Figure 4.2 to control the IGBT bidirectional switches (S1-S9) of the rectifier stage of the SMC. In SPWM scheme, a high frequency carrier signal (triangular or saw tooth) is required to be compared with a sinusoidal reference signal. The construction of the carrier signal for the rectifier stage is realized using the data provided in Table 4.2. In Table 4.1, the switching instants of the carrier signal is given. Note that the switching frequency of the SPWM scheme for the rectifier stage is adjusted as 50 kHz. The rectifier stage is controlled in an open loop manner in which there is no feedback signal is used. This greatly simplifies the rectifier control design.

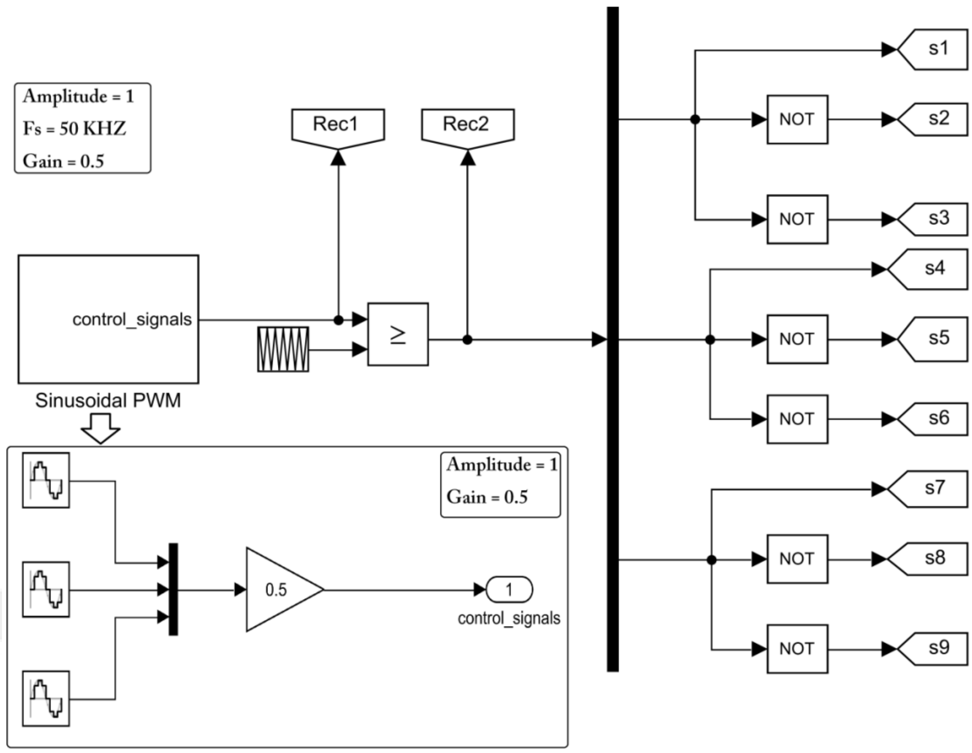

Figure 4.2 SPWM model for SMC rectifier stage

Table 4.2 Repeating switching sequence for carrier signal formation for the rectifier stage of the SMC

Time values	0	0.25/50e3	0.5/50e3	0.75/50e3	1/50e3
Output values	1	0	1	0	1

4.1.2 SMC Inverter Stage Design

The inverter stage is the second stage of the SMC. This stage is controlled by SPWM scheme like the rectifier stage as shown in Figure 4.3. But unlike the rectifier stage, the inverter stage is closed loop controlled in which feedback signals are employed. The FFO-PID is used in this stage to control the system parameters such as current and voltage. Table 4.3 shows the repeating switching sequence for carrier signal formation for the rectifier stage of the SMC. Note that the switching frequency of the SPWM scheme for the inverter stage is adjusted as 25 kHz. At this stage of the work, the open loop control system was used with SMC inverter stage. But after combining the SMC together with the WECS, a closed loop control system will be used. The mechanism of closed loop control system work depends on the PID or FFOPID controller. This will be explained later in the control section.

Table 4.3 Repeating switching sequence for carrier signal formation for the inverter stage of the SMC

Time values	0	1/25e3
Output values	1	-1

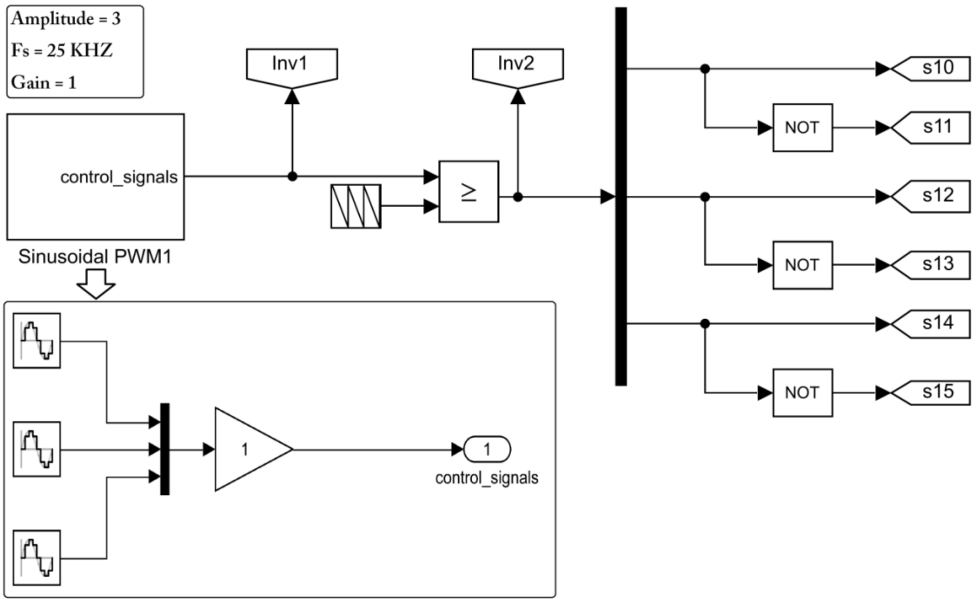

Figure 4.3 SPWM model for SMC inverter stage

4.2 LCL Filter Design

To improve the output waveform quality of the SMC output, an LCL filter used is used in this work. The LCL model is shown in Figure 4.4. The input of the LCL is connected to the SMC output, while the output of the LCL filter is connected to the grid (usually after a coupling transformer). The LCL filter parameters are designed as follows: The left inductor is 0.6 mH, the right inductor is 51 mH, the shunt capacitor is 22 μF.

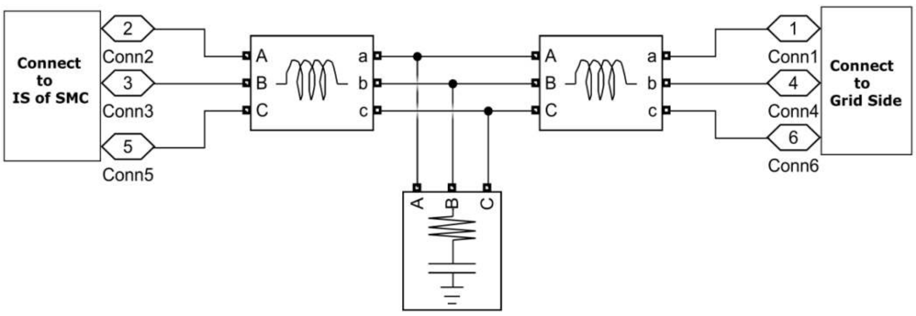

Figure 4.4 LCL filter model

4.3 The Final Design of SMC Connected to 3-Phase AC Source

The simulation model for testing and verifying the SMC is shown in Figure 4.5. This model is the first step of the simulation studies. The rectifier stage of the SMC is powered by a three-phase constant 50 Hz AC voltage source with a line-to-line rms voltage of 537V. In this model, the three-phase voltage source represents the output of the PMSG. The load at the output is a three-phase Y-connected RC load. The load parameters are R=16 Ω and C= 10 μF. In this study, the SPWM scheme is adapted for producing the control signals of the power semiconductor switches, both in the rectifier and inverter stages. The controllers here are of the open-loop type. It is intended to test the operation of the SMC before it is connected to the PMSG-WECS. In this case study, the measurements are taken both before and after LCL filter.

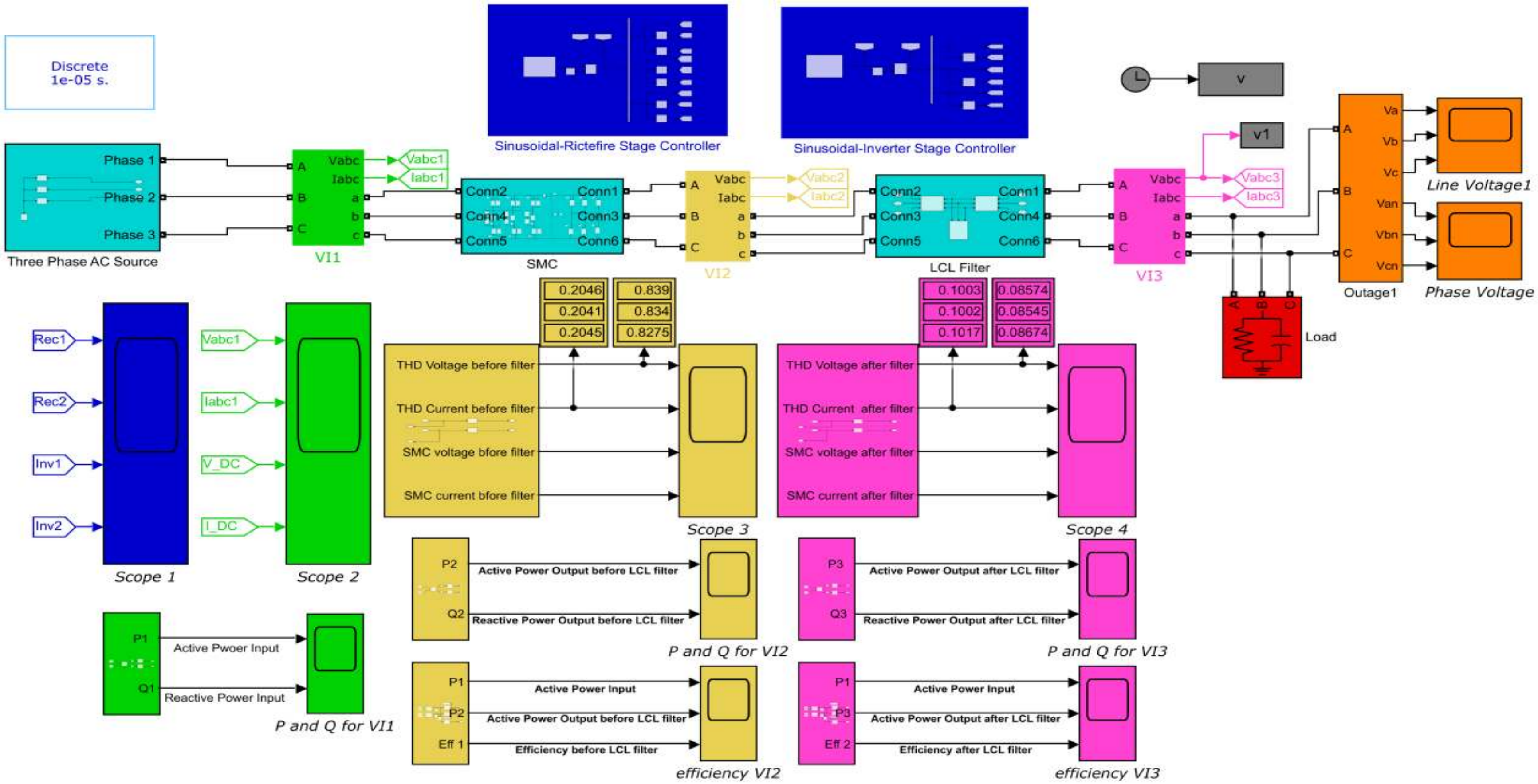

Figure 4.5 The general model of the designed PMSG based WECS

4.4 The Simulation Results: SMC is feeding a load

This section presents time-domain simulation results of three-phase SMC feeding a three-phase purely resistive load when it is fed by a constant three-phase voltage source. For these simulations, the rectifier and inverter stage gain are set to 0.5 and 1, respectively. The amplitudes of the rectifier and inverter stage are tuned to 1 and 3, respectively. The switching frequency of rectifier and inverter stage is set to 50 kHz and 25 kHz, respectively. The results are obtained with a goal of reducing THD of current and voltage waveforms at the output of the SMC as minimum as possible by adjusting the parameters of the rectifier and inverter stages. In this simulation studies, LCL filter is also used at the output of the SMC to reduce the harmonic content. Both rectifier and inverter of the SMC employs SPWM scheme to generate the control signals for the power semiconductor switches. Figure 4.6 depicts the active and reactive power measurements at the SMC output before LCL filter. On the other hand, Figure 4.7represents the input voltage and current waveforms of the SMC, respectively. Since, no filter is used at the SMC input, the current waveforms contain some switching noise and harmonics due to the rectifier semiconductor switching.

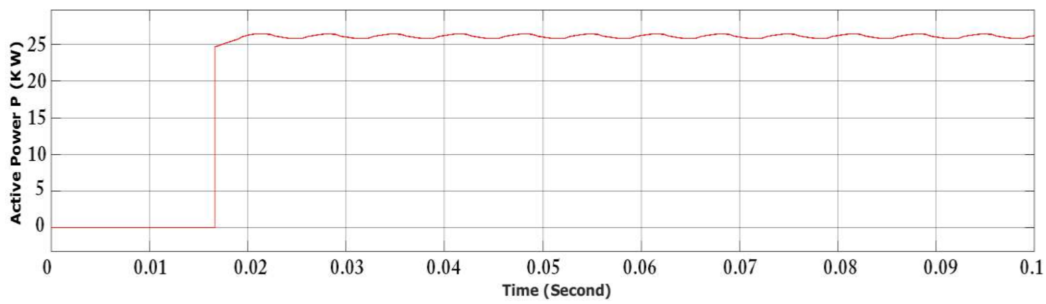

(a)

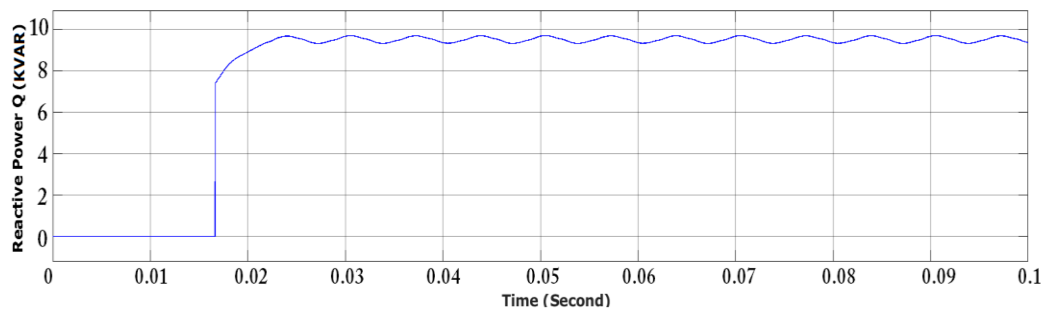

(b)

Figure 4.6 Active and reactive power measurements at the SMC output before LCL filter: (a) active power, (b) reactive power

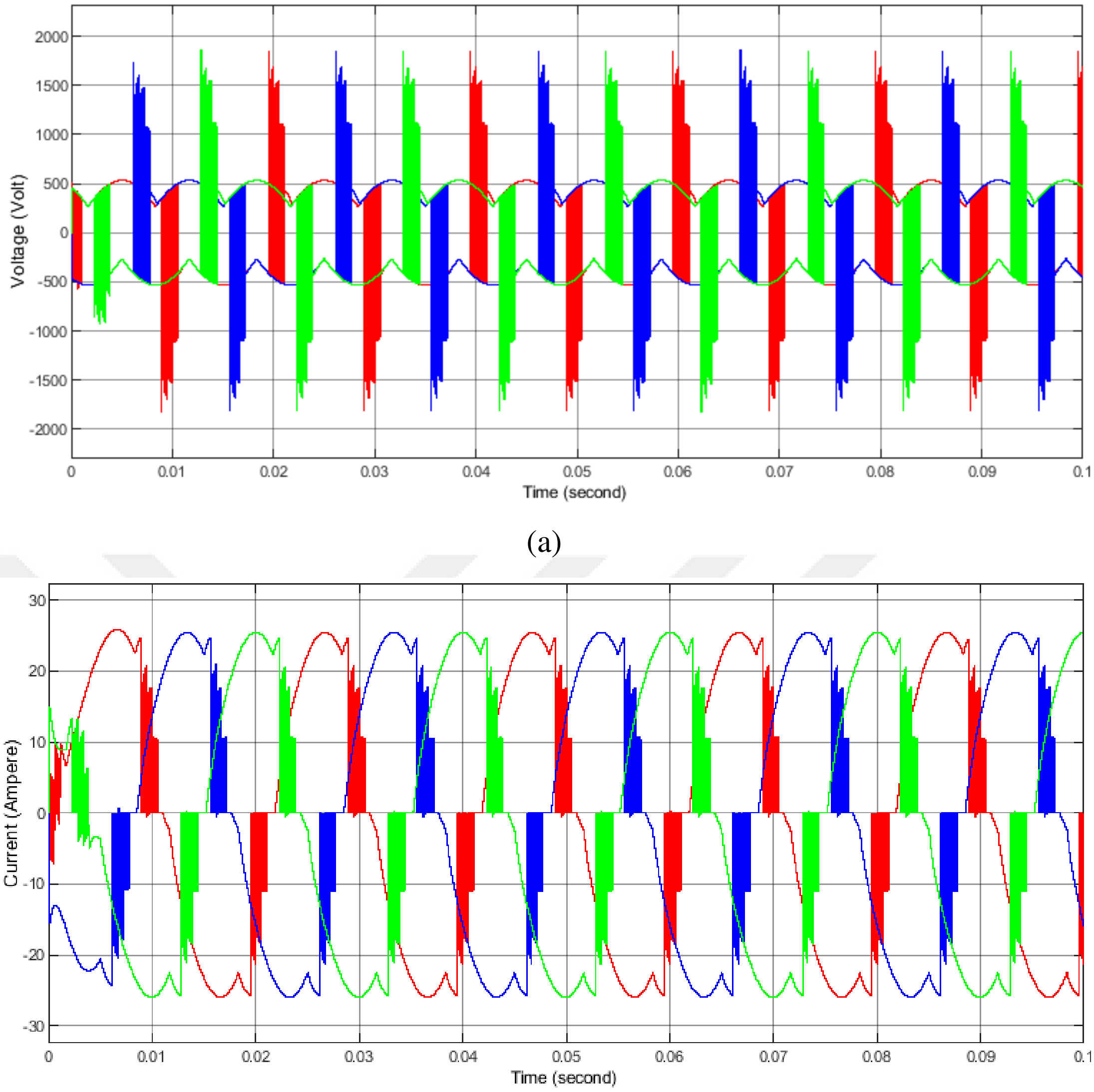

(a)

(b)

Figure 4.7 The input voltage and current waveforms of the SMC: (a) voltage waveform, (b) current waveform

Figure 4.8 (a) and (b) represents THD measurements for voltage and current waveforms of the SMC output before LCL filter. The following comments are given. The THD values presented in Figure 4.8 are relatively high. This is due to the lack of LCL filtering. The switching harmonics negatively affect the output waveform quality. The THD of the current waveform is very high which is more than 80%. On the other hand, the THD of the voltage waveform is again very high which is more than 20%. Both of these results are not practically accepted. Figure 4.9 shows the efficiency measurement of the SMC before LCL filter. It can be observed that the final value of the efficiency when no filter is used is around 95%.

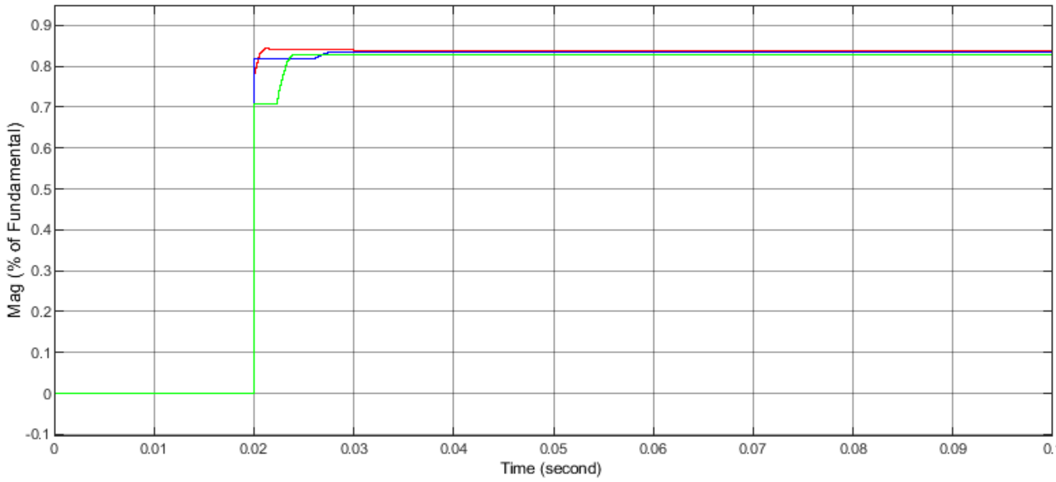

(a)

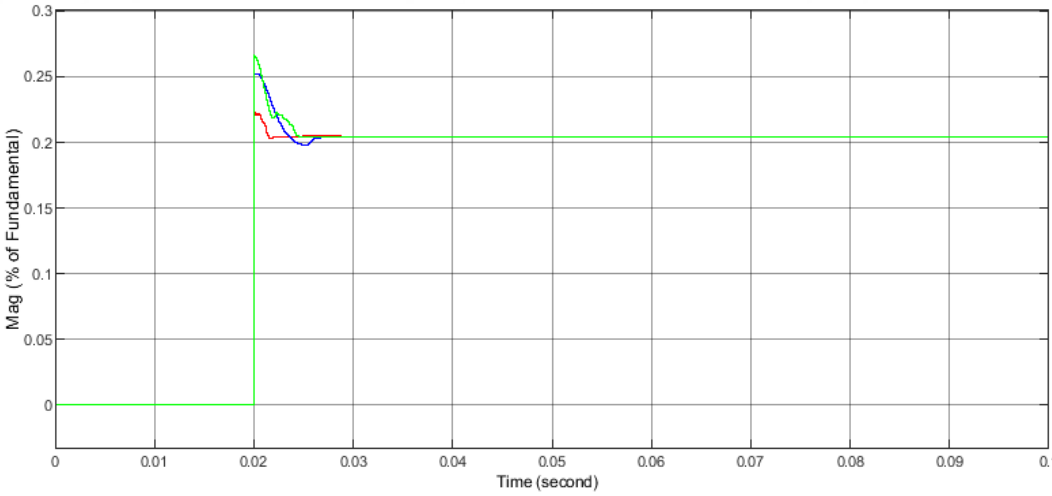

(b)

Figure 4.8 THD measurements for voltage and current waveforms of the SMC output before LCL filter:(a) voltage THD, (b)current THD

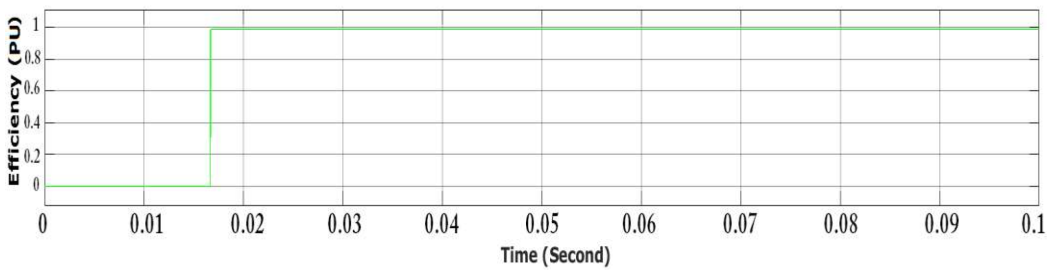

Figure 4.9 The efficiency measurement of the SMC before LCL filter

Figure 4.10 depicts the active and reactive power measurements at the SMC output after LCL filter. When these results are compared with Figure 4.6, the following comments can be made. The active power shown in Figure 4.10 (a) seems lower after using the LCL filter. This result can be acceptable since with the usage of LCL filter, the THD values are greatly reduced. More quality waveforms are now being injected into the electrical grid or the load. When comparing the reactive power shown in Figure 4.6 (b) and Figure 4.10 (b), the following comments can be made. The decrease in the reactive power can be seen in Figure 4.10 (b) to -3kVAR compared to the one shown in Figure 4.6 (b), where this value is 10 kVAR. Here the role of the filter becomes clear again in reducing the value of the reactive power.

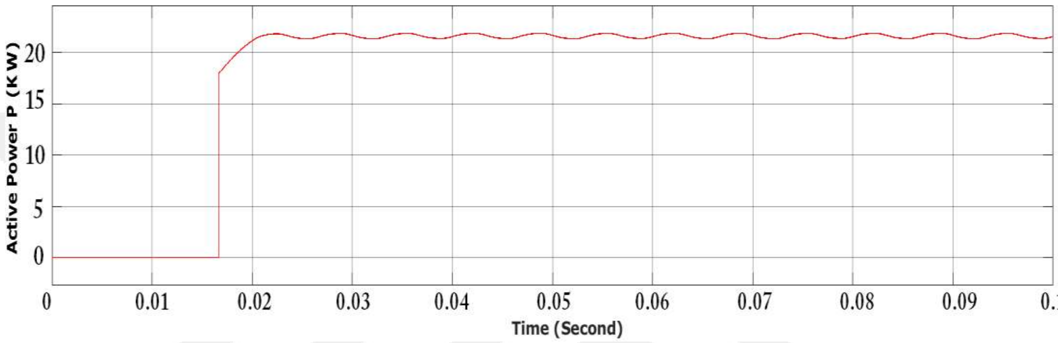

(a)

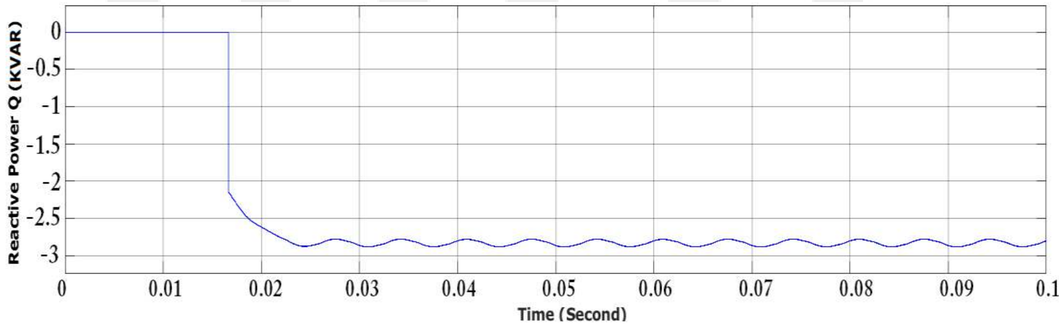

(b)

Figure 4.10 Active and reactive power measurements at the SMC output after LCL filter: (a) active power, (b) reactive power

Figure 4.11 shows the output voltage and current waveforms of the SMC after LCL filter. For Figure 4.11 (a) and (b), the following comments can be made. The value of the THD decreases a lot after using the LCL filter. The voltage waveform shown in Figure 4.11 (a) looks like almost pure sinusoidal waveform with a peak value of around 410V. Similarly, the current waveform shown in Figure 4.11 (b) again looks like almost pure sinusoidal waveform with a peak value of around 27A. Figure 4.12 represents the THD measurements for voltage and current waveforms of the SMC output after LCL filter. THD measurements before the LCL filter indicate a THD of 0.83% for the SMC output voltage and with a THD of 0.2% for the SMC output current. On the other hand, the THD of SMC output voltage is reduced to 0.08%, while the THD of the SMC output current is reduced to 0.1% by using the LCL filter. It can be clearly concluded that with the use of LCL filter, the THD of voltage and current waveforms at the SMC output is clearly obtained as a lower value. The LCL filter reduces the switching noise and harmonics in both waveforms.

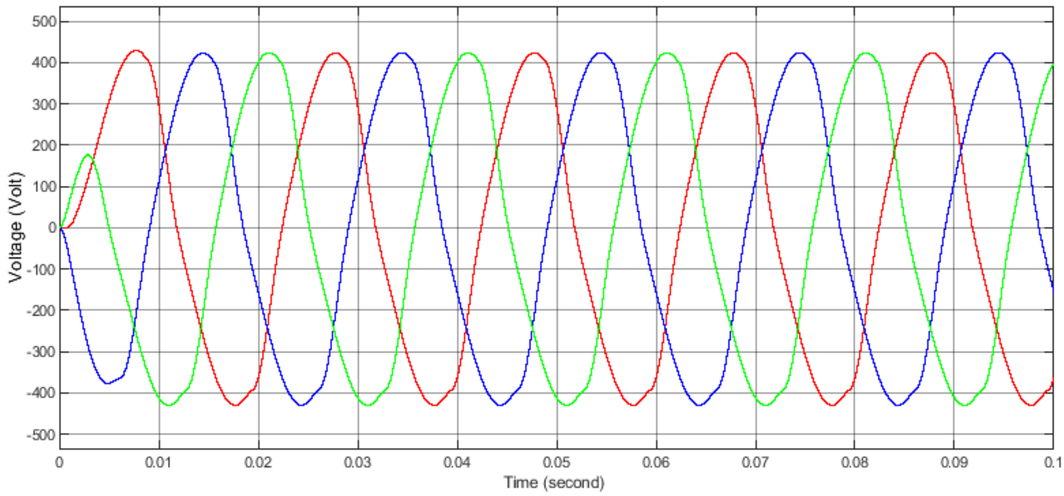

(a)

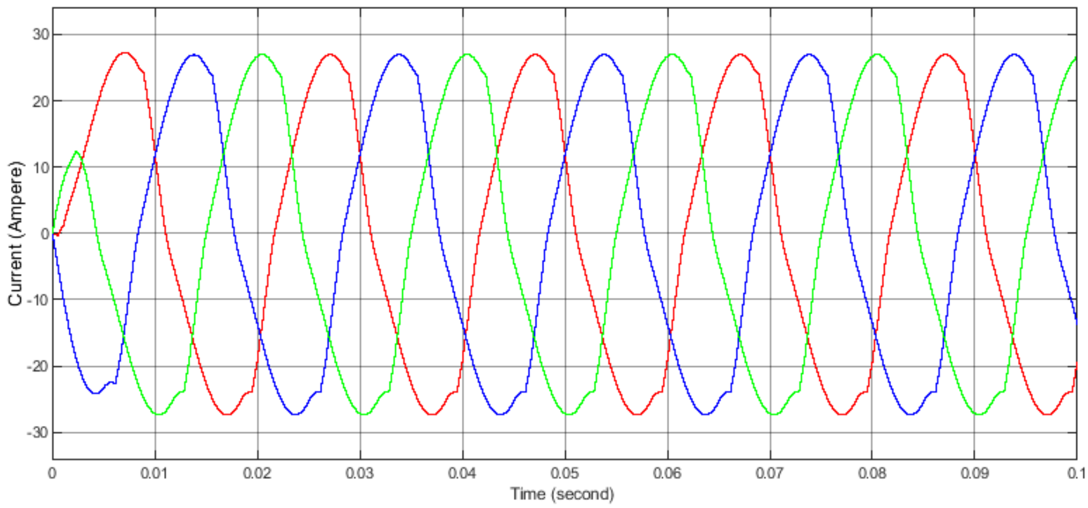

(b)

Figure 4.11 The output voltage and current waveforms of the SMC after LCL filter: (a) voltage waveform, (b) current waveform

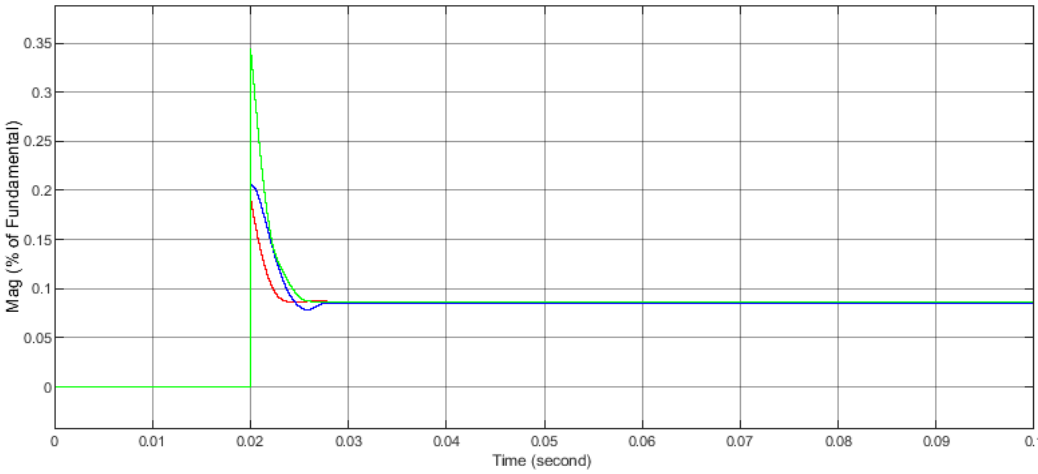

(a)

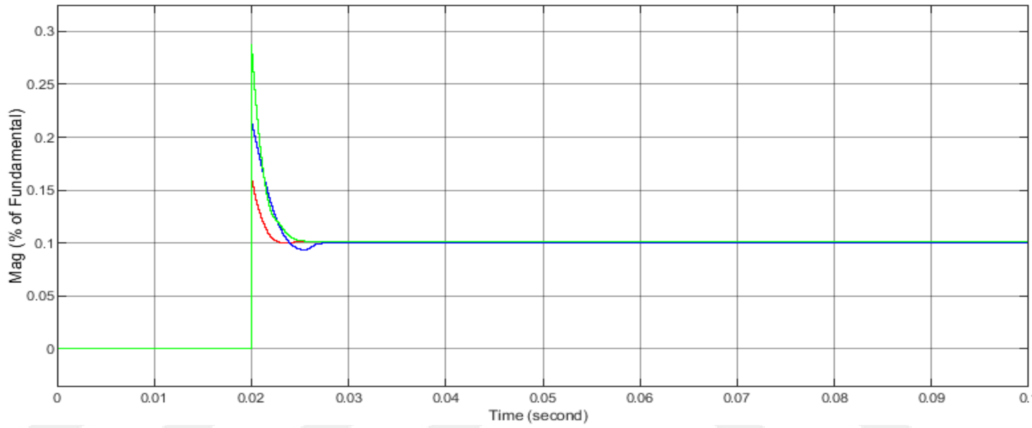

(b)

Figure 4.12 THD measurements for voltage and current waveforms of the SMC output after LCL filter: (a) voltage, (b) current

Figure 4.13shows the efficiency measurement of the SMC after LCL filter. When comparing the efficiency value in Figure 4.13 after using the LCL filter with the efficiency value shown in Figure 4.9 before using the LCL filter, we will notice that the efficiency becomes around 85% after using the LCL filter.

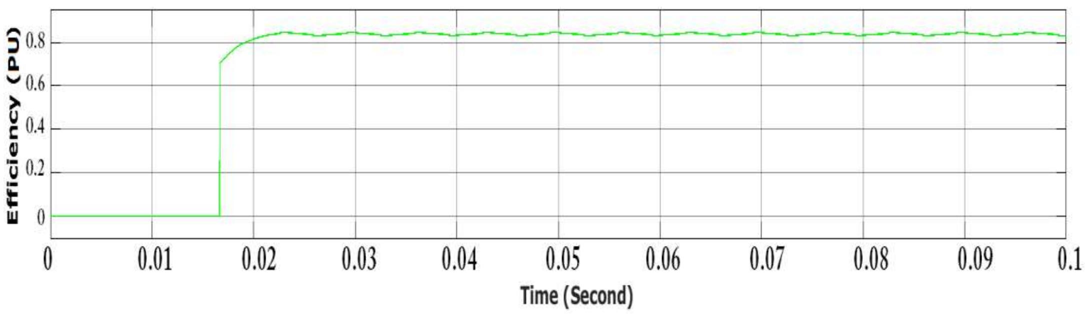

Figure 4.13 The efficiency result after LCL filter

The voltage and current waveforms at the input of rectifier stage of SMC are represented in Figure 4.14 (a) and (b), respectively. From Figure 4.14, the following observations are made. The voltage waveform is almost pure sinusoidal waveform as shown in Figure 4.14 (a). On the other hand, the current waveform contains some distortions as shown in Figure 4.14 (b). However, the THD values are greatly decreased after using the LCL filter.

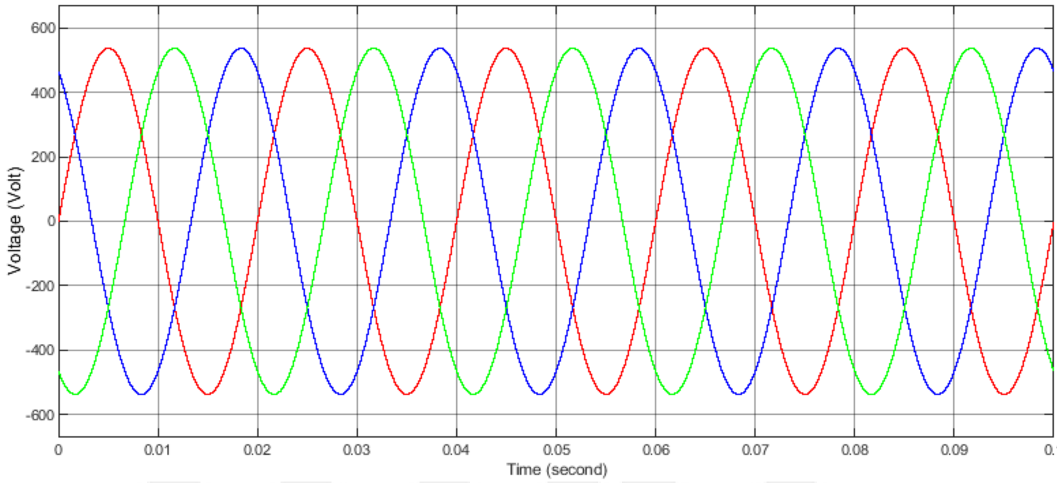

(a)

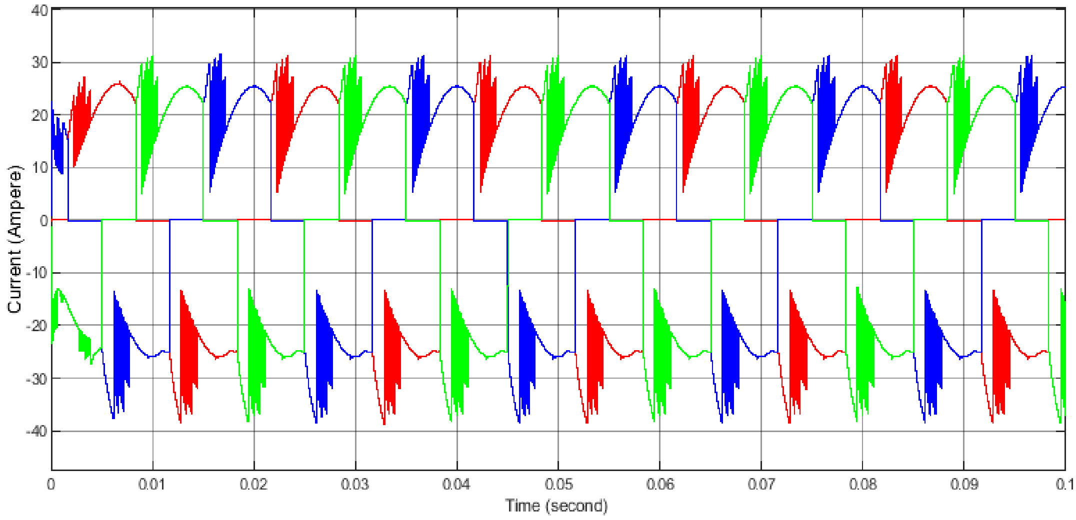

(b)

Figure 4.14 The voltage and current waveforms at the input of rectifier stage of SMC: (a) voltage, (b) current

The voltage and current waveforms of fictitious DC link of SMC are shown in Figure 4.15. It is seen that the DC voltage waveform has a ripple factor of 6.75% with an average value of around 860 V.

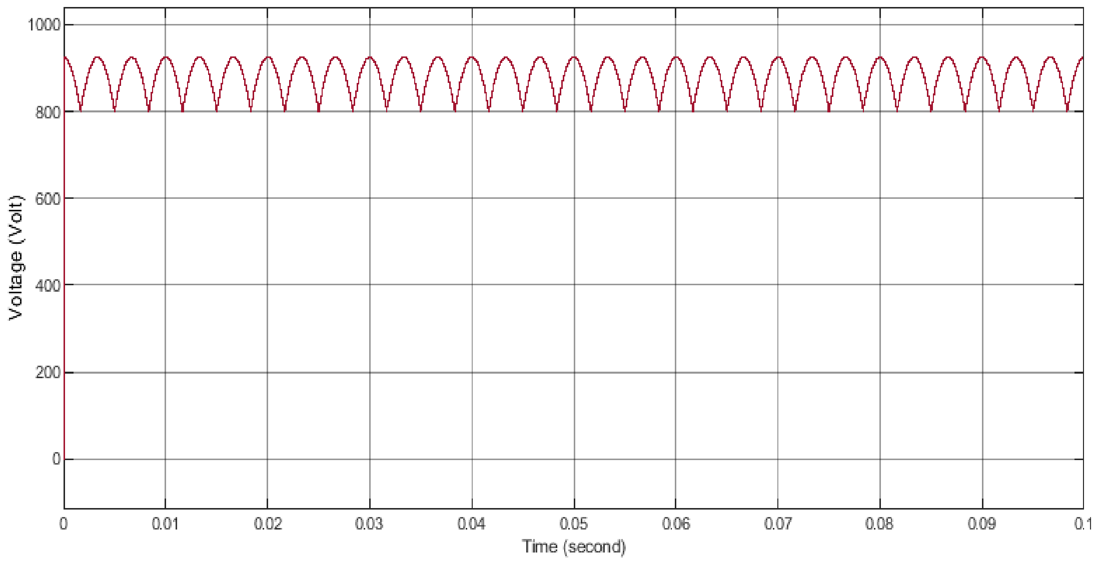

(a)

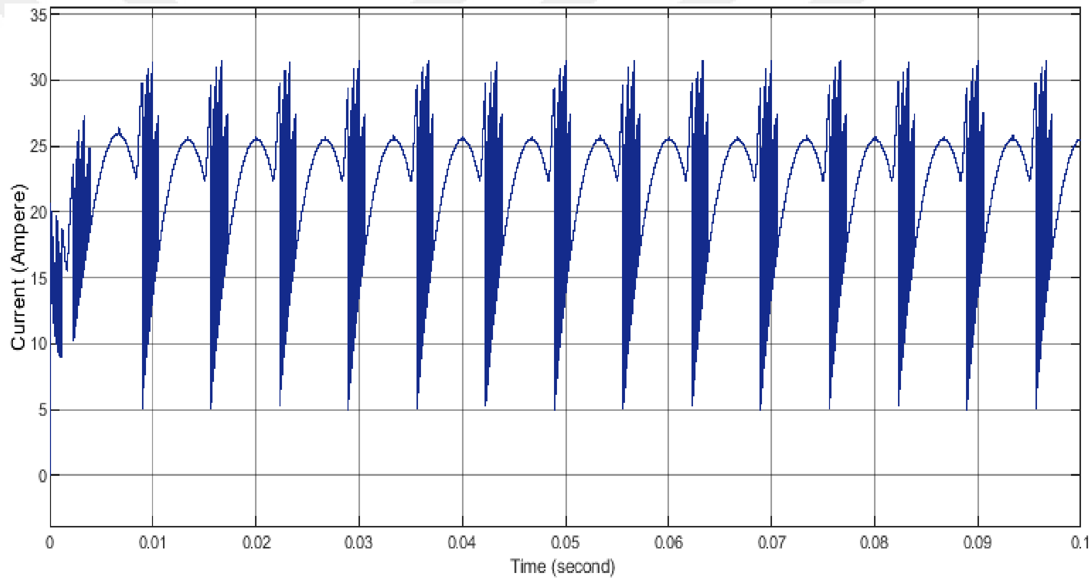

(b)

Figure 4.15 The voltage and current waveforms of fictitious DC link of SMC: (a) voltage, (b)current

Figure 4.16 depicts the real and reactive power at the input of rectifier stage of SMC. From Figure 4.16 (a) and (b), the following details can be observed. Figure 4.16 (a) represents the active power supplied from the three-phase AC source and its value is around 26 kW, where the AC power source is connected with the SMC to the rectifier stage. On the other hand, Figure 4.16 (b) represents the value of the supplied reactive power to the rectifier stage of SMC.

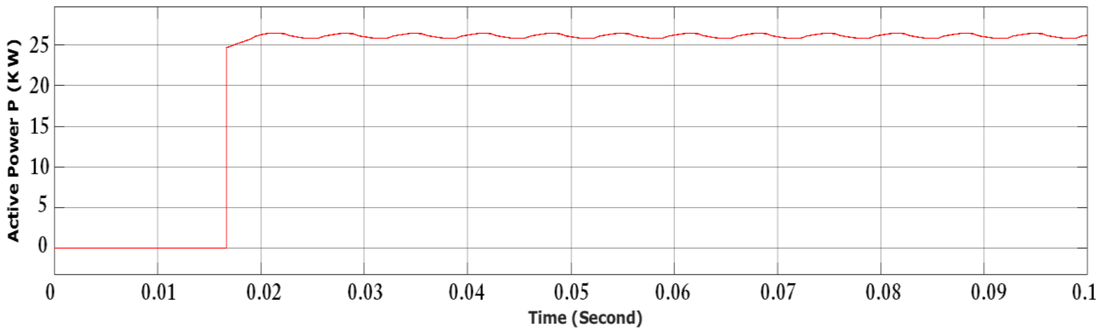

(a)

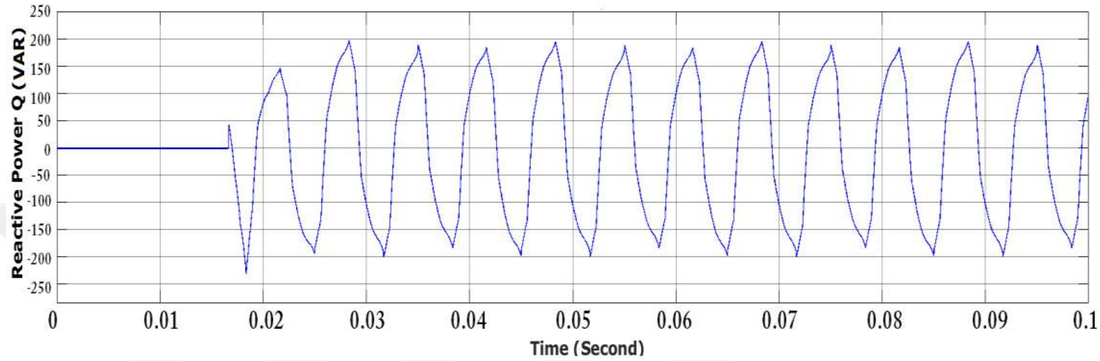

(b)

Figure 4.16 The real and reactive power at the input of rectifier stage of SMC: (a) active power, (b) reactive power

The SPWM control signals for rectifier and inverter stages of SMC are represented in Figure 4.17. These signals are compared with high frequency carrier signals to generate control signals for power semiconductors in rectifier and inverter stages. The resulting SPWM signals are shown in Figure 4.18.

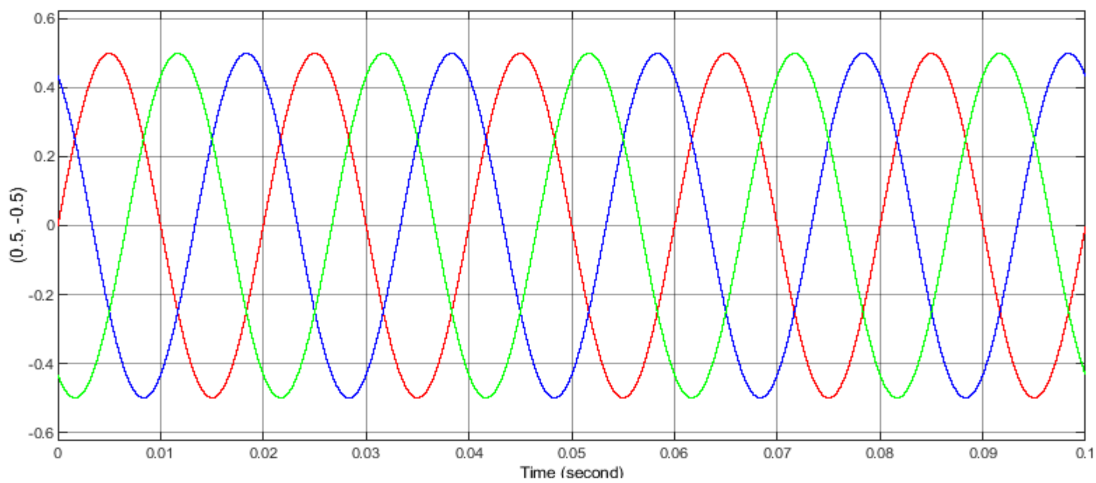

(a)

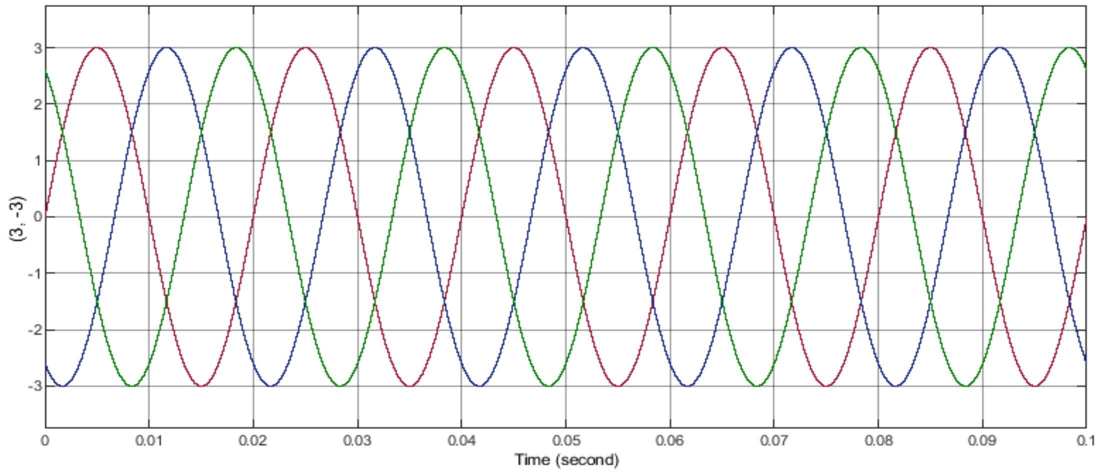

(b)

Figure 4.17 The SPWM control signals: (a) for rectifier; (b) for inverter

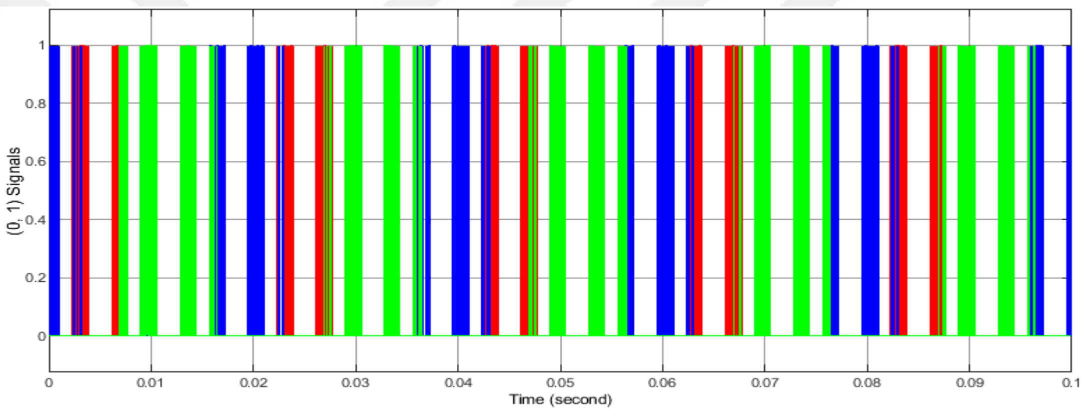

(a)

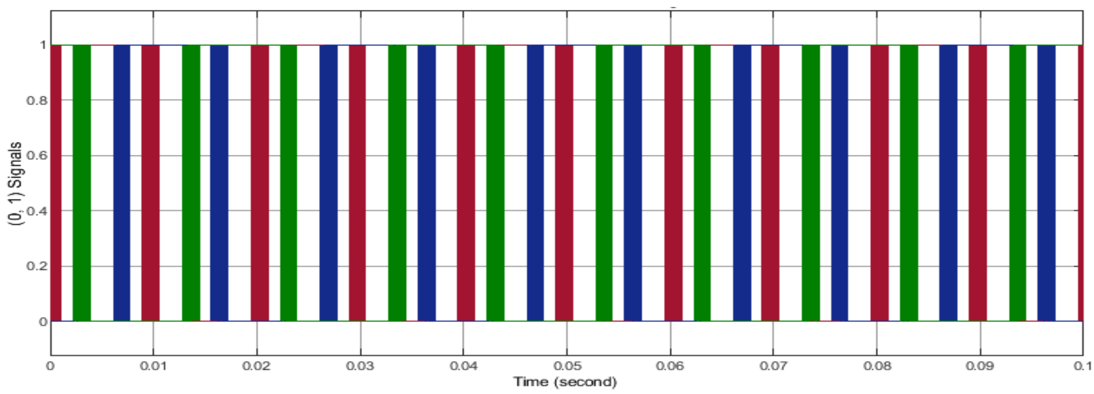

(b)

Figure 4.18 SPWM control signals: (a) for rectifier, (b) for inverter

Figure 4.19 and Figure 4.20 respectively represents the line-to-line and line-to-neutral voltage waveforms at the output of the SMC.

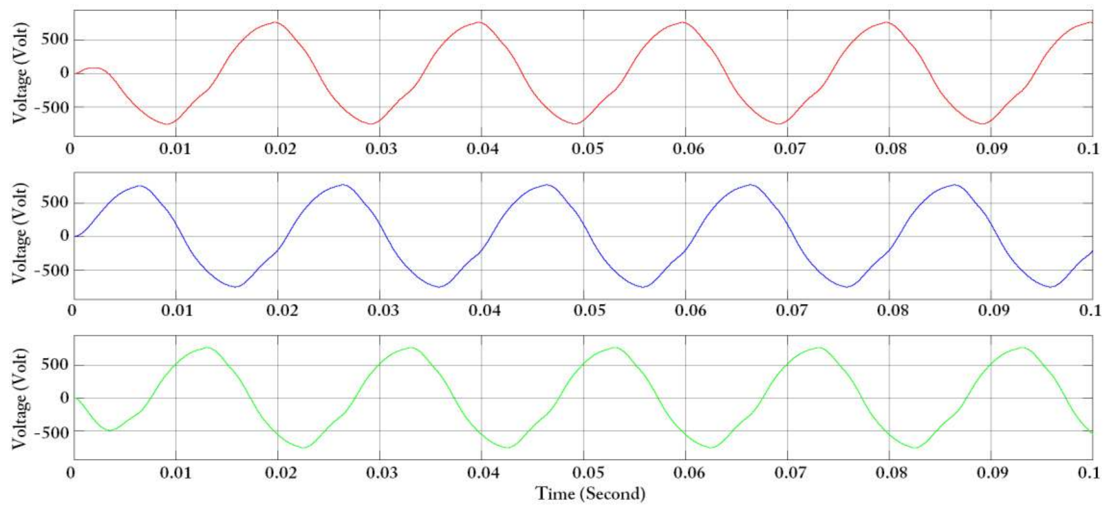

Figure 4.19 Line voltage Va, Vb, Vc

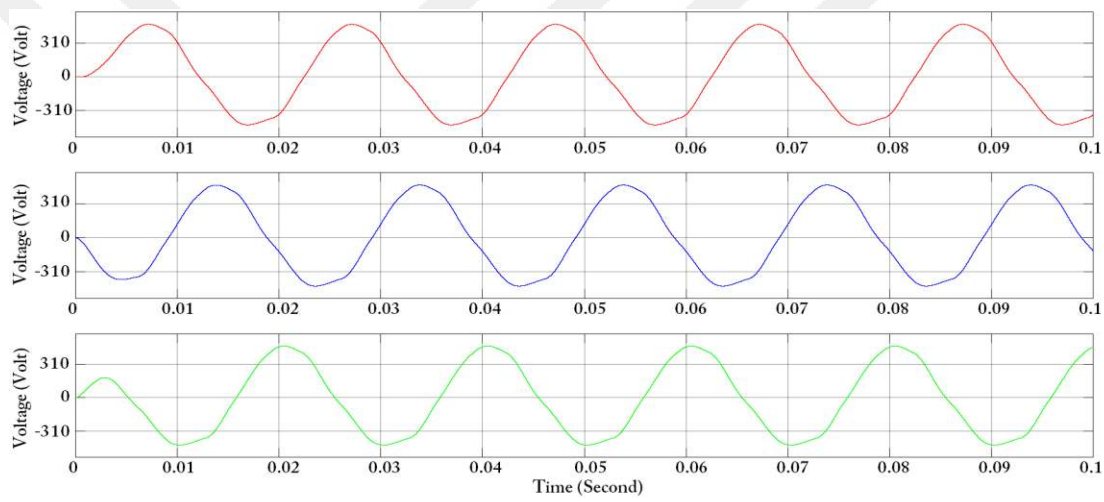

Figure 4.20 Phase voltage Van, Vbn, Vcn

4.5 SMC Output Voltage Control

The simulation studies also investigate the changes in SMC output voltage by changing the rectifier/inverter gains and amplitudes. Table 4.4 shows the changes in SMC output voltage for different values of rectifier and inverter gains. In this case study, the amplitude of the rectifier and inverter stage is tuned to 1. The rectifier switching frequency is tuned to50 kHz, while the inverter switching frequency is tuned to 25 kHz. The highest output voltage is obtained as 142 V when both rectifier and inverter gains are adjusted to 1.

Table 4.5 lists the changes in SMC output voltage for different values of rectifier and inverter amplitudes when the rectifier switching frequency is tuned to 50 kHz and the inverter switching frequency is tuned to 25 kHz. In this case study, the gain of the rectifier and inverter stage is tuned to 1. The highest output voltage is obtained as 425.5 V when the rectifier gains are adjusted to 1and the inverter gain is adjusted to 5. Table 4.6 presents the changes in SMC output voltage for different values of rectifier and inverter switching frequencies. In this case study, the gain and amplitude of the rectifier are adjusted to 1 and 0.5, respectively. In this case study, gain and amplitude of the inverter are adjusted to 5 and 1, respectively. From Table 4.6, it can be concluded that if a higher output voltage is needed, relatively high switching frequencies for rectifier and inverter can be used. However, this situation increases converter switching losses, so the designer should consider a trade-off between the high output voltage and low losses.

Table 4.4 The change in SMC output voltage for different values of the rectifier and inverter gains (rectifier Fs is 50 kHz, inverter Fs is 25 kHz)

Rectifier Gain (G)	Inverter Gain (G)	Output Voltage (Under Load)
1	1	142
1	0.5	31.37
1	0.2	31.37
1	0.1	31.37
0.5	1	143.7
0.2	1	143.7
0.1	1	143.7
0.5	0.5	31
0.2	0.2	31

Table 4.5 The change in SMC output voltage for different values of rectifier and inverter amplitudes (rectifier Fs is 50 kHz, inverter Fs is 25kHz)

Rectifier Amplitude	Inverter Amplitude	Output Voltage (Under Load)
0.5	1	170
1	1	142
2	1	6.5
1	0.5	31.37
1	2	420.5
1	3	424.3
1	5	425.5
0.5	0.5	31.37
2	2	54.9
3	3	66.8

Table 4.6 The change in SMC output voltage for different values of rectifier and inverter switching frequencies (the gain and amplitude of the rectifier are 1 and 0.5, the gain and amplitude of the inverter are 5 and 1)

Rectifier (f_s)	Inverter (f_s)	Output Voltage (Under Load)
50	50	425.5
50	40	426.4
50	30	426.8
50	20	425.8
50	25	426
40	50	238.4
30	50	211.1
20	50	238.8
25	50	155.8

4.6 SMC Efficiency Evaluation

The efficiency of SMC is evaluated by changing modulation indices such as gain, amplitude, and switching frequency. Table 4.7, Table 4.8, and Table 4.9lists the changes in SMC efficiency for different values of rectifier and inverter amplitudes. It is observed that around 98% of SMC efficiency is measured which can be considered sufficient for the given parameter settings.

Table 4.7 The change in efficiency of SMC for different values of rectifier and inverter gains (rectifier Fs is 50 kHz, inverter Fs is 25 kHz)

Rectifier Gain (G)	Inverter Gain (G)	SMC efficiency before LCL filter	SMC efficiency after LCL filter
1	1	98.8	58
1	0.5	98.43	16.5
1	0.2	98.43	16.5
1	0.1	98.43	16.5
0.5	1	98.8	58
0.2	1	98.8	58
0.1	1	98.8	58
0.5	0.5	98.43	16.5
0.2	0.2	98.43	16.5

Table 4.8 The change in efficiency of SMC for different values of rectifier and inverter amplitudes (rectifier Fs is 50 kHz, inverter Fs is 25 kHz)

Rectifier Amplitude	Inverter Amplitude	SMC efficiency before LCL filter	SMC efficiency after LCL filter
0.5	1	98.8	58
1	1	98.8	58
2	1	98.8	68
3	1	98.8	68
1	0.5	98.4	16.5
1	2	98.9	79.5
1	3	98.9	82.5
1	5	98.9	85
0.5	0.5	98.4	16.5
2	2	98.8	16.5
3	3	98.8	83

Table 4.9 The change in efficiency of SMC for different values of switching frequencies (gain and amplitude of rectifier is1 and 0.5, gain and amplitude of inverter is5 and 1

Rectifier (f_s)	Inverter (f_s)	SMC efficiency before LCL filter	SMC efficiency after LCL filter
50	50	98.9	85
50	40	98.9	85
50	30	98.9	84.9
50	20	98.9	85
50	25	98.9	85
40	50	96.3	79
30	50	95.4	78.5
20	50	96.2	79
25	50	94.9	77.5

4.7 SMC THD Performance Evaluation

The different changes in THD of voltage and current waveforms under load by changing modulation indices (gain, amplitude, and frequency of switch)are shown in Table 4.10, Table 4.11, and Table 4.12.

Table 4.10 The change in THD values for voltage and current for different rectifier and inverter gains, (amplitude is 1 for both rectifier and inverter, rectifier Fs is 50 kHz, inverter Fs is 25 kHz)

Rectifier Gain (G)	Inverter Gain (G)	Voltage (THD)%	Current (THD)%
1	1	0.2	0.2
1	0.5	0.2	0.2
1	0.2	0.2	0.2
1	0.1	0.2	0.2
0.5	1	0.2	0.2
0.2	1	0.2	0.2
0.1	1	0.2	0.2
0.5	0.5	0.2	0.2
0.2	0.2	0.2	0.2

Table 4.11 The change in THD values for voltage and current for different rectifier and inverter amplitudes, (gain is 1 for both rectifier and inverter, rectifier Fs is 50 kHz, inverter Fs is 25 kHz)

Rectifier Amplitude	Inverter Amplitude	Voltage (THD)%	Current (THD)%
0.5	1	0.2	0.2
1	1	0.2	0.2
2	1	0.4	0.4
3	1	0.4	0.4
1	0.5	0.2	0.2
1	2	0.1	0.1
1	3	0.08	0.1
1	5	0.08	0.1
0.5	0.5	0.2	0.2
2	2	0.3	0.3
3	3	0.3	0.3

Table 4.12 The change in THD values for voltage and current for different rectifier and inverter switching frequencies, (gain and amplitude of rectifier is 1 and 0.5, gain and amplitude of inverter is 5 and 1, rectifier Fs is 50 kHz, inverter Fs is 25 kHz)

Rectifier (f_s)	Inverter (f_s)	Voltage (THD)%	Current (THD)%
50	50	0.1	0.1
50	40	0.08	0.1
50	30	0.08	0.1
50	20	0.08	0.1
50	25	0.08	0.1
40	50	0.1	0.1
30	50	0.1	0.1
20	50	0.1	0.1
25	50	0.1	0.2

4.8 WECS Mathematical Model

In this section, the mathematical models of each component of the WECS are described in detail. This mathematical model presents for all parts of the WECS separately. The main equations are mentioned for each part separately. All the parts are then combined into a single system. The generated active and reactive power are transferred to the SMC and then to the grid. The mathematical models of the parts of the WESC are given as follows.

4.8.1 Wind Turbine Model

The kinetic energy stored in a wind turbine is represented by Equations (4.1) and (4.2) [44].

$$\mathrm{E_C} = \frac{1}{2} m v^2 \tag{4.1}$$

$$m = \rho v S \tag{4.2}$$

where$m$ is the air mass, $v$is the wind speed in m/s, $\rho$is theair density in kg/m^3, and $S$is the total surface area of the turbine blades in m^2. The wind power can be represented by the following Equation (4.3) [44][60].

$$P_w = E_c = \frac{1}{2} m v^2 = \frac{1}{2} \rho S v^3 \tag{4.3}$$

The wind turbine is used to convert wind energy into mechanical energy. Equation (4.4) represents the relationship between mechanical energy and wind energy to extract the power coefficient of the turbine [44].

$$C_p = \frac{P_m}{P_w};\ C_p < 1 \tag{4.4}$$

where$C_p$is the unitless power coefficient of the turbine, P_m is the mechanical power (W), and $P_w$is the captured wind power (W). The power coefficient of the turbine has a maximum limit, called as “Betz's limit”. Theoretically, the power coefficient is equal to 0.593, meaning that no energy is higher than 59.3% of the extracted from the turbine. The coefficient C_p is a function of pitch angle (β) and tip speed ratio (λ), expressed as follows [44][61].

$$P_m = C_p(\lambda, \beta) = \frac{\rho S}{2} v_{wind}^3 \tag{4.5}$$

$$T_m = \frac{P_m}{w} \tag{4.6}$$

Figure 4.21 includes the simulation model of the wind turbine, with the control mechanism used to obtain the mechanical power needed to rotate the generator. PMSG is used in the WECS. The input side of the wind turbine includes three main parameters.

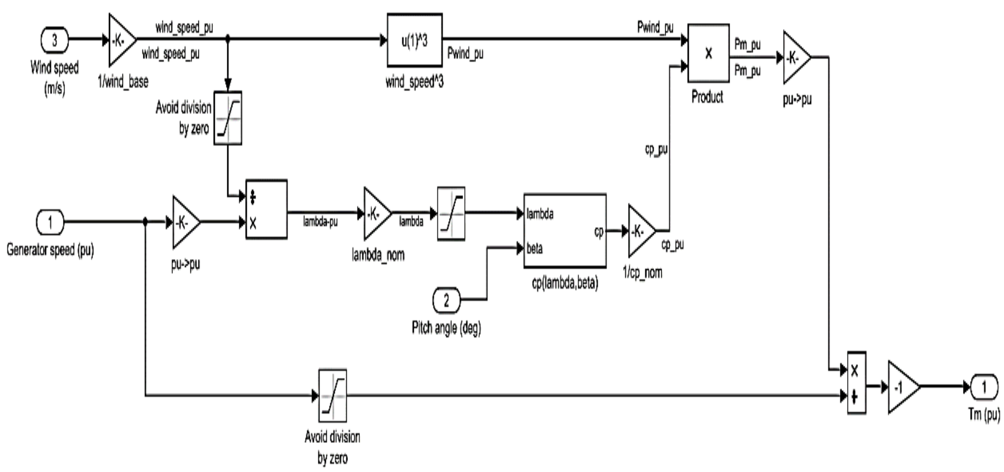

Figure 4.21 The simulation model of wind turbine

The wind speed rotates the turbine blades. There is a feedback loop from the generator which is connected after the turbine stage, and its usefulness is to control the speed of the generator by increasing or decreasing the rotational speed of the turbine. The pitch angle, through which the turbine blades are angled, so that they are always facing the wind in order to get the most benefit from the wind energy. Adjusting the angle of inclination of the blades also helps to control the speed of the generator. The output side of the wind turbine is to obtain the mechanical torque (Tm) needed eventually to rotate the generator shaft. The pu measurements are adopted for the whole system.

4.8.2 PMSG Model

Permanent magnets are used in PMSGs instead of field windings and field excitation circuit. This situation brings many advantages to PMSGs such as small size, high power density, high reliability, and robustness. Also, PMSG can be equipped without any gearbox in a WECS which reduces maintenance costs. The equivalent circuit of a PMSG is shown in Figure 4.22. This model is constructed in d-q synchronous reference frame [62][63]. Table 4.13 shows PMSG model parameters used in the simulation studies.

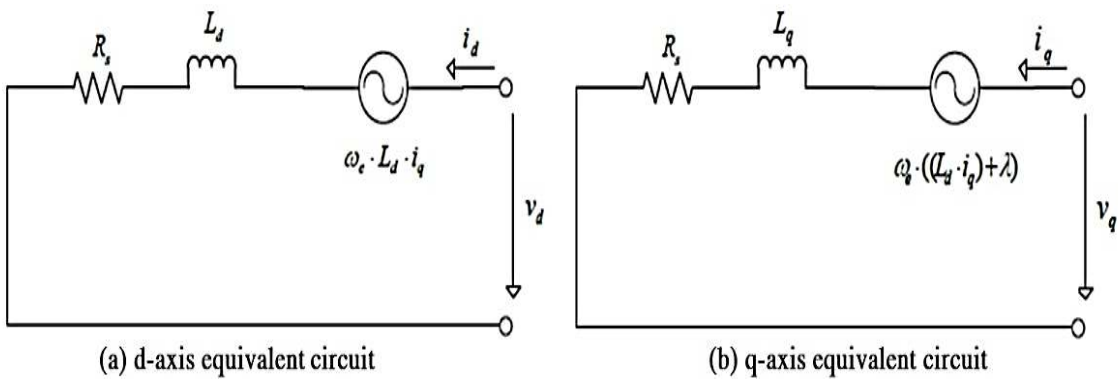

Figure 4.22 The equivalent circuit of PMSG in the d-q synchronous reference frame [64]

The voltage equations of a PMSG can be written as follows [64]

$$\frac{d}{dt} i_d = \frac{1}{L_d} v_d - \frac{R}{L_d} i_d + \frac{L_q}{L_d} p w_r i_q \quad (4.7)$$

$$\frac{d}{dt} i_q = \frac{1}{L_q} v_q - \frac{R}{L_q} i_q + \frac{L_q}{L_q} p w_r i_q - \frac{\lambda p w_r}{L_q} \quad (4.8)$$

The electromagnetic torque can be represented in Equation (4.9) [65].

$$T_e = 1.5\rho[\lambda i_q + (L_d - L_q)i_d i_q \quad (4.9)$$

where, L_d is the d–axis inductance, L_q is the q–axis inductance, R is the resistance of the stator windings, i_d is the d–axis current, i_q is the q–axis current, v_d is the d–axis voltage, v_q is the q–axis voltage, w_r is the angular velocity of the rotor, λ is the amplitude of induced flux, p is the number of pole pairs. The dynamic equations are represented by Equations (4.10) and (4.11) [66],

$$\frac{d}{dt} w_r = \frac{1}{J}(T_e - F w_r - T_m) \quad (4.10)$$

$$\frac{d}{dt}\theta = w_r \quad (4.11)$$

where, J is the inertia of the rotor in ($kg.m^2$), F is the friction coefficient of the rotor in (N.m.sec), and θ is the rotor angular position in (rad/sec).

Table 4.13 PMSG simulation model parameters

Parameter	**Value**
Power rating	1.5 MW
Stator phase resistance	0.006 Ω
Armature inductance	0.000395 H
Flux linkage	1.51 Wb-turns
Number of polepairs	48

4.8.3 Drive Train Model

The mechanical drive system used in a WECS delivers mechanical power to the shaft of the generator. It differs from the gearbox used in Doubly Feed Induction Generator (DFIG). The drive train system helps to reduce the size of the PMSG.WECS that use drive trains do not need a large PMSG generator to compensate for the differences in speed, thus making the system lighter and less expensive to manufacture. The wind turbines can be classified according to the used drive train configuration and the speed required for the turbines. This classification is shown in Figure 4.23. Table 3.4 shows the quantity of what the wind turbine requires from permanent magnet (PM) for manufacturing and compares the quantity used with different types of generators according to the capacity of each one. PM mainly contributes to increased manufacturing costs due to its manufacture from rare earth elements [62][67]. Figure 4.24 shows the drive train model used in this work. The mathematical model of this drive train is expressed as follows,

$$2H_t \frac{dw_t}{dt} = T_m - T_s \tag{4.12}$$

$$\frac{1}{w_{ebs}} \frac{d\theta_{sta}}{dt} = W_t - W_r \tag{4.13}$$

$$T_s = K_{ss}\theta_{sta} + D_t \frac{d\theta_{sta}}{dt} \tag{4.14}$$

where, H_t is the inertia constant of the turbine, θ_{sta} is the shaft twist angle in rad /sec, W_t is the angular speed of the wind turbine rad/sec, W_r is the rotor speed of the generator in rpm, w_{ebs} is the electrical base speed in pu, T_s is the shaft torque in rad/N-m, K_{ss} is the shaft stiffness in rad.N/m, and D_t is the damping coefficient in lbf s/inch.

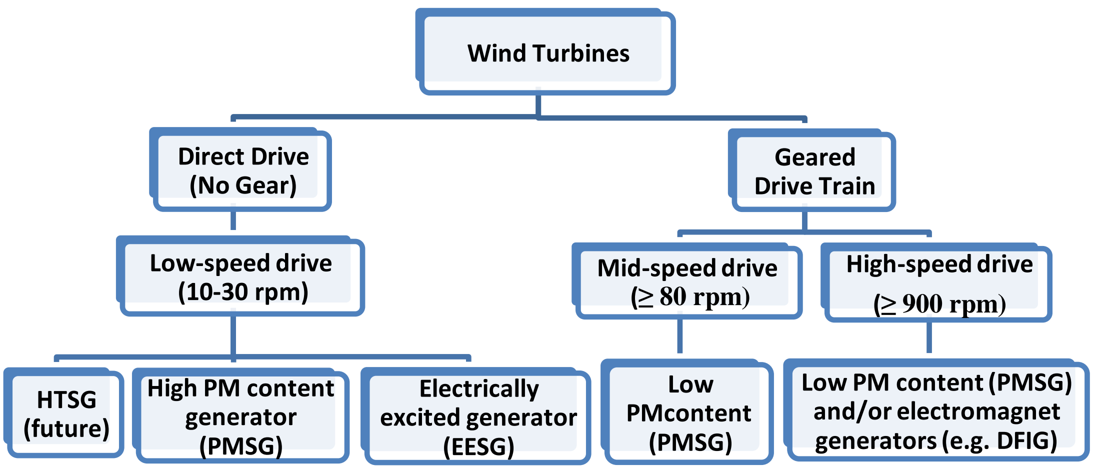

Figure 4.23 Types of turbines according to drive train configuration and the speed limit [68]

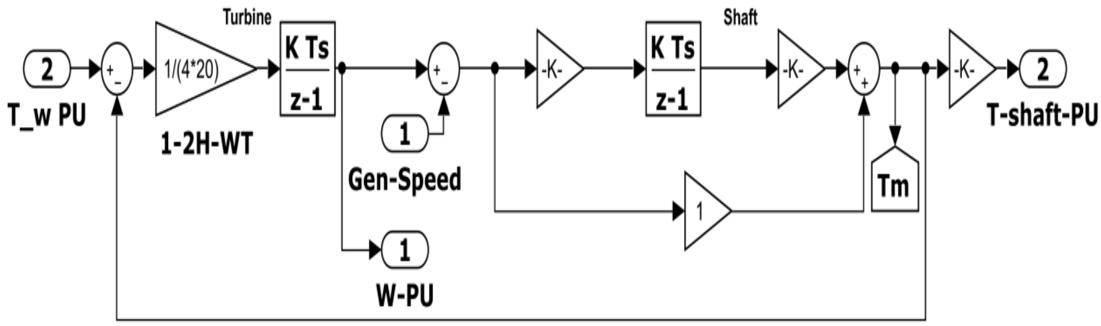

Figure 4.24 Simulation model of the drive train

Table 4.14 The quantity of permanent magnetic in each type of generator.**a** Typical permanent magnet amount: high =650 kg/MW; medium =160 kg/MW; low =80 kg/MW, **b**EESG– electrically excited synchronous generator, **c** Over time, Enercon has upgraded the capacity of its generator [69][70]

Technology	Permanent magnet amount[a]	Generator type and capacity	Manufacturer
Low-speed/direct drive	High	PMSG 6 MW	Siemens Wind Power
Mid-speed/geared	Medium	PMSG 8 MW	Vestas (MHIVestas)
Low-speed/direct drive	None	EESG[b] 7.58 MW	Enercon[c]
Low-speed/direct drive	High	PMSG 6 MW	Alstom
High-speed/geared	None	DFIG 6.2 MW	Senvion
Mid-speed/geared	Medium	PMSG 5 MW	Advent

4.9 The Complete Simulation Model of PMSG based WECS

Figure 4.25 represents the final complete simulation model of the PMSG based WECS proposed in this study. The system is divided into many stages.The first stage is the generation stage. This stage includes the wind turbine, drive train, PMSG, in addition, the control systems that are used to control the generation stage to obtain the required active and reactive power. A constant wind speed of 9m/s is used to rotate the turbine. The pitch angle control system is used, which constantly adjusts the angle of inclination of the turbine blades so that they are facing the wind to achieve the maximum benefit from the wind energy.The mechanical torque produced by the turbine is transmitted to the drive train. The operational controller block determines the maximum speed at which the generator is rotated by controlling the rotation of the drive train. When the maximum speed is exceeded more than 9m/s, the operational controller turns off the generator to prevent it from damage. Finally, the mechanical torque is transmitted to the PMSG. The generator generates a rated power of 1.5 MW. This power is transferred to the next stage of the system.The second stage is the converter stage. A three-phase SMC is used. The SMC consists of two main stages, rectifier stage and inverter stage. Each stage contains bidirectional switches. These switches consist of semiconductors, IGBT, and diode. Each stage of the SMC is controlled separately, in order to obtain the maximum value of the AC output voltage. The energy from the generation stage is injected into the first stage of the SMC into the rectifier stage. The rectifier stage converts AC input voltage to DC output voltage. Since the SMC does not contain energy storage elements such as a conductor or capacitor, will be dealt with a fictitious DC link between the rectifier stage and inverter stage. DC output voltage from rectifier stage is the input to inverter stage. The inverter stage converts a DC voltage to AC output voltage. An open-loop control system is used to control the rectifier stage to generate PWM signals that control the switches from S1 to S9. A closed-loop control system is used to control the inverter stage to generate PWM signals that control the switches from S10 to S15. The closed-loop control system depends on the PID or FFOPID to calculate the error and change in the error. The AC output voltage from the converter stage is transferred to the next stage. The third stage is the filter stage. The filter stage eliminates or reduces the harmonics present in the waveforms of the SMC. The electrical energy is transferred to the next stage. The fourth and final stage is the electrical grid stage. The electrical grid consists of a Y-Y connected transformer designed with a frequency of 50 Hz, an apparent power of 2.5 MVA, a voltage for the primary winding is 0.6 kV rms phase to phase, a voltage for the secondary winding of 20 kV rms phase to phase. The network also contains power transmission lines and loads. The transmission line and load parameters are shown in Figure 4.25.

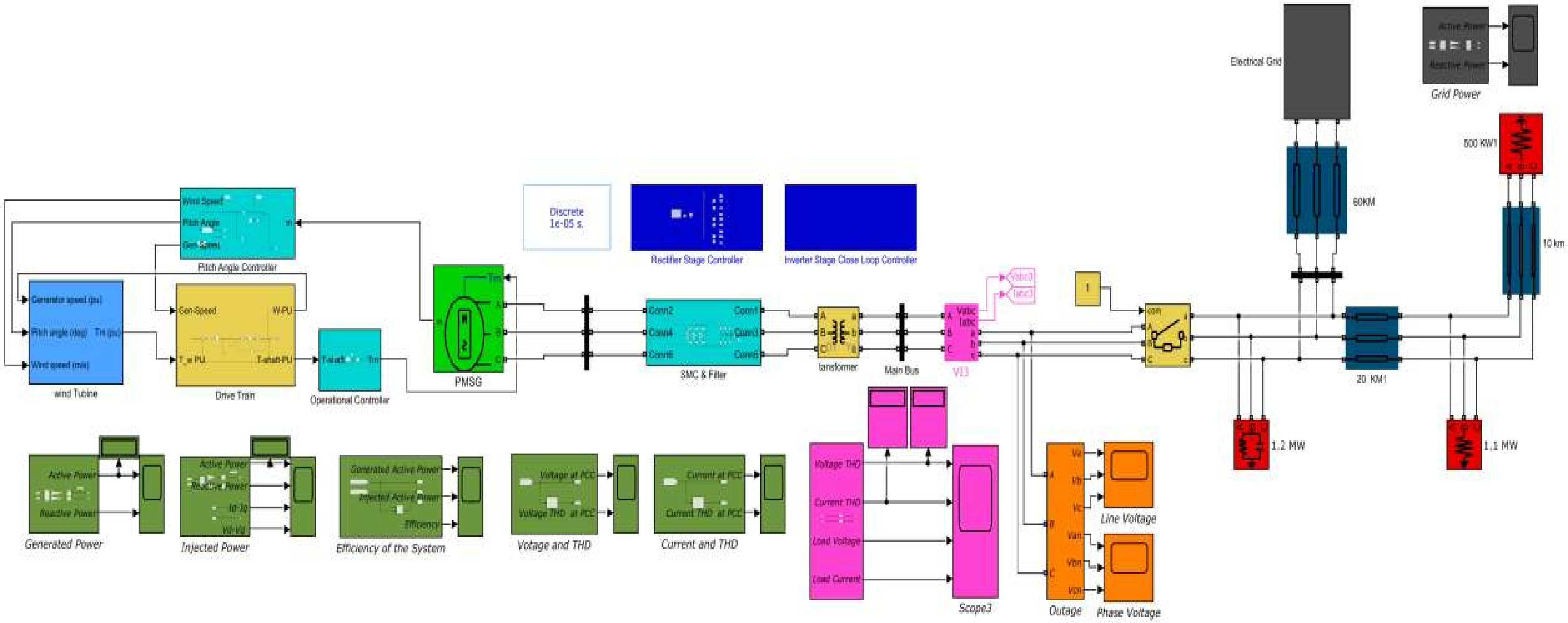

Figure 4.25 The simulation model of PMSG based WECS

4.10 The Control System Model

The conceptual block diagram of the designed control system for the inverter stage of the SMC is shown in Figure 4.26. As seen, it is based on the transformation from ABC to dq0 reference frame and vice versa. In this control approach, FFOPID or PID controllers can be selected for comparison of their performances. The simulation model of ABC to dq0 transformation is given in Figure 4.27. The closed loop simulation model of the inverter stage control is shown in Figure 4.28.

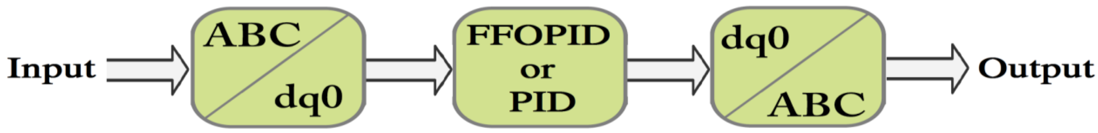

Figure 4.26 The conceptual block diagram of the closed loop control

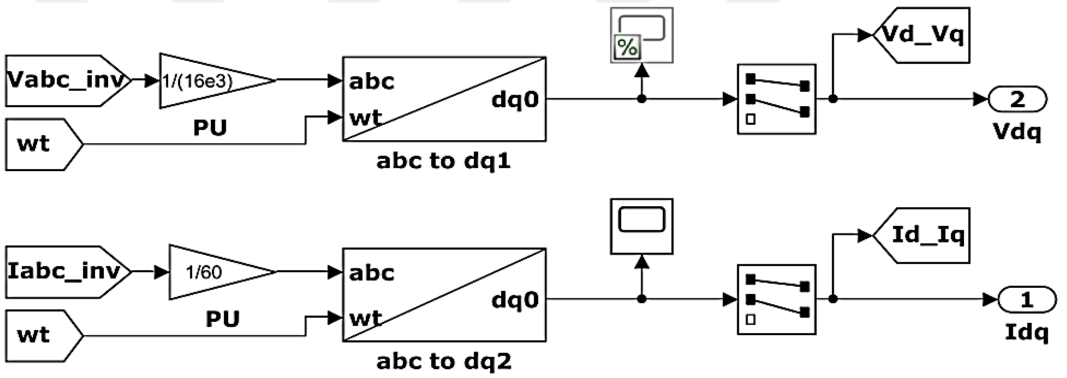

Figure 4.27 The simulation model of ABC to dq0 transformation

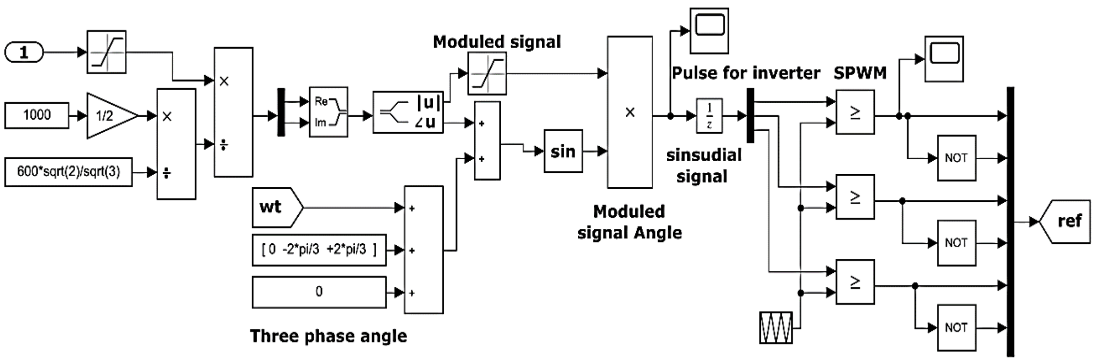

Figure 4.28 The closed loop simulation model of the inverter stage control

4.10.1 The Simulation Model of The Inverter Stage Controller Based on PID Control Scheme

Figure 4.29 depicts the simulation model of the inverter stage controller which is based on PID control scheme. The objective of this controller is to produce control signals for the power semiconductor switches in the inverter stage of the SMC from the reference values of I_{d-ref}, I_{q-ref}. The input of this controller has three signals. The first one is the grid voltage (V_{ABC}). This signal is the combination of the three-phase line-to-neutral voltages obtained from the grid. This signal is used as in input of the PLL to produce reference signals such as, frequency and wt. The latter one is used for synchronization of the control scheme with the grid. The second and third signals that enter to the controller areI_{d-ref}, I_{q-ref} values. The I_{d-ref} value is set to one pu so that the active power injected into the network from the WECS is set to 100% of the produced power from the wind. The value of the I_{q-ref} is set to zero pu so that the reactive power injected into the grid from the WECS is set to zero (unity power factor operation). The PID controller generates the control signal based on the error signal at its input [71]. Finally, the control signals for the inverter stage are obtained at the output of the control scheme. Then, the active and reactive power are injected into the grid at their predefined values using the above-mentioned controller mechanism.

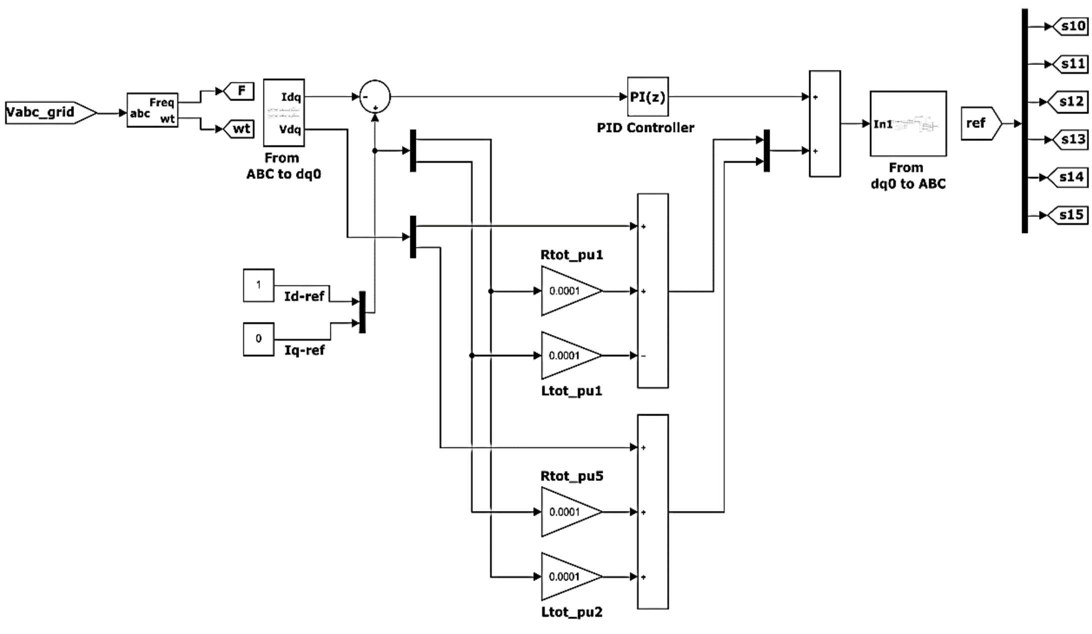

Figure 4.29 The simulation model of inverter stage controller based on PID control scheme

4.10.2 Fractional-Order PID Controller Model

Continuing study and research in the field of controllers has produced modern controllers, including the FO, which is better than the classic PID controller in terms of performance and durability [72][73]. The FO calculus applications for dynamic systems have started in the year 1960 [74]. Since then, the research on FO control has extended to various areas of engineering. The fractional-order PID controller is a sum of fractional operators along with controller gains. The mathematics dealing with FO is integration branches and calculus of the real and complex order. Calculating FO relates to fractional dimension infinite memory and chaotic behavior. FO can apply in electronics, control theory, and many other fields [55][56].FO mathematics is necessary to describe and model real-time more accurately than using traditional integers. The FO differentiator can be represented as a continuous differential integral operator as in Equation (4.17) [75]-[77],

$$aD_t^{\gamma} = \begin{cases} \frac{d^{\gamma}}{dt^{\gamma}} \Re(\gamma) > & 0 \\ 1 & \Re(\gamma) = 0 \\ \int_a^t (d\tau)^{-\gamma} & \Re(\gamma) < 0 \end{cases} \quad (4.17)$$

where, γ is the order of the differ integration, and a is constant related to initial conditions. Several standard definitions used in the field of FO calculus are Caputo (e.g., in numerical integration and physics), Grunwald-Letnikov (e.g., communications and control), and Riemann-Liouville (e.g., in calculus). The Riemann-Liouville and Caputo definitions are expressed in Equation (4.18),

$$aD_t^{\gamma} f\,(t) = \frac{1}{\Gamma(n-1)} \frac{d^n}{dt^n} \int_a^t \frac{f(\tau)}{f(t-\tau)^{\gamma-n+1}} d\tau \quad (4.18)$$

where, $\Gamma(\gamma)$, $(n-1 < \gamma < n)$ is the normal gamma function represented as,

$$\Gamma(\gamma) = \int_0^{\infty} e^{-u} u^{\gamma-1} du, \; \Re(\gamma) > 0 \quad (4.19)$$

The Grunwald-Letnikov definitions used in this thesis are represented as,

$$ {}_aD_{\gamma}^{t} f(t) = \lim_{h \to 0} h^{-\gamma} \sum_{j=0}^{[(t-a)/h]} (-1)^{j} \binom{\gamma}{j} f(t - jh) \quad (4.20) $$

where, $[(t-a)/h]$ are the limits of the operator. The gamma function generalizes the factorial operator. It is works on evaluating the binomial coefficient, given as,

$$ \binom{\gamma}{j} = \frac{\gamma!}{j!(\gamma-j)!} = \frac{\Gamma(\gamma+j)}{\Gamma(\gamma+1)\,\Gamma(\gamma-j+1)} \quad (4.21) $$

The beneficial equation to get the numerical solution of a fractional differential equation is Equation (4.20) [78]. The FOPID controller transfer function is given as,

$$ G_c(s) = \frac{I_{abc}(s)}{e\,(s)} = K_P + K_I s^{-\lambda} + K_D s^{\mu} \quad (4.22) $$

where, $G_c(s)$is the controller transfer function, $e(s)$is the error, $I_{abc}(s)$ is the output, K_P, K_I, K_D are respectively the gains for proportional, integral, and derivative terms. The term$\lambda$is defined as the fractional component of the integral part, and μ is the fractional component of derivative part. The FOPID controller time-domain representation is given as follows,

$$ I_{abc}(t) = K_P e(t) + K_I D^{-\lambda} e(t) + K_D D^{\mu} e(t) \quad (4.23) $$

It is evident that, in the FOPID controller, apart from the usual three parameters K_P, K_I, and $K_D$the parameters of integral order λ and derivative-order μ should be considered. Hence, the FOPID controller design procedure involves solving five nonlinear equations with five unknowns K_P, K_I, K_D, λ, and μ related to the system. On the other hand, it has five complex nonlinear equations, and when we notice this complexity, we see it is due to the presence of fractional order. The simulation environment can be considered as the appropriate tool for designing this controller with minimum error rate. The controller design for the suggested system is completed by using the FOMCON toolbox with Oustaloup's analytical approximation technique described in [79][80].

4.10.3 Fuzzy Fractional-Order PID Controller Model

In this study, fuzzy logic theory is used to dynamically adjust the gains (K_P, K_I, K_D) of the PID controller. The real-time adjustments are given as follows,

$$\left\{ \begin{array}{c} K_P = K_P + \Delta K_P \\ K_I = K_I + \Delta K_I \\ K_D = K_D + \Delta K_D \end{array} \right\} \tag{4.24}$$

where, K_P, K_I, and K_D are the initial gains of the PID controller, $\Delta K_P, \Delta K_I$, and $\Delta K_D$are the dynamic scaling factors computed by fuzzy logic theory. In the design of fuzzy part, Mamdani-type fuzzy inference system is used with triangle membership functions for inputs and Gaussian membership functions for output. Note that two membership functions are used for the inputs, whereas three membership functions are selected for the outputs. The FFOPID controller parameters used in the design are listed in Table 4.15.

Table 4.15 FFOPID controller parameters

K_P	K_I	K_D	γ	μ
1.2	0.25	0.01	0.3	0.3

Figure 4.30 represents the simulation model of the FFOPID controller used for the inverter stage of the SMC. The objective of this controller is to obtain control signals for the power semiconductor switches of the inverter stage of the SMC. The operation style of the FFOPID controller is the same as that of the PID control scheme which is previously mentioned. However, The FFOPID controller works to adjust the error and change of error by adopting the FO system in which a fuzzy interference system is added. FFOPID controller is placed for the two components such as $d - q$ separately.Finally, we get a PWM signal that controls the power semiconductor switches of the inverter stage of the SMC. The simulation studies show that the active and reactive power are injected into the grid in a faster time response compared to the classical PID controller. The details of this comparison are mentioned later in more detail. The membership functions used in the fuzzy interference system are shown in Figure 4.31. The membership functions are designed with linguistic variables. For input, NB is negative big, NM is negative

medium, NS is negative small, Z is zero, PS is positive small, PM is positive medium, and PB is positive big. For output small and big definitions are utilized. The rule base is the pivotal part of the fuzzy logic control design which links the input and output linguistic variables. Mudi and Pal in 1999 had recommended the methods for framing rule base using conjectural logic [81]. Table 4.16, Table 4.17, and Table 4.18 respectively represents the output rule $\Delta K_P, \Delta K_I$, and ΔK_D. The surface view relationships between input and output are shown in Figure 4.32. The surface view shows how the scaling factor could vary based on input and change-in-error magnitude. From the surface view, it is observed that input and output have a nonlinear relationship, in particular for the proportional and derivative scaling factors. The proportional, integral, and derivative scaling values are more for the larger amplitude of error and change-in-error. Also, these values have gradually reduced for the minor error and change-in-error values. To determine the crisp output, the center of gravity defuzzification is used [56][82][83].

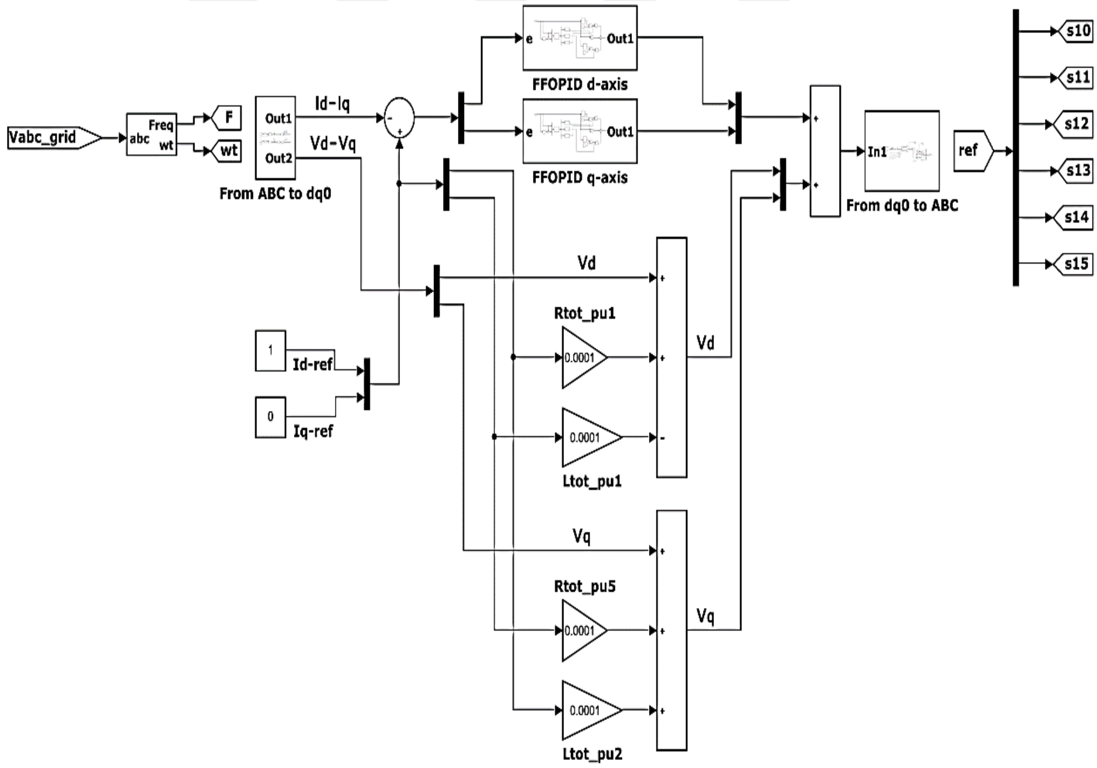

Figure 4.30 The simulation model of the FFOPID controller

Table 4.16 Fuzzy linguistic rules for $\Delta K_P - e$ pair

d, q		Δe						
ΔK_P		NB	NM	NS	Z	PS	PM	PB
e	NB	Big	Big	Big	Big	Big	Big	Big
	NM	Small	Big	Big	Big	Big	Big	Big
	NS	Small	Small	Big	Big	Big	Small	Small
	Z	Small	Small	Small	Big	Small	Small	Small
	PS	Small	Small	Big	Big	Big	Small	Small
	PM	Small	Big	Big	Big	Big	Big	Small
	PB	Big	Big	Big	Big	Big	Big	Big

Table 4.17 Fuzzy linguistic rule and $\Delta K_I - \Delta$epair

d, q		Δe						
ΔK_I		NB	NM	NS	Z	PS	PM	PB
e	NB	Small	Small	Small	Small	Small	Small	Small
	NM	Big	Big	Small	Small	Small	Big	Big
	NS	Big	Big	Big	Small	Big	Big	Big
	Z	Big	Big	Big	Big	Big	Big	Big
	PS	Big	Big	Big	Small	Big	Big	Big
	PM	Big	Big	Small	Small	Small	Big	Big
	PB	Small	Small	Small	Small	Small	Small	Small

Table 4.18 Fuzzy linguistic rule and $\Delta K_D - \Delta e$ pair

d, q		Δe						
	ΔK_D	NB	NM	NS	Z	PS	PM	PB
e	NB	Small	Small	Small	Small	Small	Small	Small
	NM	Big	Big	Small	Small	Small	Big	Big
	NS	Big	Big	Big	Small	Big	Big	Big
	Z	Big	Big	Big	Big	Big	Big	Big
	PS	Big	Big	Big	Small	Big	Big	Big
	PM	Big	Big	Small	Small	Small	Big	Big
	PB	Small	Small	Small	Small	Small	Small	Small

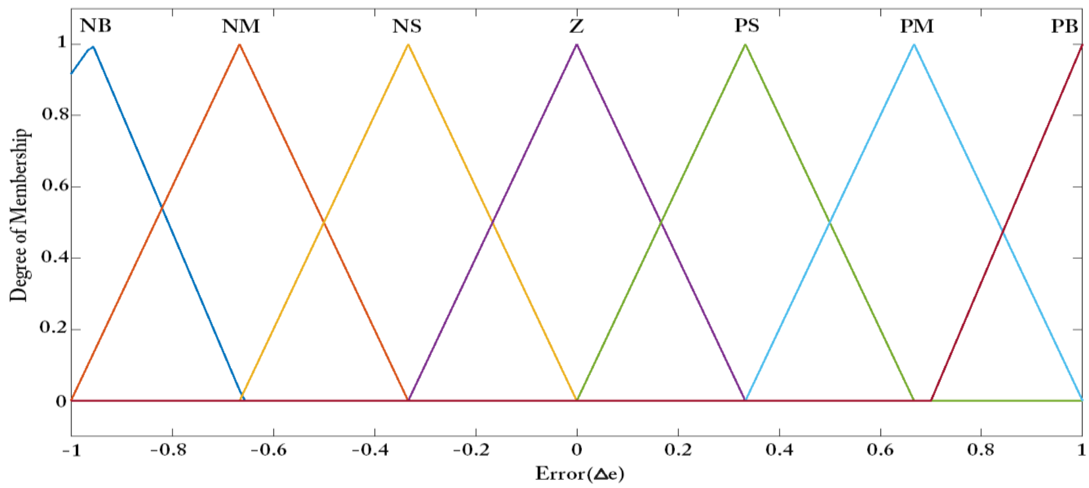

Figure 4.31 Input membership functions for error

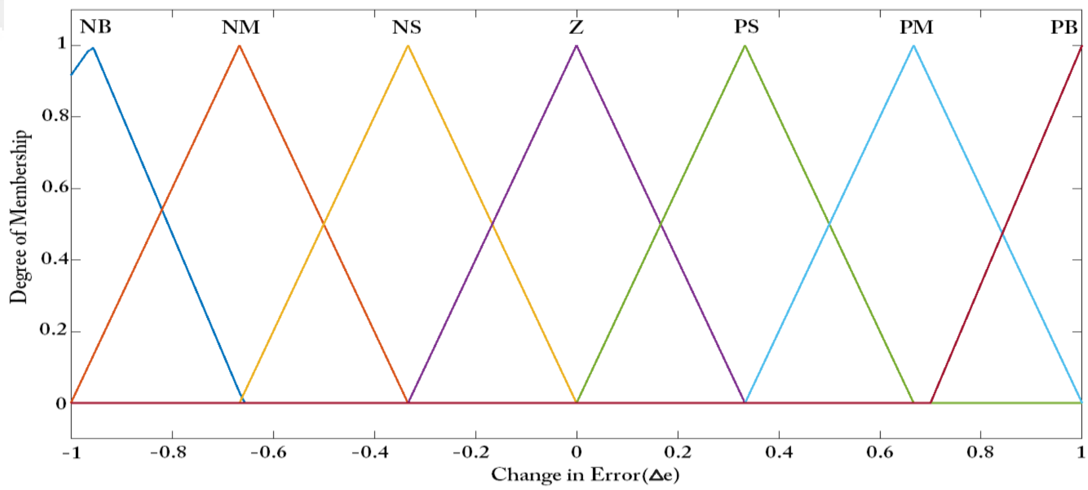

Figure 4.32 Input membership functions for change-in-error

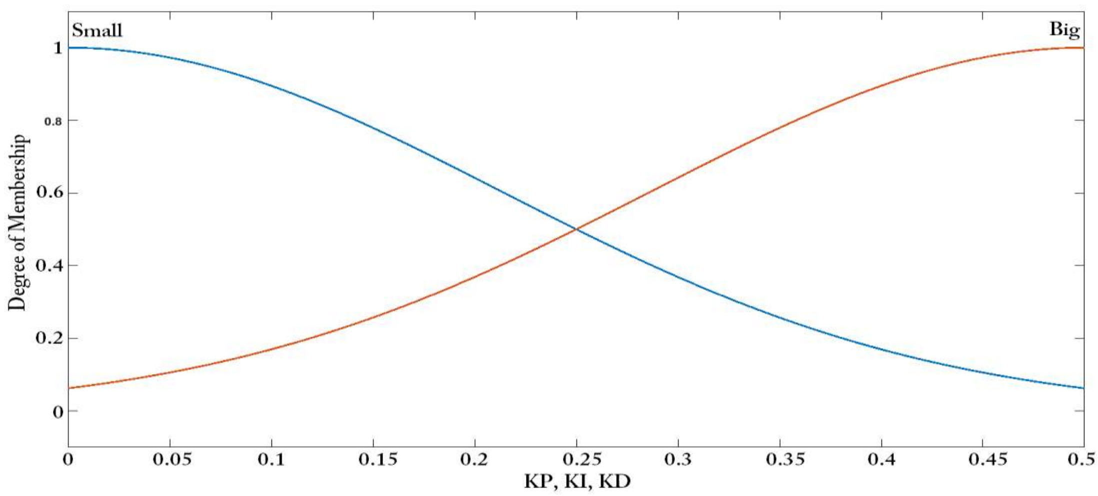

Figure 4.33 Output membership functions for $\Delta K_P, \Delta K_I, \Delta K_D$

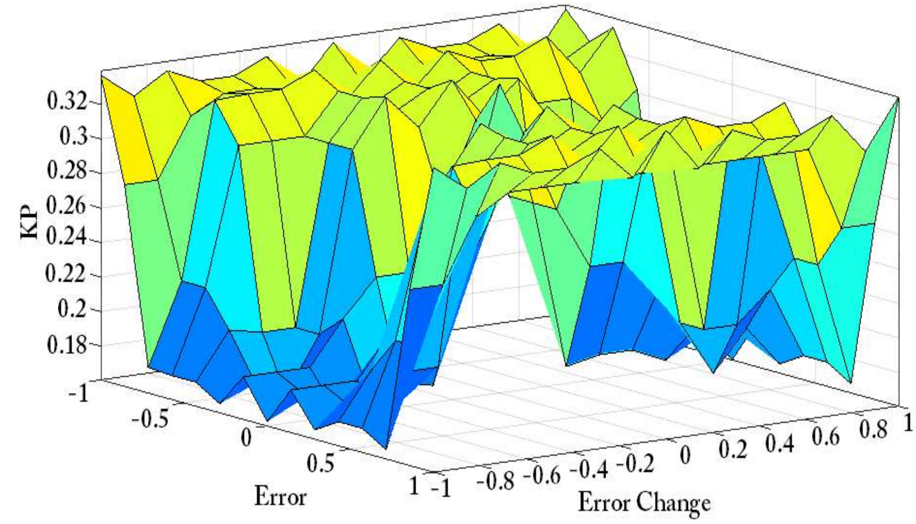

(a)

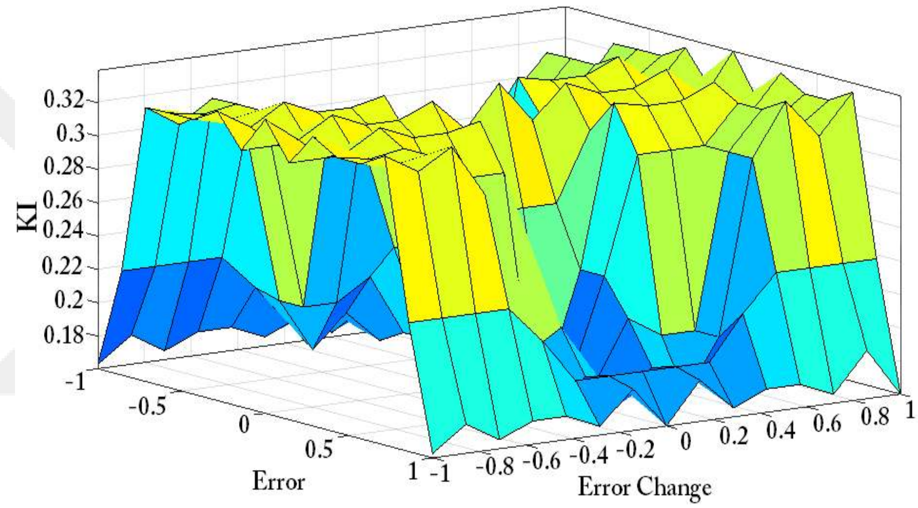

(b)

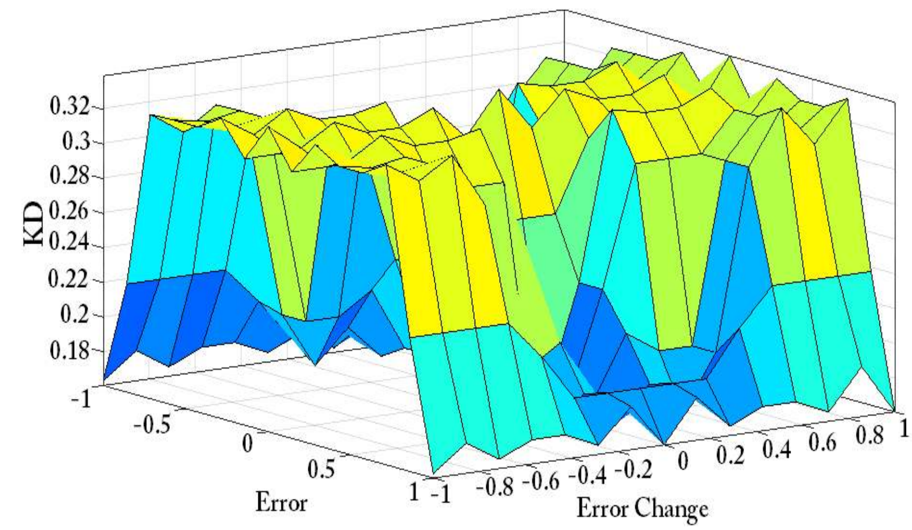

(c)

Figure 4.34 The surface view of change of (a) ΔK_P, (b)ΔK_I, (c)ΔK_D with respect to error and change-in-error

4.11 The Simulation Results of PMSG based WECS Connected to Grid

4.11.1 The Simulation Results with PID Controller

In this study, WECS is designed to generate a rated power of 1.5 MW. The generated power appears at the input of the SMC (rectifier stage). By using the control system of the SMC, this power is transferred to the inverter stage of the SMC without using any storage element at the DC link. The inverter stage is operated with a fictitious DC power at its input to produce controllable AC voltage at its output. This AC power is then injected to the electrical grid through LCL filter and the coupling transformer. The control system used here is the PID controller. Figure 4.35 respectively represents the generated active and reactive power by the PMSG.

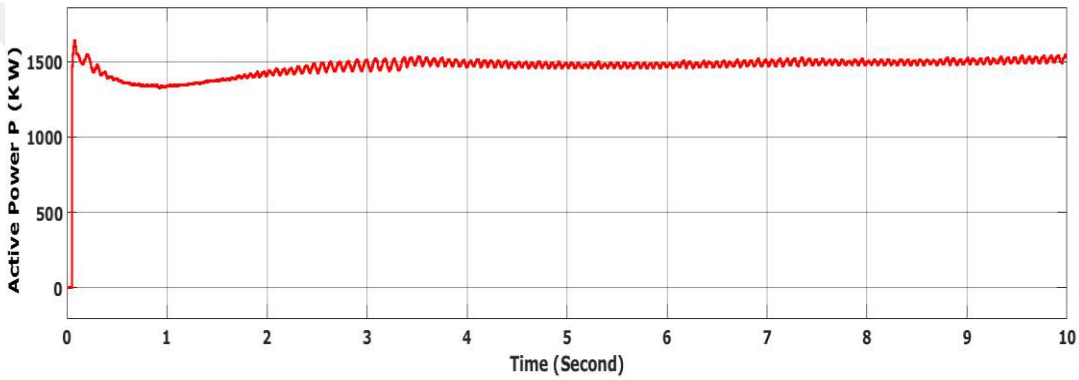

(a)

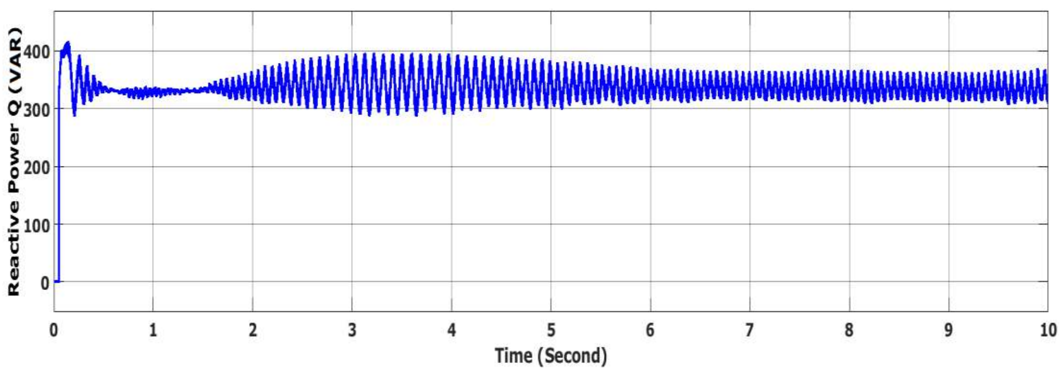

(b)

Figure 4.35 Generated power: (a) active power; (b) reactive power

The injected powers by the WECS into the electrical grid are shown in Figure 4.36. The reactive power injection must be zero or close to zero according to the previously described control conditions of the system. This is the condition necessary to have maximum power transferred without any impedance mismatch. When the reactive power is zero, this means that active power becomes equal to the apparent power. This means that the PF becomes unity. This also means that the system power rating is used as much as possible to inject the maximum possible amount of active power from the WECS into the grid. Figure 4.37 represents the grid side active and reactive power injections. From Figure 4.37, the following comments can be made. We also note that the stability of the grid is ensured when checking the simulation results. From Figure 4.37 (a), we notice that the value of the active power is about 1.4 MW. From Figure 4.37 (b), we notice that the value of the reactive power is about -300 VAR. The grid supplies this amount of reactive power to the loads connected to the grid. Since different power factor loads are available in the system.

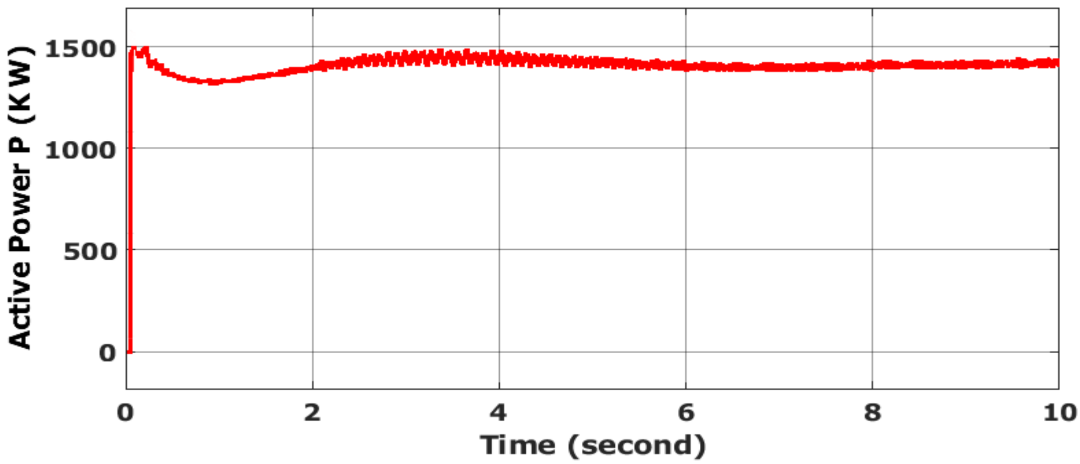

(a)

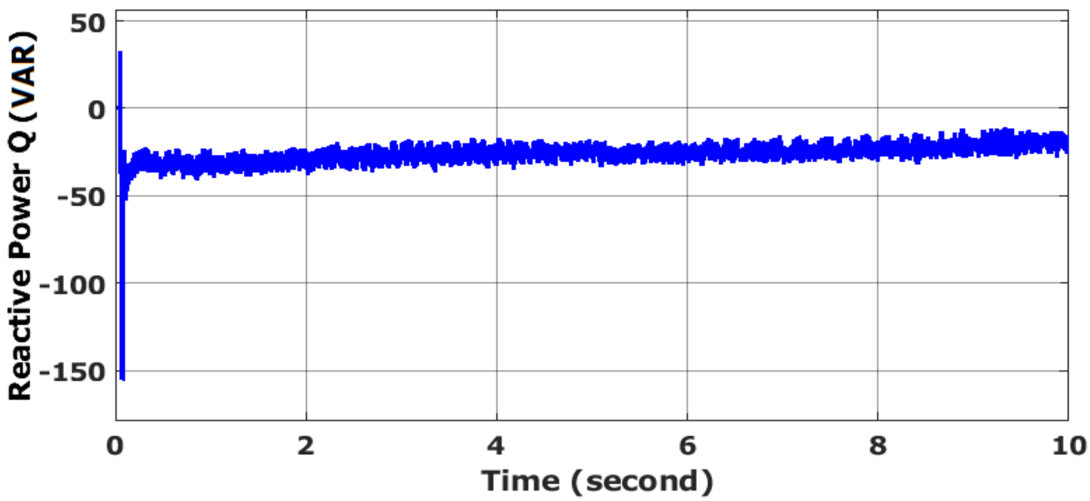

(b)

Figure 4.36 The injected powers by the WECS into the electrical grid: (a) active power, (b) reactive power

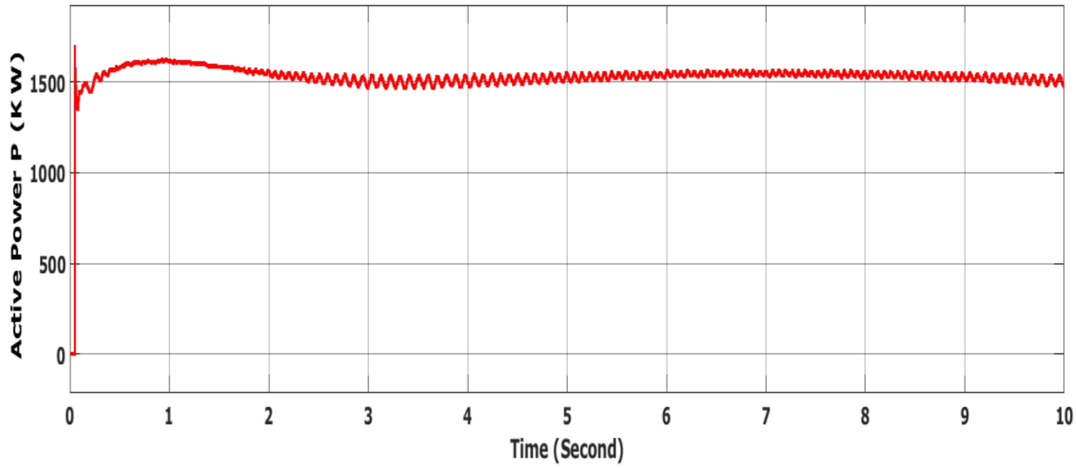

(a)

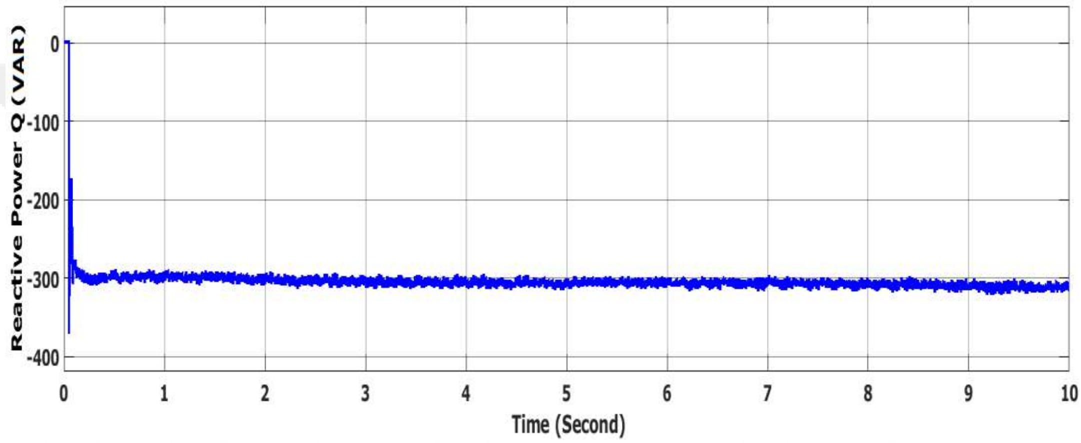

(b)

Figure 4.37 The grid side power injections: (a) active power, (b) reactive power

Figure 4.38 represents the dynamic change of the system efficiency to be about 93% when the PID controller is used.

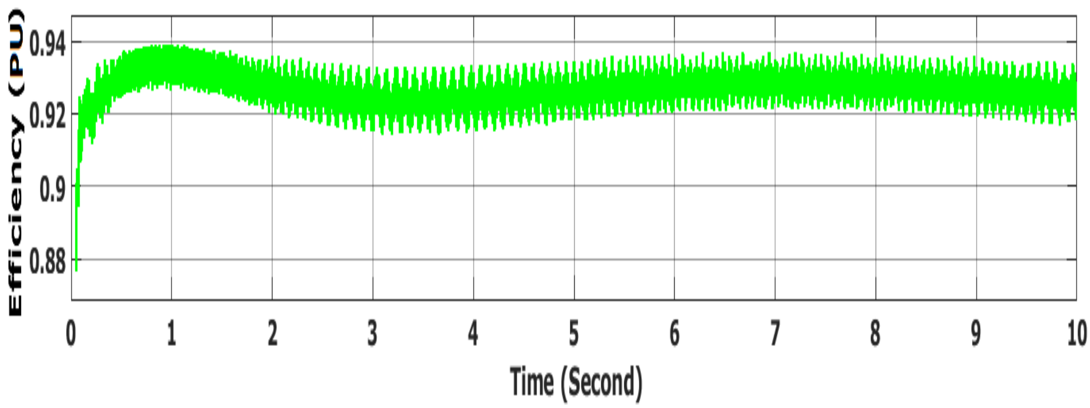

Figure 4.38 System efficiency when PID controller is activated

4.11.2 The Simulation Results with FFOPID Controller

Figure 4.39 (a) and (b) respectively represents the generated active and reactive power from the WECS into the grid. From Figure 4.39, the following comments can be made. Figure 4.39 (a) represents the generated active power which is very close to 1.5 MW. This value is the value on which the WECS was designed. From the respective waveform, we note that the response time is fast due to the use of the FFOPID controller. This response is faster than the response obtained when the PID controller is used, as shown in Figure 4.35 (a). Figure 4.39 (b) represents the generated reactive power of the WECS into the grid. From Figure 4.39, the following comments can be made. The value of the reactive power is 300 VAR. The FFOPID controller succeeded in reducing the value of the reactive power after it was equal to 370 VAR when using the PID controller. In terms of response time, it is faster when compared with the waveform generated using the PID controller as shown in Figure 4.35 (b).

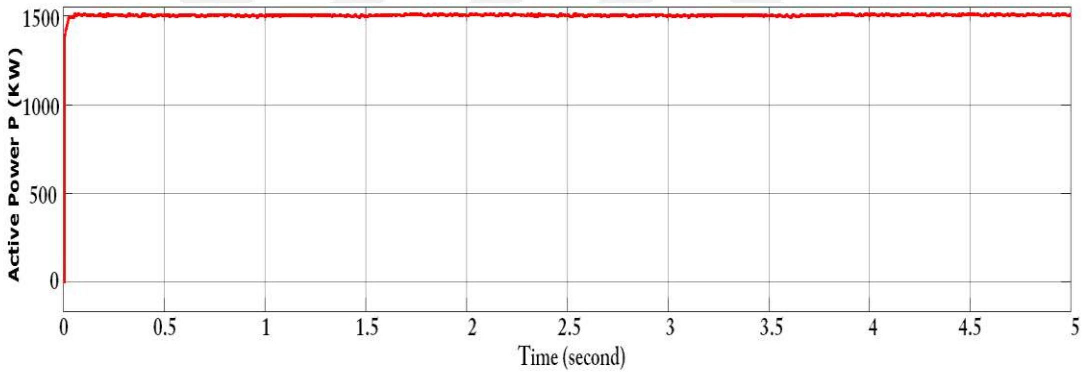

(a)

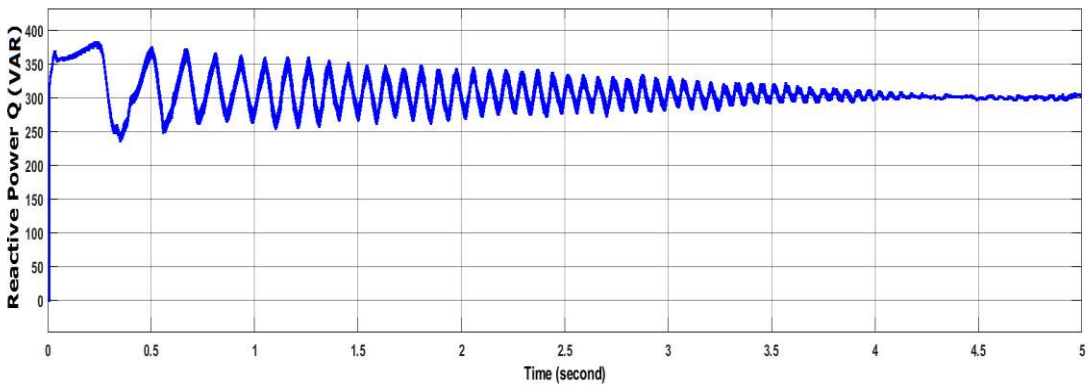

(b)

Figure 4.39 Generated power: (a) active power; (b) reactive power

Figure 4.40 (a) and (b) respectively represents the injected active and reactive power into the grid using the FFOPID controller. From Figure 4.40, the following comments can be made. Figure 4.40 (a) represents the injected active power which is very close to 1.5 MW. This is the value on which the WECS was designed. From the waveform, we note that the response time is fast due to the use of the FFOPID controller. This response is faster when compared to the waveform generated using the PID as shown in Figure 4.36 (a). Also, the value of the injected power is 1.4MW by using the PID controller. This proves the superiority of FFOPID control scheme. Figure 4.40 (b) represents the injected reactive power into the electrical grid. From this figure, the following comments can be made. The value of the reactive power is 0 VAR. The FFOPID controller succeeded in making the value of the reactive power stable after it was equal to -25 VAR when using the PID controller. In terms of response time, it is faster when compared with the waveform generated using the PID controller shown in Figure 4.36 (b).

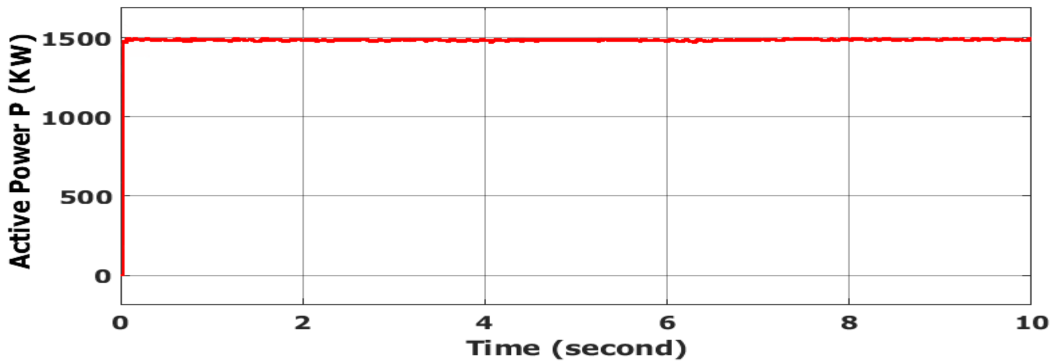

(a)

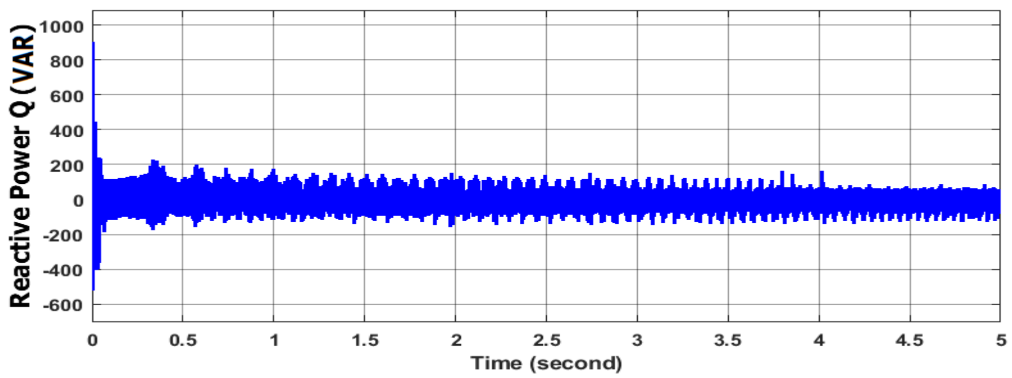

(b)

Figure 4.40 The injected powers by the WECS into the electrical grid: (a) active power, (b) reactive power

Figure 4.41 (a) and (b) respectively represent the grid active and reactive power. From Figure 4.41, the following comments can be made. Figure 4.41 (a) represents the grid active power and has a value of 1.75 MW. From the simulated waveform, we note that the response time is fast due to the use of the FFOPID controller, which is faster when compared to the waveform generated using the PID as shown in Figure 4.37 (a). Figure 4.41 (b) represents the grid reactive power. From this figure, the following comments can be made. The value of the reactive power is -300 VAR. Also, in terms of response time, it is faster when compared with the waveform generated using the PID controller shown in Figure 4.37 (b). Figure 4.42 represents the efficiency of the system. It is measured as about 94% after 5 seconds.

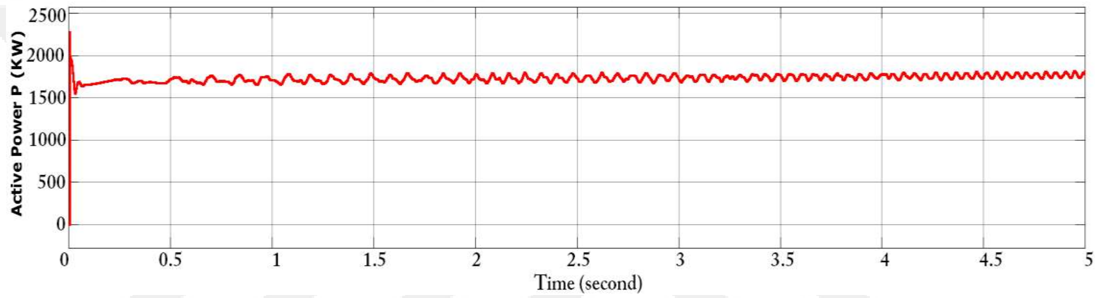

(a)

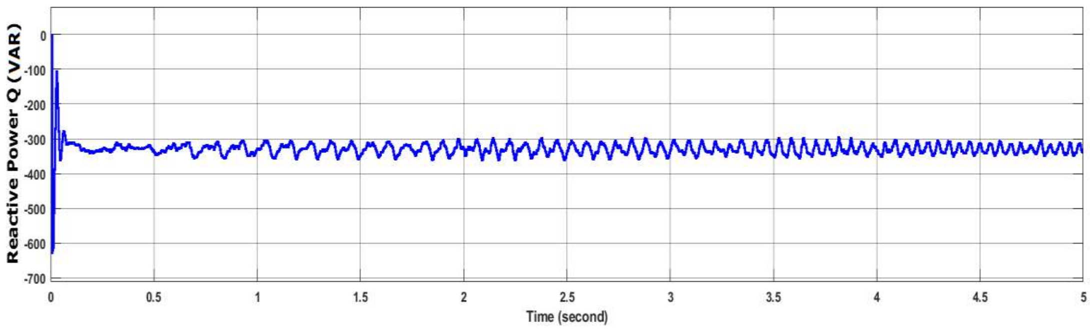

(b)

Figure 4.41 Grid power: (a) active power; (b) reactive power

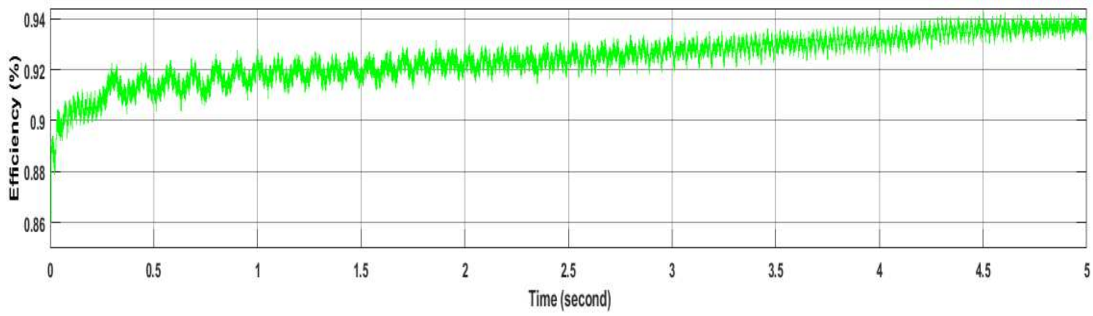

Figure 4.42 Efficiency of the system

4.11.3 The Comparison Study between PID and FFOPID Controller

In this section the dynamic performances of PID and FFOPID controllers are compared and evaluated. The wind speed is adjusted to 9m/s. Unit step changes are applied to both $I_{d-ref}$and I_{q-ref}at different times. Figure 4.43 shows a comparison between PID and FFOPID controllers when $I_{d-ref}$is constant and I_{q-ref} is altered. On the other hand, Figure 4.44 shows a comparison between PID and FFOPID controllers when $I_{q-ref}$is constant and $I_{d-ref}$is altered. The system that uses the classical PID controller takes a long time to reach the desired output and an acceptable value of the overshot until the steady-state is reached. However, when using the FFOPID, the system's response takes less time to reach the desired output when compared with the classical PID control. There is no value to be mentioned for overshoot, and access to the steady-state is much faster when FFOPID controller is utilized. All of these observations clearly make the FFOPID better than PID controller. Due to applications of the fuzzy logic theory and FO calculus, FFOPID controller is able to dynamically modify the controller gains in each sampling time, yielding better dynamic response can be obtained. Table. 4.19, Table. 4.20clarifies a qualitative comparison between PID and FFOPID controllers in terms of rise time, overshoot, settling time, and steady-state time. The numerical values clearly show the superiority of the FFOPID over PID controller.

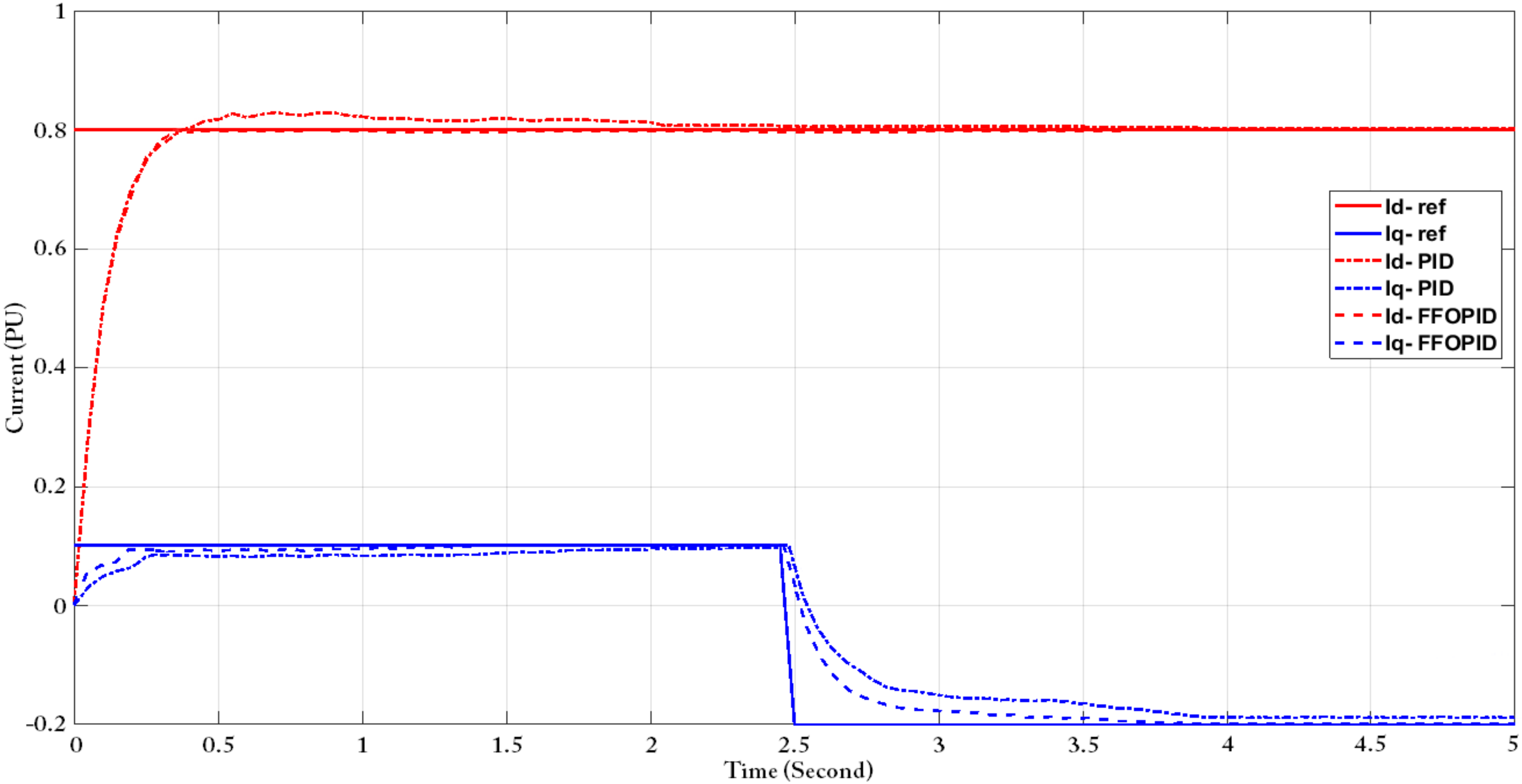

Figure 4.43 The response of PID and FFOPID controllers when I_{d-ref} is constant and I_{q-ref} is altered

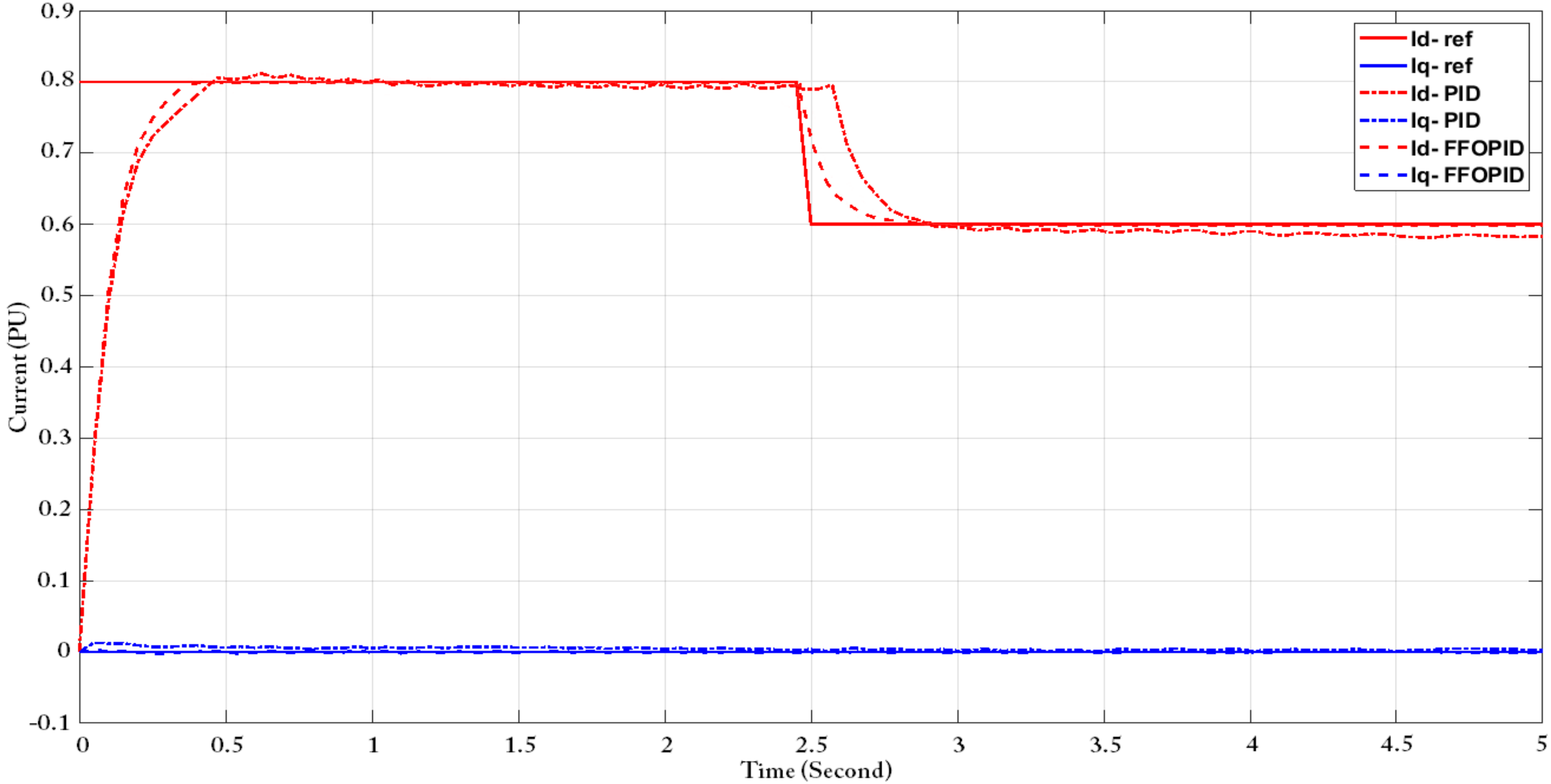

Figure 4.44 The response of PID and FFOPID controllers when I_{q-ref} is constant and I_{d-ref} is altered

Table 4.19 The qualitative comparison between PID and FFOPID controllers (I_{q-ref} is altered and I_{d-ref} is =0.8 pu)

Iq Value	Controller	Rise Time	Overshoot	Settling Time	St-St time
+ 0.1	FFO-PID	0.18	0.00	0.19	0.20
	Classical PID	0.20	0.00	0.25	0.32
- 0.2	FFO-PID	3.00	0.00	3.50	3.55
	Classical PID	3.50	0.00	3.80	4.00

Table 4.20 The qualitative comparison between PID and FFOPID controllers (I_{d-ref} is altered and I_{q-ref} is =0.0 pu)

Id Value	Controller	Rise Time	Overshoot	Settling Time	St-St time
+ 0.8	FFO-PID	0.30	0.00	0.40	0.48
	Classical PID	0.42	0.62	1.50	1.60
+ 0.6	FFO-PID	2.60	0.00	2.70	2.85
	Classical PID	2.80	3.60	2.90	3.30

4.12 The Summary

In this chapter, the work is divided into two stages .The first stage is the simulation design of three-phase SMC without and with LCL filter. Open-loop control systems are designed to control two stages of SMC, RS and IS. The SMC is fed from a three-phase AC source. The results for this design were obtained from the input and output (current, voltage, active power, reactive power) before and after using the LCL filter. The figures and tables are compared before and after using the LCL filter, to get the best AC output voltage with the lowest THD value. Finally, a 98% efficiency of SMC is obtained. The second stage, a WECS system simulation design based on PMSG with a capacity of 1.5 MW. All control systems are designed from pitch angle controller and operational controller. The PMSG based WECS is connected to the SMC to generate active and reactive output power. The closed-loop control system is designed to control the second stage of the SMC, namely, inverter stage. The closed-loop control system is designed twice, once using the PID controller, and using the FFOPID controller. The electrical grid is designed to consist of a transformer, power transmission lines, and loads. The power from the SMC-based WECS is finally injected into the electrical grid. Active and reactive power is obtained by using PID and FFOPID controllers separately. In the end, a comparison was made using both controllers PID and FFOPID, by changing the values of I_{d-ref},I_{q-ref}.

CHAPTER V

CONCLUSIONS

The simulation and design of a three-phase SMC-based WECS with a capacity of 1.5MW with the necessary control systems to operate the system was completed. After a brief introduction to the history of wind energy and the evolution of its use, until its use in the generation of electric power, we have included recent statistics on the growth of wind energy use in Turkey and the world. We discussed the principle of MC, in brief, and the main division of all types of MC. Moreover, we have identified the DMC and IMC with the electrical circuits of each type. Also, the comparisons show the superiority of the IMC.

The mathematical model of indirect MC is introduced, and SMC is briefly described with the method of obtaining the SMC with its modulation strategies. The principle of the work of the MC-based WECS in its operation was also described. In addition, we have given a description of the main control methods in the system. The mathematical model of the WECS used was also introduced; the mathematical model used for control systems was also presented. The work in this thesis is divided into two stages.

The first stage is discussed, in which the SMC was designed and modeled as it was fed from a three-phase constant voltage source and a purely resistive load was connected at its output. In the simulation study, the SMC control is realized by simultaneously operating two SPWM schemes for rectifier and inverter stages. It becomes then possible to change the SMC output voltage to the desired value by varying the gain and amplitude parameters of the rectifier and inverter stages. To improve voltage and current waveform quality at the output, an LCL filter is designed and added between the SMC output and the load. Simulation results verify the advantages of using such a filter.

The second stage. The results of the SMC from the first stage were used to adapt the three-phase SMC to the grid-connected wind energy conversion system. Therefore, the advantages of SMC, such as the lower number of semiconductor devices, will be effectively used in the renewable energy system. This feature also reduces energy losses and manufacturing costs for a truly renewable energy system. In addition, it has no energy storage elements such as transformer or capacitor, which makes it light and reliable in work. In the simulation study, control of the SMC-based WECS was achieved by designing a closed-loop control system based on the FFOPID controller to control the inverter stage of the SMC, with another block control following the WES.

The SMC control is realized by simultaneously operating the SPWM schemes for the rectifier stage and FFOPID for the inverter stage. The LCL filter was designed and added between the SMC output and the electrical grid. The proposed controller's efficiency has been proven through the use of step input with set-point change conditions. The proposed system proved robust and capable in light of the change in the generated power from the WES system. Thus, we see the change in the power injected into the grid.

The fuzzy logic system of FFOPID enhances the precise performance of the controller under various conditions. A comparative study was conducted with the classical PID controller to verify the validity of the proposed method in the FFOPID controller. Through the speed of response, the results of which clearly showed the superiority of the FFOPID controller over the classical PID, and that this controller is effective and can be an alternative to the current traditional PID controller, and from the results, it is also clear that it is the best for use with the WES. Finally, the SMC-based WECS achieved 92% efficiency with the PID controller and 94% efficiency with the FFOPID controller.

The simulation results have proven that a wide range of application areas of SMC topology is potentially available in addition to its successful application in renewable energies, especially those based on wind energy. There are greater opportunities to expand the field of this controller in the future through the entry of digital algorithms that the microprocessor or other digital systems can achieve.

REFERENCES

[1] EIA, I. U. (2014). Energy Information Administration (EIA).

[2] Tong, W. (2010). Fundamentals of wind energy. *Wind power generation and wind turbine design*, 3-48.

[3] Jain, B., Jain, S., Nema, R. K. (2015). Control strategies of grid interfaced wind energy conversion system: An overview. *Renewable and Sustainable Energy Reviews*, **47**, 983-996.

[4] "RüzgarEnerjiSantralleri" (in Turkish). EnerjiAtlası. Retrieved 2017-08-04.

[5] Türkiyeelektrikenerjisistatistikler (in Turkish). ElektrikMühendisleriOdası. Retrieved 2018-08-06.

[6] IEEE, peer verified methods program. Manual on policies and procedures. IEEE, Intl. www.tureb.com.tr, 22.08.2020.

[7] IEEE, peer verified methods program. Manual on policies and procedures. IEEE, Intl. Petroleum, B. (2020). Statistics https://www. bp.com/en/global/ corporate /energy-economics/ statistical-review- of-world- energy. html, 15.05.2020.

[8] IEEE, peer verified methods program. Manual on policies and procedures. IEEE, Intl. Ember: https://ember-climate.org/data/, 17.03.2020.

[9] IEEE, peer verified methods program. Manual on policies and procedures. IEEE, Intl. https://en.wikipedia. org/wiki/ Wind_ power_by_country, 14.07.2021.

[10] Madvar, M. D., Ahmadi, F., Shirmohammadi, R., Aslani, A. (2019). Forecasting of wind energy technology domains based on the technology life cycle approach. *Energy Reports*, **5**, 1236-1248.

[11] IEEE, https://www. luvside.de /en /hawt- advantage- disadvantage/, 03.01. 2021.

[12] IEEE, https://theconversation.com/wind-turbines-off-the-coast-could-help-austra- lia- become- an-energy- superpower- research- finds- 164590, 03.01.2021

[13] NC-ND license (http://creativecommons.org /lice- nses/by-ncnd/4.0/). Journal homepage: www.elsevier.com/locate/egyr, 18.9.2021.

[14] Kolar, J. W., Baumann, M., Schafmeister, F., Ertl, H. (2002, March). Novel three-phase AC-DC-AC sparse matrix converter. In *APEC. Seventeenth Annual IEEE Applied Power Electronics Conference and Exposition (Cat. No. 02CH37335)* **2**, 777-791. IEEE.

[15] Venturini, M. (1980). A new sine wave in sine wave out, conversion technique which eliminates reactive elements. *Proc. Powercon 7*.

[16] Venturini, M., Alesina, A. (1980, June). The generalised transformer: A new bidirectional, sinusoidal waveform frequency converter with continuously adjustable input power factor. In *1980 IEEE Power Electronics Specialists Conference* (242-252). IEEE.

[17] Stacey, E. J. (1976, June). An" unrestricted frequency changer" employing force commutated thyristors. In *1976 IEEE Power Electronics Specialists Conference* (165-173). IEEE.

[18] Jones, V. C., Bose, B. K. (1976). A frequency step-up cycloconverter using power transistors in inverse-series mode. *International Journal of Electronics Theoretical and Experimental*, **41 (6)**, 573-587.

[19] Daniels, A. R., Slattery, D. T. (1978, July). Application of power transistors to poly phase regenerative power convertors. In *Proceedings of the Institution of Electrical Engineers* (**125**, No. **7**, 643-647). IET.

[20] Alesina, A., Venturini, M. (1988, April). Intrinsic amplitude limits and optimum design of 9-switches direct PWM AC-AC converters. In *PESC'88 Record., 19th Annual IEEE Power Electronics Specialists Conference* (1284-1291). IEEE.

[21] Alesina, A., Venturini, M. G. (1989). Analysis and design of optimum-amplitude nine-switch direct AC-AC converters. *IEEE transactions on power electronics*, *4* **(1)**, 101-112.

[22] Venturini, M., Alesina, A. (1980, June). The generalised transformer: A new bidirectional, sinusoidal waveform frequency converter with continuously adjustable input power factor. In *1980 IEEE Power Electronics Specialists Conference* (242-252). IEEE.

[23] Klumpner, C., Nielsen, P., Boldea, I., Blaabjerg, F. (2002). A new matrix converter motor (MCM) for industry applications. *IEEE transactions on Industrial Electronics*, *49* **(2)**, 325-335.

[24] Xia, C., Yan, Y., Song, P., Shi, T. (2011). Voltage disturbance rejection for matrix converter-based PMSM drive system using internal model control. *IEEE Transactions on Industrial Electronics*, *59* **(1)**, 361-372.

[25] Casadei, D., Serra, G., Tani, A., Trentin, A., Zarri, L. (2005). Theoretical and experimental investigation on the stability of matrix converters. *IEEE Transactions on Industrial Electronics*, *52* **(5)**, 1409-1419.

[26] Burany, N. (1989, October). Safe control of four-quadrant switches. In *Conference Record of the IEEE Industry Applications Society Annual Meeting,* (1190-1194). IEEE.

[27] Kolar, J. W., Ertl, H. (2001). Vorrichtungzur quasi-direkt enpuls breitengesteuertenEnergieumformungzwischenDreiphasennetzen. *Austrian Patent AT412136B (2004-2) filed:(2001-7)*.

[28] Klumpner, C., Lee, M., Wheeler, P. (2006, November). A new three-level sparse indirect matrix converter. In *IECON 2006-32nd Annual Conference on IEEE Industrial Electronics* (1902-1907). IEEE.

[29] Rahmani, S., Rmili, L., Al-Haddad, K. (2015). A review of Indirect Matrix Converter Topologies. *Renewable Energy and Sustainable Development*, **1(1)**, 30-37.

[30] Kolar, J. W., Schafmeister, F., Round, S. D., Ertl, H. (2007). Novel three-phase AC–AC sparse matrix converters. *IEEE transactions on power electronics*, **22(5)**, 1649-1661.

[31] Holtz, J., Boelkens, U. (1989). Direct frequency convertor with sinusoidal line currents for speed-variable AC motors. *IEEE Transactions on Industrial Electronics*, **36(4)**, 475-479.

[32] Rmili, L., Rahmani, S., Fnaiech, F., Al-Haddad, K. (2013, December). Space vector modulation strategy for a direct matrix converter. In *14th International Conference on Sciences and Techniques of Automatic Control & Computer Engineering-STA'2013* (pp. 126-131). IEEE.

[33] Hornkamp, M., Loddenkötter, M., Münzer, M., Simon, O., Bruckmann, M. (2001, June). EconoMAC the first all-in-one IGBT module for matrix converters. In *Proc. PCIM* (1-6).

[34] IEEE, http://electricalarticle.com /comparison- of-scr-power -bjt- power-mosfet-igbt/, 17.05.2021.

[35] IEEE, https://electricalworkbook.com /difference- between- bjt-mosfet-and-igbt/, 17.5.2021.

[36] Wei, Z., Yang, X., Sun, G., Sun, Y., Ju, P. (2013). Wind power system state estimation with automatic differentiation technique. *International Journal of Electrical Power & Energy Systems*, **53**, 297-306.

[37] Shahbazi, M., Poure, P., Saadate, S., Zolghadri, M. R. (2011). Five-leg converter topology for wind energy conversion system with doubly fed induction generator. *Renewable Energy*, **36(11)**, 3187-3194.

[38] Grauers, A. Directly driven wind turbine generators, *Proceedings of the International Conference on Electrical Machines (ICEM'96), Vigo (Spain), Sept. 1996,* **2***, 417-422.*

[39] Lampola, P. (1998). Electromagnetic design of an unconventional directly driven permanent-magnet wind generator. In *International Conference on Electrical Machines, ICEM'98, Istanbul, Turkey, Sept. 2-4., 1998* (1705-1710). Middle East Technical University.

[40] Ramirez, D., Martinez, S., Carrero, C., Platero, C. A. (2012). Improvements in the grid connection of renewable generators with full power converters. *Renewable Energy*, **43**, 90-100.

[41] Delfino, F., Pampararo, F., Procopio, R., Rossi, M. (2011). A feedback linearization control scheme for the integration of wind energy conversion systems into distribution grids. *IEEE systems journal*, ***6*** **(1)**, 85-93.

[42] Zhang, Z., Hackl, C., Wang, F., Chen, Z., Kennel, R. (2013, September). Encoderless model predictive control of back-to-back converter direct-drive permanent-magnet synchronous generator wind turbine systems. In *2013 15th European conference on power electronics and applications (EPE)* (1-10). IEEE.

[43] Xia, C., Wang, Z., Shi, T., Song, Z. (2013). A novel cascaded boost chopper for the wind energy conversion system based on the permanent magnet synchronous generator. *IEEE Transactions on energy conversion*, **28(3)**, 512-522.

[44] MREC website at: www.mrec.orghttps://mrec.org/files/2014/03/HowDoWindTurbines.pdf, 23.10.2020.

[45] Mahela, O. P., Shaik, A. G. (2016). Comprehensive overview of grid interfaced wind energy generation systems. *Renewable and Sustainable Energy Reviews*, **57**, 260-281.

[46] Amei, K., Takayasu, Y., Ohji, T., Sakui, M. (2002, April). A maximum power control of wind generator system using a permanent magnet synchronous generator and a boost chopper circuit. In *Proceedings of the Power Conversion Conference-Osaka 2002 (Cat. No. 02TH8579)* **3**, 1447-1452. IEEE.

[47] Verdia, M., Johari, S., Kumar, V., Gidwani, L. (2020, January). A Technological Review on Multilevel Matrix Converter for Wind Power Generation System. In *2020 International Conference on Computer Communication and Informatics (ICCCI)* (1-10). IEEE.

[48] Szczesniak, P. (2009). *Analysis and testing matrix-reactance frequency converters* (Doctoral dissertation, PhD Thesis, University of Zielona Gora).

[49] Iwanski, G., Maciejewski, P., &Łuszczyk, T. (2020). New Stationary Frame Transformation for Control of a Three-Phase Power Converter under Unbalanced Grid Voltage Sags. *IEEE Journal of Emerging and Selected Topics in Power Electronics*.

[50] Astrom, K. (1995). PID controllers. *theory, design and tuning*.

[51] Matušů, R. (2011). Application of fractional order calculus to control theory. *International journal of mathematical models and methods in applied sciences*, ***5*** **(7)**, 1162-1169.

[52] Noutchie, S. C. O., Secer, A., Ray, S. S., El-Sayed, A. M. Theory, Methods, and Applications of Fractional Calculus.

[53] Cuong, H. M., Dong, H. Q., Van Trieu, P. (2021). Adaptive fractional-order terminal sliding mode control of rubber-tired gantry cranes with uncertainties and unknown disturbances. *Mechanical Systems and Signal Processing*, *154*, 107601.

[54] Girgis, M. E., Fahmy, R. A., Badr, R. I. (2020). Optimal fractional-order PID control for plasma shape, position, and current in Tokamaks. *Fusion Engineering and Design*, *150*, 111361.

[55] Chenbin, M., Yoichi, H. (2004). The application of fractional order control to backlash vibration suppression. In *Proceedings of conference on American control*.

[56] Rastogi, P., Chatterji, S., Karanjkar, D. S. (2012, December). Performance analysis of fractional-order controller for pH neutralization process. In *2012 2nd International Conference on Power, Control and Embedded Systems* (1-6). IEEE.

[57] Al-Dhaifallah, M., Kanagaraj, N., Nisar, K. S. (2018). Fuzzy fractional-order PID controller for fractional model of pneumatic pressure system. *Mathematical Problems in Engineering*, *2018*.

[58] Tepljakov, A., Petlenkov, E., Belikov, J. (2011). FOMCOM: a toolbox for fractional-order system identification and control. *International Journal of Microelectronics and computer science*, **2(2)**, 51-62.

[59] Azar, A. T., Vaidyanathan, S., Ouannas, A. (Eds.). (2017). *Fractional order control and synchronization of chaotic systems* (**688**). Springer.

[60] Ahmed, S. (2015). Parameter and delay estimation of fractional order models from step response. *IFAC-Papers OnLine*, **48(8)**, 942-947.

[61] Kumar, V., Joshi, R. R., Bansal, R. C. (2009). Optimal control of matrix-converter-based WECS for performance enhancement and efficiency optimization. *IEEE Transactions on Energy Conversion*, **24(1)**, 264-273.

[62] Rakesh, N., Nitya, A., Ram, G. (2014, July). Modelling and simulation of the wind energy electric conversion system to extract the maximum power from the wind using simulation environment. In *2014 Annual International Conference on Emerging Research Areas: Magnetics, Machines and Drives (AICERA/iCMMD)* (1-6). IEEE.

[63] Singh, A. K., Krisham, R., Sood, Y. (2013, April). Modeling and control of grid connected variable speed PMSG based wind energy system. In *Conference on Advances in Communication and Control Systems*.

[64] Vijayalakshmi, S., Saikumar, S., Saravanan, S., Sandip, R. V., Sridhar, V. (2011). Modelling and control of a wind turbine using permanent magnet synchronous generator. *International Journal of Engineering Science and Technology (IJEST)*, **3(3)**, 2377-2384.

[65] Grenier, D., Dessaint, L. A., Akhrif, O., Bonnassieux, Y., Le Pioufle, B. (1997). Experimental nonlinear torque control of a permanent-magnet synchronous motor using saliency. *IEEE Transactions on Industrial Electronics*, **44(5)**, 680-687.

[66] Samanvorakij, S., Kumkratug, P. (2013). Modeling and simulation PMSG based on wind energy conversion system in simulation environment. In *Proc. of Second Intl. Conf. on Advances in Electronics and Electrical Engineering* (37-41)..

[67] Toliyat, H. A., & Campbell, S. G. (2003). *DSP-based electromechanical motion control*. CRC press.

[68] Mei, F., Pal, B. (2007). Modal analysis of grid-connected doubly fed induction generators. *IEEE transactions on energy conversion*, **22(3)**, 728-736.

[69] Pavel, C. C., Lacal-Arántegui, R., Marmier, A., Schüler, D., Tzimas, E., Buchert, M., Blagoeva, D. (2017). Substitution strategies for reducing the use of rare earths in wind turbines. *Resources Policy*, *52*, 349-357.

[70] Jensen, B. B., Mijatovic, N., & Abrahamsen, A. B. (2016). Advantages and challenges of superconducting wind turbine generators.

[71] Rivera, D. E., Morari, M., Skogestad, S. (1986). Internal model control: PID controller design. *Industrial & engineering chemistry process design and development*, **25(1)**, 252-265.

[72] Ho, M. T., Lin, C. Y. (2003). PID controller design for robust performance. *IEEE Transactions on Automatic Control*, **48(8)**, 1404-1409.

[73] Al-Dhaifallah, M. (2019, March). Heat Exchanger Control Using Fuzzy Fractional-Order PID. In *2019 16th International Multi-Conference on Systems, Signals Devices (SSD)* (73-77). IEEE.

[74] Junyi, C., Binggang, C. (2011). Fractional-order control of pneumatic position servosystems. *Mathematical Problems in Engineering*, *2011*.

[75] Gutierrez, R. E., Rosario, J. M., Tenreiro Machado, J. (2010). Fractional order calculus: basic concepts and engineering applications. *Mathematical problems in engineering*, *2010*.

[76] Petras, I. (2008). Stability of fractional-order systems with rational orders. *arXiv preprint arXiv:0811.4102*.

[77] Karami, M., Kazemi, A., Vatankhah, R., Khosravifard, A. (2021). Adaptive fractional-order backstepping sliding mode controller design for an electrostatically actuated size-dependent microplate. *Journal of Vibration and Control*, *27*(**11-12)**, 1353-1369.

[78] Petráš, I. (2012). Tuning and implementation methods for fractional-order controllers. *Fractional Calculus and Applied Analysis*, **15(2)**, 282-303.

[79] Manabe, S. (1960). The non-integer integral and its application to control systems. *Journal of Institute of Electrical Engineers of Japan*, **80 (860)**, 589-597.

[80] Oustaloup, A., Levron, F., Mathieu, B., Nanot, F. M. (2000). Frequency-band complex noninteger differentiator: characterization and synthesis. *IEEE Transactions on Circuits and Systems I: Fundamental Theory and Applications*, **47(1)**, 25-39.

[81] Luersen, M. A., Le Riche, R. (2004). Globalized Nelder–Mead method for engineering optimization. *Computers & structures*, **82(23-26)**, 2251-2260.

[82] Mudi, R. K., Pal, N. R. (1999). A robust self-tuning scheme for PI-and PD-type fuzzy controllers. *IEEE Transactions on fuzzy systems*, **7(1)**, 2-16.

[83] Wu, X., Xu, Y., Liu, J., Lv, C., Zhou, J., Zhang, Q. (2020). Characteristics analysis and fuzzy fractional-order PID parameter optimization for primary frequency modulation of a pumped storage unit based on a multi-objective gravitational search algorithm. *Energies*, **13(1)**, 137.

CIRRICULUM VITAE (CV)

Name: WALEED KHALED ABDULRAZAQ ABDULRAZAQ

Language: Arabic, and English

Education:

- **Bachelor of Electrical and Electronic Engineering**
  AL-Anbar University
  Iraq
- **Higher Diploma in Business Management**
  European University
  Turkey
- **Diploma, Digital Marketing**
  Show Academy
  Ireland
- **Master of Electric and Electronic Engineering**
  Department of Electrical and Electronic Engineering
  Gaziantep University
  Turkey

Work Experience

- Customer Service Manager in Zain Iraq Company: Dec.2010- Jul.2011
- Implementation Engineer In AL-furat General Constructing: Jul.2011- Des.2011
- Supervising Engineer in Ministry Agriculture: Dec.2011- Jun.2014
- Manager In WD Group Company: Jul.2014- Des.2017
- Manager of Project follow-up Division in Ministry Agriculture: Jan.2018- continue

Computer Skills:

- Microsoft Office (word, excel, power point and outlook)
- Visual Basic
- CST Studio
- Autocad
- Matlab
- Google Sketchup Design
- Network Security
- Android App

Memberships:

- The Iraqi Engineers Association: Apr.2011
- Iraqi Association for Public Housing: Oct.2012
- Arab Foundation for Management Development: Jul.2016
- Turkish-Arab Chamber of Commerce: Jul.2016

Training and Certifications:

- International Academy of Personal Training and Leadership Development: Jun.2012.
- Personal Strategic Planning: Des.2012
- Visual Basic language: Jun.2013.
- AutoCAD Design Program: Aug.2013
- Euro-Arab Organization for Business: Jul.2015
- Turkish-Arab Chamber of Business Administration: Jul.2016
- Arab Foundation for Management Development: Jun.2018

PUBLICATIONS

Journals:

[1] Abdulrazaq, Waleed Khaled Abdulrazaq &Vural, Ahmet Mete. "Fuzzy Fractional-order PID Control Scheme for PMSG Driven Wind Energy Conversion System with Sparse Matrix Converter Topology", submitted to **IETE Journal of Research (SCI-E)**.

Conferences:

[1] Abdulrazaq,Waleed Khaled Abdulrazaq &Vural, Ahmet Mete. "Sparse Matrix Converter Modelling and Simulation", 7th International Conference on Engineering and Natural Science, June 23-27 2021, Sarajevo – Serbia.